

5-2008

HD 100453 : an evolutionary link between protoplanetary disks and debris disks.

Karen Alicia Collins 1962-
University of Louisville

Follow this and additional works at: <https://ir.library.louisville.edu/etd>

Recommended Citation

Collins, Karen Alicia 1962-, "HD 100453 : an evolutionary link between protoplanetary disks and debris disks." (2008). *Electronic Theses and Dissertations*. Paper 266.
<https://doi.org/10.18297/etd/266>

This Master's Thesis is brought to you for free and open access by ThinkIR: The University of Louisville's Institutional Repository. It has been accepted for inclusion in Electronic Theses and Dissertations by an authorized administrator of ThinkIR: The University of Louisville's Institutional Repository. This title appears here courtesy of the author, who has retained all other copyrights. For more information, please contact thinkir@louisville.edu.

HD 100453: AN EVOLUTIONARY LINK BETWEEN PROTOPLANETARY DISKS AND DEBRIS DISKS

By

Karen Alicia Collins

A Thesis
Submitted to the Faculty of the
Graduate School of the University of Louisville
in Partial Fulfillment of the Requirements
for the Degree of

Master of Science

Department of Physics and Astronomy
University of Louisville
Louisville, Kentucky

May 2008

HD 100453: AN EVOLUTIONARY LINK BETWEEN PROTOPLANETARY DISKS AND DEBRIS DISKS

By

Karen Alicia Collins

A Thesis Approved on

April 24, 2008

by the following Thesis Committee:

Thesis Director

Thesis Co-Director

ACKNOWLEDGEMENTS

This work was supported by a graduate fellowship from the Kentucky Space Grant Consortium (KSGC) under NASA National Space Grant College and Fellowship Program Grant NNG05GH07H. I would like to extend my sincerest thanks to my science mentor and research co-advisor, Dr. Carol Grady, for her extreme patience, expert guidance, and for the opportunity to lead this very interesting project and to collaborate with the distinguished astrophysicists who contributed to this work. Furthermore, I would like to thank my research advisor, Dr. Gerard Williger, for providing me with the opportunity to work in his research group, for his expert advice, for the KSGC fellowship opportunity, and for the opportunity to collaborate with Dr. Grady. Many collaborators have gone beyond making a contribution to the work and have helped to greatly enrich my education. For this reason, I extend a special thanks to Drs. John Wisniewski, Michael Sitko, Sean Brittain, and Andres Carmona. Finally, I would like to thank Dr. John Kielkopf and Dr. Timothy Dowling for participating on my thesis committee.

I would like to thank the following collaborators for contributing valuable observations, data, data reduction, and results to this thesis. Gerry Williger of the University of Louisville contributed FUSE data reduction and related results. Kenji Hamaguchi and Rob Petre of NASA/GSFC contributed Chandra X-ray data and related results. John Wisniewski of NASA/GSFC contributed HST ACS HRC data and related results. Sean Brittain of Clemson University contributed Gemini South CO

spectroscopic data and related results. Mike Sitko and Joey Carpenter of the University of Cincinnati provided SED data and related results. Roy van Boekel of the Max-Planck-Institut für Astronomie in Germany contributed VLT NACO photometric data and related results. Andres Carmona and Mario van den Ancker of the European Southern Observatory provided VLT SINFONI NIR spectroscopic data and results. Gwendolyn Meeus of the Astrophysikalisches Institut Potsdam contributed FEROS Ca II spectroscopic data. Jonathan Williams and Geoff Mathews of the University of Hawaii contributed JCMT HARP CO spectroscopic data and related results. Xuepeng Chen of the Max-Planck-Institut für Astronomie provided common proper motion data reduction from the VLT NACO observations. Bruce Woodgate of NASA/GSFC and Thomas Henning of the Max-Planck-Institut für Astronomie provided overall scientific support, detailed comments, and direction. George Hartig of STScI contributed information regarding the SBC design and investigated the probable source of the SBC optical ghost.

This work is based on observations made with the NASA/ESA Hubble Space Telescope (HST) as part of the HST-GO-10764 (Grady, PI). HST is operated by the Association of Universities for Research in Astronomy, Inc., under NASA Contract NAS5-26555. Based on observations made with the Chandra X-Ray Observatory as part of the Chandra Cycle 7 program P07200493 (Grady, PI). Chandra is operated by the Smithsonian Astrophysical Observatory for and on behalf of the National Aeronautics Space Administration under contract NAS8-03060. Based on observations made with the NASA-CNES-CSA Far Ultraviolet Spectroscopic Explorer, which is operated for NASA by Johns Hopkins University under NASA contract NAS5-32985. The FUSE data were

collected under the FUSE GI program C126. This work is also based on observations obtained at the Gemini Observatory, which is operated by the Association of Universities for Research in Astronomy, Inc., under a cooperative agreement with the NSF on behalf of the Gemini partnership. The Phoenix infrared spectrograph was developed and is operated by the National Optical Astronomy Observatory and the observations were obtained as part of program GS-2006B-C-3. This work is also based on observations collected at the European Southern Observatory, Chile with VLT NACO under observing program 077.C-0570(A), on observations collected at the European Southern Observatory, Chile with VLT SINFONI under observing program ID 079.C-0018(A), on observations collected at The James Clerk Maxwell Telescope, which is operated by The Joint Astronomy Centre, on archival data obtained with the Spitzer Space Telescope, which is operated by the Jet Propulsion Laboratory, California Institute of Technology under a contract with NASA, and on archival IUE data collected under observing program ID RM050.

ABSTRACT

HD 100453: An Evolutionary Link Between Protoplanetary Disks and Debris Disks

Karen A. Collins

April 24, 2008

Herbig Ae stars are young stars usually surrounded by gas and dust in the form of a disk and are thought to evolve into planetary systems similar to our own. We present a multi-wavelength examination of the disk and environment of the Herbig Ae star HD 100453A, focusing on the determination of accretion rate, system age, and disk evolution. We show that the accretion rate is characterized by Chandra X-ray imagery that is inconsistent with strongly accreting early F stars, that the disk lacks the conspicuous Fe II emission and continuum seen in FUV spectra of actively accreting Herbig Ae stars, and that FUSE, HST, and FEROS data suggest an accretion rate below $\sim 2.5 \times 10^{-10} M_{\odot} \text{ yr}^{-1}$. We confirm that HD 100453B is a common proper motion companion to HD 100453A, with spectral type M4.0V – M4.5V, and derive an age of 14 ± 4 Myr. We examine the Meeus et al. (2001) hypothesis that Meeus Group I sources, which have a mid-IR bump which can be fitted by a black body component, evolve to Meeus Group II sources, which have no such mid-IR bump. By considering stellar age and accretion rate evidence, we find the hypothesis to be invalid. Furthermore, we find that the disk characteristics of HD 100453A do not fit the traditional definition of a protoplanetary disk, a transitional disk, or a debris disk, and they may suggest a new class of disks linking gas-rich protoplanetary disks and gas-poor debris disks.

TABLE OF CONTENTS

	PAGE
ACKNOWLEDGEMENTS	iii
ABSTRACT	vi
LIST OF TABLES	xi
LIST OF FIGURES	xii
1. INTRODUCTION	1
1.1 Molecular Cloud Collapse	1
1.2 The SED and IR Excess	4
1.3 Circumstellar Disk Evolution	7
1.3.1 Protoplanetary Disk Phase	7
1.3.2 Transitional Disk Phase	11
1.3.3 Debris Disk Phase	13
1.4 Meeus Groups	13
1.5 Thesis Goal and Approach	16
1.6 Characteristics of HD 100453	19
1.7 Age Determination Techniques	19
1.8 Instrumentation Requirements	21
1.8.1 High Spatial Resolution Spectroscopy	23
1.8.2 High Spatial Resolution Photometry	23

1.8.3 Coronagraphic Imaging and psf-Subtraction	24
1.8.4 Sub-millimeter Photometry	26
1.8.5 FUV and X-ray Spectroscopy	27
1.8.6 Summary of Instrumentation	28
2. THE DISK AND ENVIRONMENT OF HD 100453.....	29
2.1. Introduction.....	30
2.2. Observations and Data Reduction.....	30
2.2.1 Imagery	31
2.2.1.1 Chandra ACIS-S Imagery	31
2.2.1.2 HST ACS/HRC Imagery.....	35
2.2.1.3 HST ACS/SBC Imagery	36
2.2.1.4 VLT NACO Imagery	39
2.2.2 Spectroscopy	40
2.2.2.1 VLT SINFONI Spectroscopy	40
2.2.2.2 FUSE Spectroscopy	43
2.2.2.3 Gemini South Phoenix Echelle Spectroscopy.....	47
2.2.2.4 JCMT HARP Spectroscopy	47
2.2.2.5 ESO 1.52 m FEROS Echelle Spectroscopy	49
2.2.2.6 IUE Archival Data	50
2.3. Results.....	51
2.3.1 A T-Tauri Star near HD 100453A	51
2.3.1.1 Spectral Type Determination	55
2.3.1.2 Photometry	57

2.3.1.3 Relative Proper Motion.....	60
2.3.2 A Third Object in the Field.....	61
2.3.3 The Age of the System.....	62
2.3.3.1 Companion Star H-R Diagram.....	64
2.3.3.2 Primary Star H-R Diagram	65
2.3.4 Accretion and Mass Loss of the Primary.....	68
2.3.4.1 H α Emission	68
2.3.4.2 FUV Limits	69
2.3.4.3 Ca II λ 8662 Å Limits	70
2.3.4.4 X-Ray Limits	72
2.3.4.5 Jet and HH Knot Limits	72
2.3.5 Constraints on Disk Structure	74
2.3.5.1 Spatially Resolved PAH Features.....	75
2.3.5.2 Limiting Surface Brightness	75
2.3.5.3 The Inner Disk	77
2.3.5.4 The Outer Disk.....	81
2.4. Discussion.....	83
2.5. Summary of Results.....	89
3. CONCLUSIONS	91
3.1 Results of the Thesis Statement Test	91
3.2 Possible Physical Explanations.....	94
3.3 Future Directions	98
3.3.1 NICMOS on HST	98

3.3.2 ACS and STIS on HST	101
3.3.3 Millimeter/Submillimeter Interferometry	101
3.3.4 Mid-IR Imaging and Spectroscopy	102
3.3.5 NICI on Gemini South.....	103
3.3.6 Atacama Large Millimeter Array (ALMA)	104
3.3.7 Space-based Missions	106
REFERENCES	108
APPENDIX.....	115
A. AN OPTICAL GHOST IN HST/ACS/SBC F122M	116
A.1 Introduction.....	116
A.2 Observations.....	116
A.2.1 Program Star Observations	116
A.2.2 Archival Observations.....	117
A.3 Data Reduction.....	117
A.3.1 Known ACS/SBC Anomalies	118
A.4 Analysis.....	119
A.4.1 Identification of an Optical Ghost.....	119
A.4.2 Characterization of the Ghost	120
A.5 Discussion	120
GLOSSARY OF ACRONYMS.....	123
CURRICULUM VITAE.....	127

LIST OF TABLES

TABLE	PAGE
Table 1.1. Summary of Wavelength Band Definitions.....	6
Table 1.2. Summary of HD 100453A Previously Known Characteristics	20
Table 1.3. Summary of Instrumentation	28
Table 2.1. Summary of X-ray Spectral Fit Parameters.....	34
Table 2.2. Summary of HST/ACS Observations	35
Table 2.3. Summary of White Dwarf HS2027+0651 psf Star Observations.....	37
Table 2.4. Summary of VLT SINFONI Observations of HD 100453B	41
Table 2.5. Summary of FUSE Observations.....	43
Table 2.6. Summary of Photometry	59
Table 2.7. Summary of Accretion Rate Indicators	74
Table 3.1. Summary of Meeus Group I and II age estimates	93
Table A.1. Summary of Ghost Observations (HST/ACS/SBC F122M)	118
Table A.2. Summary of Optical Ghost Results.....	121

LIST OF FIGURES

FIGURE	PAGE
Figure 1.1. The four stages of star formation.....	3
Figure 1.2. Schematic picture of the environment of a young stellar object.	4
Figure 1.3. Black Body Spectral Energy Distributions (SEDs).....	5
Figure 1.4. Example SED for a Herbig Ae star plus circumstellar disk.	8
Figure 1.5. SED model and distance scale for a young protoplanetary flared disk.	10
Figure 1.6. Vertical dust structure of a flaring protoplanetary disk.....	11
Figure 1.7. SED comparisons for 3 phases of Herbig Ae/Be star disk evolution.....	14
Figure 1.8. Meeus Group I and Group II determination.	17
Figure 1.9. Meeus Group I and Group II physical models.	18
Figure 1.10. H–R diagram for HD 169142.....	22
Figure 1.11. Demonstration of ACS coronagraphic imaging performance.	26
Figure 2.1. Chandra X-ray Imagery of the HD 100453 system.....	33
Figure 2.2. Pulse height spectrum of HD 100453A and HD 100453B.....	34
Figure 2.3. FUV image of the HD 100453 system.	39
Figure 2.4. SINFONI spectra of HD 100453B in the J, H and K bands.....	44
Figure 2.5. FUSE spectra of HD 100453.....	46
Figure 2.6. Phoenix echelle M-band spectra of HD 100453.....	48
Figure 2.7. Spectra of HD 100453A near the Ca II infrared triplet line $\lambda 8662.17 \text{ \AA}$	50

Figure 2.8. HST F606W direct image of the HD 100453 system.....	52
Figure 2.9. HST F606W coronagraphic image of the HD 100453 system.....	53
Figure 2.10. HST F122M FUV psf-subtracted image of the HD 100453 system.	55
Figure 2.11. Relative proper motion for star C.....	63
Figure 2.12. Hertzsprung-Russell diagram for HD 100453B.....	65
Figure 2.13. Hertzsprung-Russell diagram for HD 100453A.....	67
Figure 2.14. <i>log</i> FUV continuum vs. <i>log</i> accretion rate for Herbig Ae stars.....	70
Figure 2.15. Limiting surface brightness of HD 100453A’s scattered light disk.....	77
Figure 2.16. Herbig Ae/Be star CO luminosity vs. NIR excess.	80
Figure 2.17. Herbig Ae/Be star CO luminosity vs. mass accretion rate.	81
Figure 2.18. Summary of Disk Structure Constraints.....	84
Figure 3.1. Age vs. <i>log</i> accretion rate for the Group I and Group II sources	94
Figure 3.2. Schematic representation of the HD 100546 system.....	96
Figure 3.3. SEDs of HD 100546, HD 100453, and HD 169142.....	99
Figure 3.4. HST coronagraphic capabilities of ACS, STIS, and NICMOS.....	100
Figure 3.5. NICI estimated contrast ratio in H-band.	104
Figure 3.6. A simulation of ALMA observations at 950 GHz (310 μ m).	105
Figure A.1. Optical ghost imagery.....	122

1. INTRODUCTION

A topic of intense current astrophysical research is the study of young stellar environments, with the goal of understanding how stars and planetary systems form. Since the timescale over which stars and planets form is on the order of millions of years, we cannot possibly trace the formation of any single system in one human lifetime. However, by studying a number of young systems in various stages of development, we can begin to build up a complete set of evolutionary paths that characterize the formation of stars and planets. By making the reasonable assumption that the physics that controlled the evolution of our Solar System is the same as the physics for the other systems studied, we can develop an understanding of how our own solar system and the planet on which we live came into existence. Although the introduction of a new generation of astronomical instruments has enabled much progress over the past few decades, many important questions regarding the star and planet formation processes still remain unanswered. In this thesis, I attempt to test previously proposed sequencing of observational properties believed to be indicative of specific phases of stellar evolution.

1.1 Molecular Cloud Collapse

The standard model of the birth of a star from a molecular cloud (mostly H₂ gas) can be divided into four distinct phases (Shu et al. 1987). The first phase begins with the formation of a slowly rotating dense core in the molecular cloud (Figure 1.1a). Although

isolated clouds tend to have angular momentum vectors perpendicular to the galactic plane suggesting that their spin arises from galactic shear, the internal structures have more randomly oriented spin axes due possibly to turbulence, or dynamical interactions (Phillips 1999).

The second phase begins when the condensing cloud core crosses the threshold of instability and collapses from “inside-out”. Material with low angular momentum collapses under its own gravity to form the protostar. However, material with higher angular momentum naturally collapses into a rotating disk structure (i.e. a circumstellar disk). The star can then accrete the disk material if the disk can shed angular momentum. Even though the cloud may be rotating slowly, it is large, and angular momentum conservation forces the star and disk to rotate more rapidly than the collapsing cloud. This evolutionary phase is characterized by a central protostar and disk, deeply embedded within an infalling envelope of dust and gas (Figure 1.1b).

The third phase leads to collimated jets and bipolar outflows (Figure 1.1c). Stars with mass less than about $2 M_{\odot}$ will likely produce a self-reinforcing magnetic field (a dynamo) due to convection and the differential rotation of the star. The magnetic field is believed to channel infalling material such that part of it is ejected away from the star through columns centered on the rotational poles of the star (see Figure 1.2). The ejecta can carry away part of the angular momentum of the system, allowing accretion of disk mass onto the central object. These collimated flows of ejecta are sometimes referred to as collimated jets or bipolar outflows. These outflows start to disperse the material surrounding the star near the poles, and the star and disk begin to be revealed (at viewing angles in line with a rotational pole).

Over time, as accretion onto the star itself decreases while collapse of material onto the disk continues, the opening angle of the stellar outflow increases. As a result, the fourth phase of stellar evolution is realized when the star and circumstellar disk are fully revealed (Figure 1.1d). Such objects are called T Tauri stars for $M < 2 M_{\odot}$ (Joy 1945), and Herbig Ae/Be stars for $2 < M/M_{\odot} < 8$ (Herbig 1960).

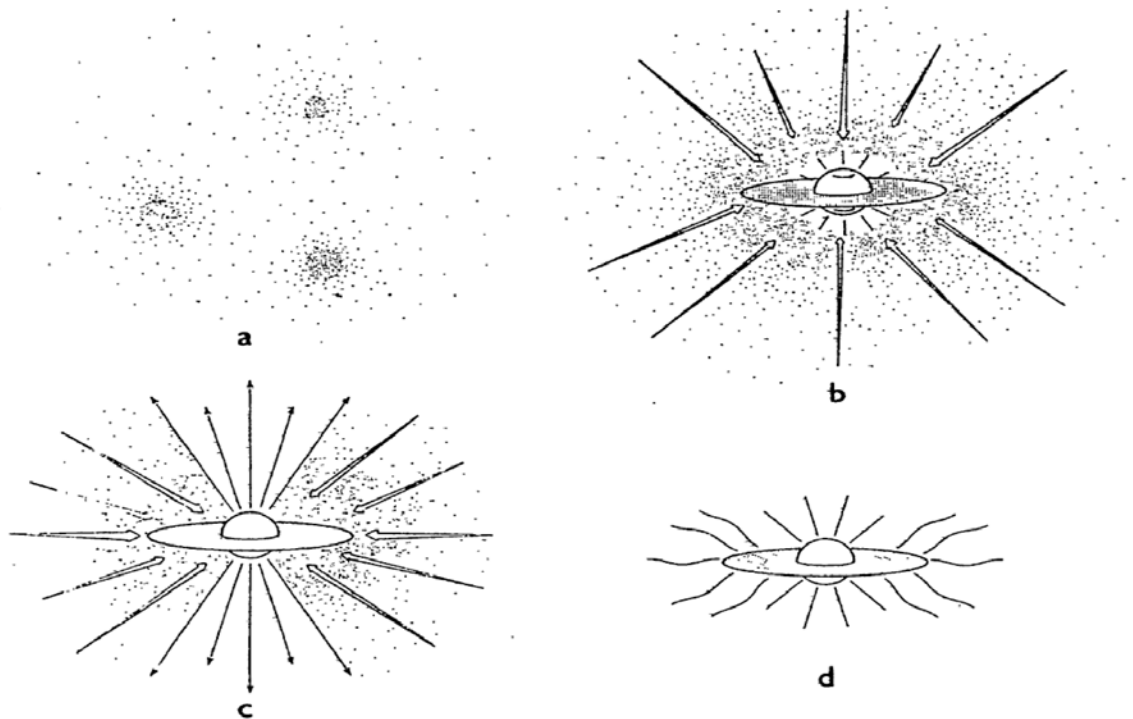


Figure 1.1. The four stages of star formation.

(a) Cores form within molecular clouds. (b) A protostar with a surrounding nebular disk forms at the center of a cloud core. (c) Outflows emerge along the rotational axes of the star, creating a bipolar outflow. (d) As the low angular momentum material is depleted, the remaining high angular momentum rotating material falls preferentially onto the disk rather than the star, the opening angle of the outflow of material broadens, and the star and circumstellar disk are fully revealed (after Shu et al. 1987).

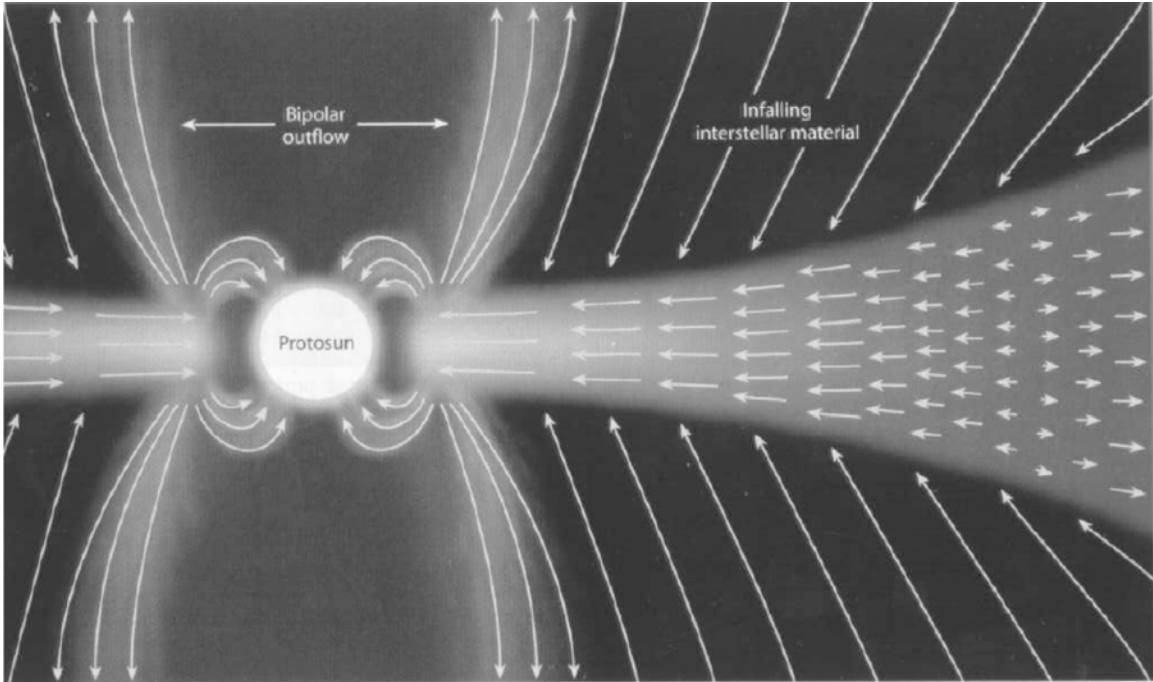


Figure 1.2. Schematic picture of the environment of a young stellar object.

Infall of matter onto the circumstellar disk, accretion onto the central star and accretion-driven outflow are indicated by arrows (from Wood 1997).

1.2 The SED and IR Excess

A typical star radiates energy (photons) in a way that can be approximated as a black body with a temperature equal to that of the visual surface (photosphere) of the star. The total energy radiated can be broken down into its spectral energy distribution (SED) (a Glossary of Acronyms is provided after the Appendix) and plotted as energy versus wavelength. Figure 1.3 shows the SEDs for black bodies with temperatures 7500 K, 3000 K, and 1500 K. For comparison, the Sun has an effective temperature of about 5800 K.

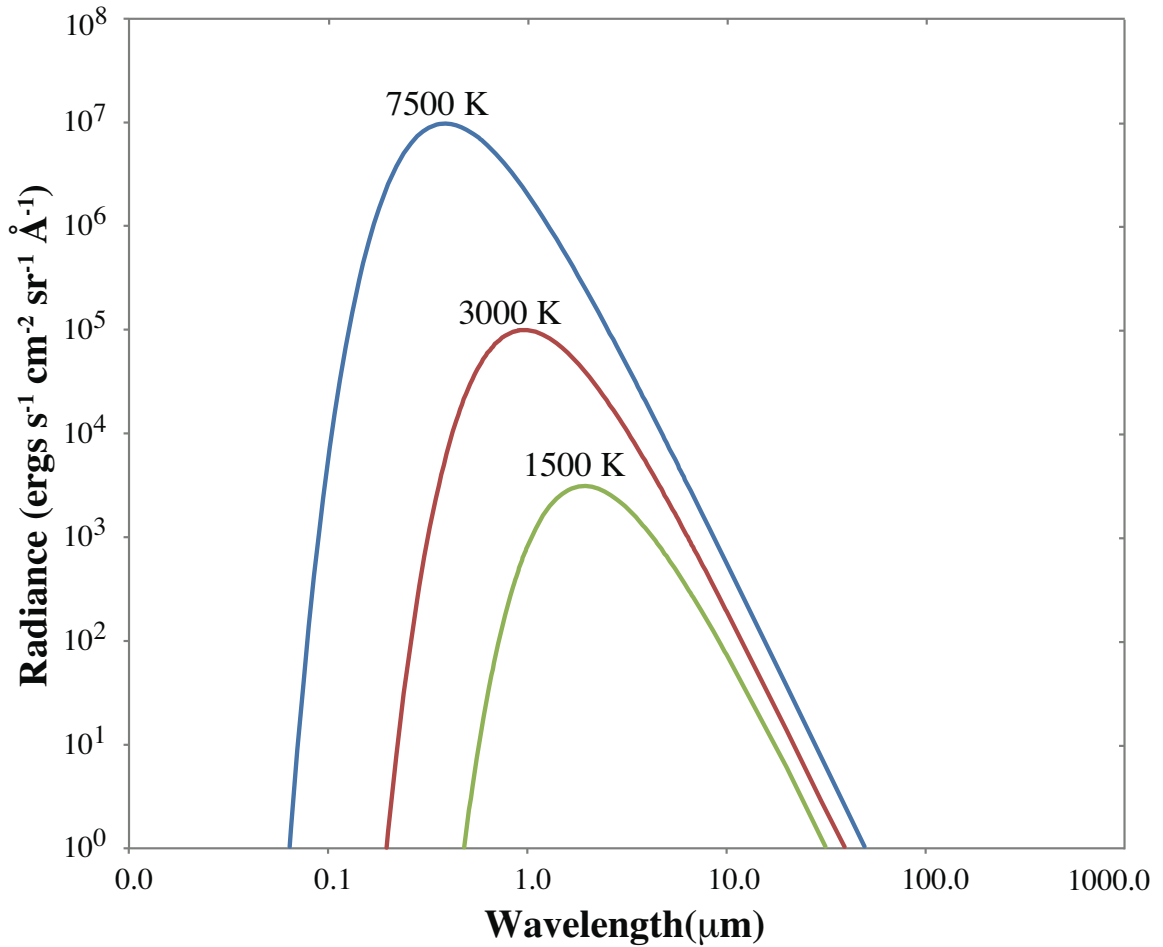


Figure 1.3. Black Body Spectral Energy Distributions (SEDs).

Radiance versus wavelength for black bodies with temperatures of 7500 K, 3000 K, and 1500 K. Typical stars radiate with SEDs similar to a black body with the temperature of the visual surface (photosphere) of the star.

A characteristic of all known T Tauri and Herbig Ae/Be stars is infrared (IR) emission which is stronger than expected from stellar blackbody radiation: the "IR excess". Since the environments of T Tauri and Herbig Ae/Be stars contain significant amounts of circumstellar material, some of the photons radiated by the star interact with dust particles and gas within the disk and are either scattered or absorbed. The scattered

photons allow us to directly image the disk at wavelengths characteristic of the temperature of the star. Furthermore, most of the absorbed energy is eventually re-radiated as thermal emission, but since the disk environment is cooler than the photosphere of the star, the peak wavelength of the re-radiated energy (1 – 50 μm) is longer than the peak wavelength of the absorbed energy ($\sim 0.5 \mu\text{m}$). This re-radiation then produces higher than expected levels of energy in the IR (Finkenzeller & Mundt 1984, Bastian et al. 1983). For the purposes of this thesis, wavelength bands, abbreviations, and wavelength range specifications are summarized in Table 1.1.

Table 1.1

Summary of Wavelength Band Definitions

Band	Abbreviation	Wavelength Range
X-ray	X-ray	1 – 100 \AA
Far-ultraviolet	FUV	1000 – 1200 \AA
Optical/Visible	Optical/Visible	4000 – 7000 \AA
Infrared	IR	1 – 350 μm
Near-Infrared	NIR	1 – 7 μm
Mid-Infrared	MIR	7 – 40 μm
Far-Infrared	FIR	40 – 350 μm
Sub-millimeter	sub-mm	350 μm – 1 mm
Millimeter	mm	$\geq 1 \text{ mm}$

Since disk material near the star is generally warmer than material farther away, thermal emission from the disk will be peaked at specific wavelength(s), depending on

the temperature of structures in the disk. For Herbig Ae stars, disk material near the star ($< \sim 1$ AU) is characterized by temperatures higher than about 500 – 1000 K and the emission tends to peak in the NIR (Figure 1.4). As demonstrated in Figure 1.2, the very inner part of the disk is dust-free due to dust sublimation at very high temperatures, leaving an inner edge to the dust in the disk. This disk “inner rim” is expected to be much hotter than the rest of the disk behind it, and is responsible for most of the NIR excess emission. Material farther out in the disk tends to peak in the MIR to FIR between $\sim 10 - 50 \mu\text{m}$. The midplane of the outer disk is even colder and is the primary contributor to emission at sub-mm and millimeter wavelengths. Thus, the observed SED can provide information to constrain the characteristics of the circumstellar environment. However, degeneracies in the disk configuration can still exist unless additional information is known about the environment (e.g. disk inner and outer radii, system inclination, grain size distribution, etc.).

1.3 Circumstellar Disk Evolution

In this work, we focus on circumstellar disk evolution of Herbig Ae stars. T Tauri disk evolution is similar, but some differences exist due to the effects of the lower mass central star, the consideration of which is beyond the scope of this work.

1.3.1 Protoplanetary Disk Phase

In the initial phase of disk evolution, circumstellar disks are characterized by gas-rich disks with small (submicron) dust grains and by gas mass to dust mass ratios of $\sim 100:1$, similar to the characteristics of the interstellar medium. With an abundance of gas near the star, the accretion rate for protoplanetary disks of Herbig Ae stars is initially

high with typical rates of more than $\sim 1 \times 10^{-8} M_{\odot} \text{ yr}^{-1}$. Since the disk initially extends from very near the star out to greater than several hundred AU or more, the SED is characterized by strong levels of NIR to FIR excess (Zuckerman 2001). Disks in this initial phase of evolution are generally called protoplanetary disks. Since the gas is well mixed with the dust, and the disk is in a state of hydrostatic equilibrium, dust material can be supported at significant distances from the disk mid-plane.

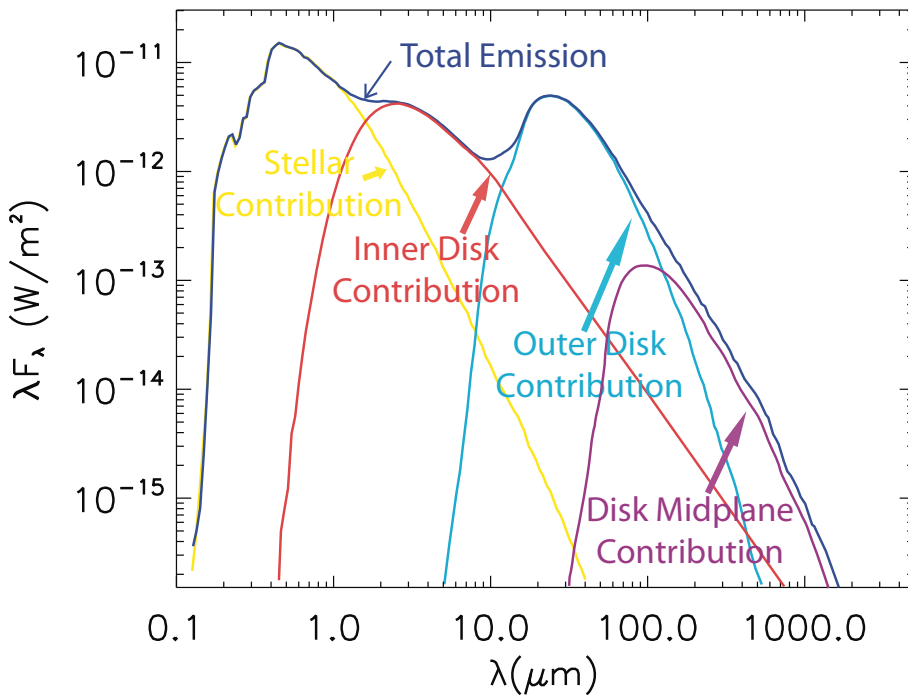


Figure 1.4. Example SED for a Herbig Ae star plus circumstellar disk.

The stellar contribution is well approximated by a black body with a temperature equal to that of the stellar photosphere and dominates at shorter wavelengths. The inner disk contributes excess NIR emission. The outer disk contributes excess MIR and FIR emission and peaks in the 10 – 50 μm region. The disk midplane is the coldest region and contributes excess emission at the sub-mm and millimeter wavelengths (after figure provided by M. Sitko, private communication).

Kenyon and Hartmann (1987) recognized that a natural explanation for the strong flux in the MIR to FIR of many protoplanetary disks is a flaring disk structure (Figure 1.5). Flaring disks are expected if small grains, which absorb and re-radiate the stellar radiation efficiently, are well-mixed with the gas. Then the gas pressure will support larger scale heights at larger radii. The disks are characterized by a scale height (h) which is a power law of the distance from the star (r) with index greater than one (i.e. $h \propto r^\alpha$, where $\alpha > 1.0$). Typical flared protoplanetary disks with no gaps produce a relatively flat SED out beyond $\sim 100 \mu\text{m}$ (depending on the degree of flaring and the physical extent of the disk). The NIR bump comes from the inner rim that is directly illuminated by the star (Figure 1.6). The MIR to FIR excess is from the warm upper dust layers of the disk, and the FIR to millimeter emission comes mostly from the disk midplane in the outer regions of the disk. See Figure 1.7 for a comparison of the SEDs of three Herbig Ae/Be stars at different phases of disk evolution. Note the relatively flat IR emission for the protoplanetary disk of AB Aur at ~ 2.5 Myr (Figure 1.7a).

As protoplanetary disks age, dust grains grow in size, and disks are expected to become vertically stratified with larger grains tending to settle to the disk midplane (Weidenschilling 1997), while smaller grains and gas can remain in the upper layers of the disk (Goldreich and Ward 1973; Youdin and Shu 2002; Isella 2006). Figure 1.6 illustrates the stratified dust layers. The very inner part of the disk is dust-free due to sublimation above temperatures of about 1500 K. At the sublimation radius (~ 0.3 AU), the “inner rim” is illuminated by the central star at about a 90° angle and is expected to be much hotter than the disk behind it. Consequently it should have a larger, hydrostatically supported scale height (i.e. be “puffed-up”).

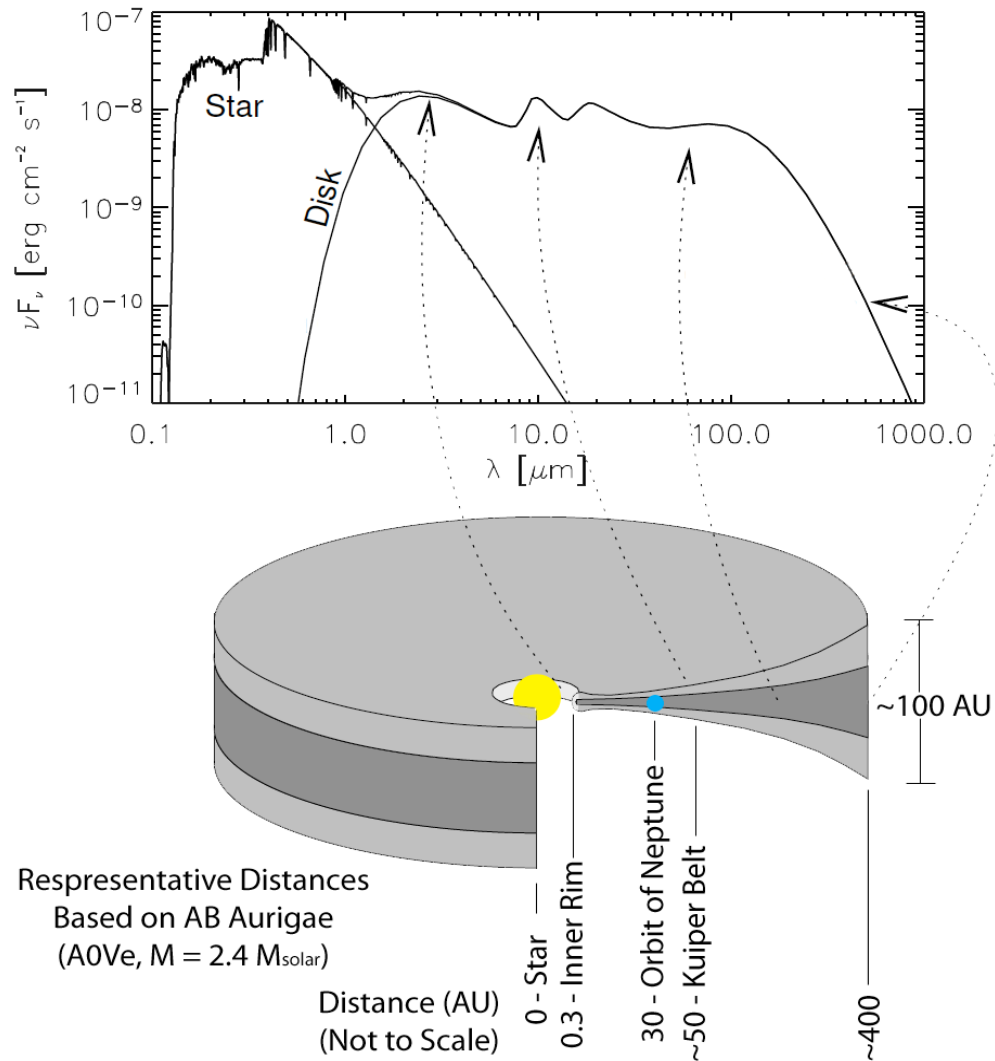


Figure 1.5. SED model and distance scale for a young protoplanetary flared disk.

Typical flared protoplanetary disks with no gaps produce a relatively flat SED out beyond $\sim 100 \mu\text{m}$ (depending on the degree of flaring and the physical extent of the disk). The NIR bump comes from the inner rim that is directly illuminated by the star. The mid-IR to FIR is from the warm upper dust layers of the disk. The FIR to millimeter emission comes mostly from the disk midplane in the outer regions of the disk. Representative distances are for AB Aur and are not to scale. Scattering is not included (after Dullemond et al. 2006).

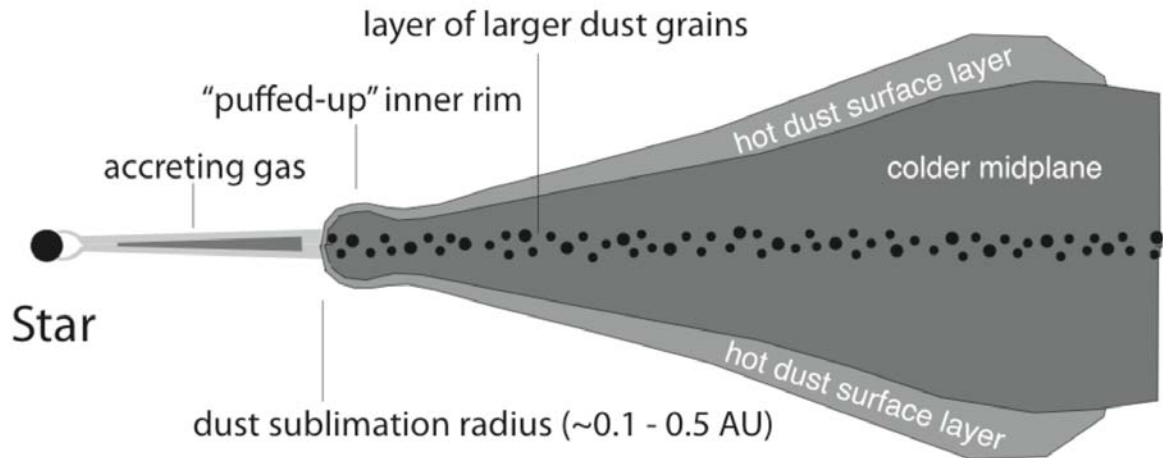


Figure 1.6. Vertical dust structure of a flaring protoplanetary disk.

As disks age, dust grains grow in size and settle toward the midplane. The very inner part of the disk is dust-free due to dust sublimation above temperatures of about 1500 K. At the sublimation radius, the “inner rim” is illuminated by the star at about a 90° angle and is expected to be much hotter than the disk behind it. Consequently it should have increased scale height (i.e. be “puffed-up”). Gas exists in the dust layers but is not shown for simplicity (after Dullemond et al. 2006).

1.3.2 Transitional Disk Phase

Transitional disks have properties indicating an intermediate phase of disk evolution. They have SEDs that are similar to protoplanetary disks at wavelengths longer than $\sim 10 \mu\text{m}$, but have significantly less IR excess at shorter wavelengths (Figure 1.7b). These SEDs imply the presence of an optically thin inner region (~ 1 to 20 AU) that is surrounded by an optically thick outer disk (Strom et al. 1989; Najita et al. 2007). Thus, the definition includes both objects with no dust within some disk radius and objects with optically thin inner dust disks. Transitional disks have accretion rates that are a factor $\sim 10 - 100\times$ less than comparable protoplanetary disks, and they have evolved from

radially continuous optically thick disks at birth to optically thick disks with an optically thin inner region (or gap) by ~ 10 Myr.

Transitional SEDs can be explained by multiple evolutionary paths. A transitional SED could arise as grains in the inner disk grow into larger bodies, thereby creating an optically thin inner disk region (Strom et al. 1989). Alternatively, a transitional SED may arise through the creation of a large gap as the result of the dynamical isolation of the inner and outer disks by a sufficiently massive giant planet (Skrutskie et al. 1990).

Photoevaporation has also been suggested as an explanation of transitional disk SEDs (Clarke et al. 2001; Alexander et al. 2006). In the surface layers of the disk, irradiation by UV and X-ray photons from the star can cause the gas temperature to become very high, greatly exceeding the dust temperature. In a process called “photoevaporation”, the thermal velocity of the gas in the surface layers exceeds the escape velocity, and warm surface gas and small dust particles can escape the gravity of the star. When the disk accretion rate at the photoevaporation radius (~ 20 AU) becomes less than the disk photoevaporation rate, the region is losing more material via photoevaporation than it is gaining via accretion from the outer disk, and the resupply of material to the inner disk is cut off. The remaining material in the inner disk accretes on to the star, leaving behind a large inner gap devoid of gas and dust (Clarke et al. 2001).

In an alternate scenario, the combination of gas loss through photoevaporation and large dust grain settling could produce a gas-to-dust ratio in the disk midplane that may become low enough to meet the gravitational instability criteria of Youdin and Shu (2002) (i.e. a gas:dust ratio of $\sim 20:1$, down by a factor of ~ 5 from the characteristic protoplanetary disk gas:dust ratio of $\sim 100:1$), indicating that planetesimals (kilometer-

sized objects) could spontaneously form. These results imply that photoevaporation may even trigger the formation of planetesimals which could create an optically thin inner disk region (Dullemond 2006).

Although the evolutionary path to the transitional SED cannot be uniquely determined from the SED alone, knowledge of the accretion rate can often help narrow the possibilities.

1.3.3 Debris Disk Phase

Debris disks represent a final stage of disk evolution, are generally devoid of detectable gas (Coulson et al. 1998), and have very little to no detectable IR excess at wavelengths shorter than $\sim 10 \mu\text{m}$, while still maintaining moderate levels of IR excess at wavelengths longer than $\sim 10 \mu\text{m}$ (Figure 1.7c). While protoplanetary disks consist of a primordial mix of interstellar gas and dust (gas to dust ratio of 100:1), debris disks are believed to consist primarily of second-generation dust created by collisions of larger bodies in the system (e.g. Zuckerman 2001). Dust grains have now grown to rocks, protoplanets, and terrestrial planets. Accretion has stopped and the lack of NIR excess is indicative that no inner disk exists at all.

1.4 Meeus Groups

Meeus et al. (2001) studied 14 Herbig Ae/Be stars and classified them into two groups depending on characteristics of their SEDs at mid-IR wavelengths. Meeus Group I sources have a mid-IR continuum which can be modeled by a power-law plus a black body, and Meeus Group II sources need only a power-law to fit their mid-IR continuum (Figure 1.8).

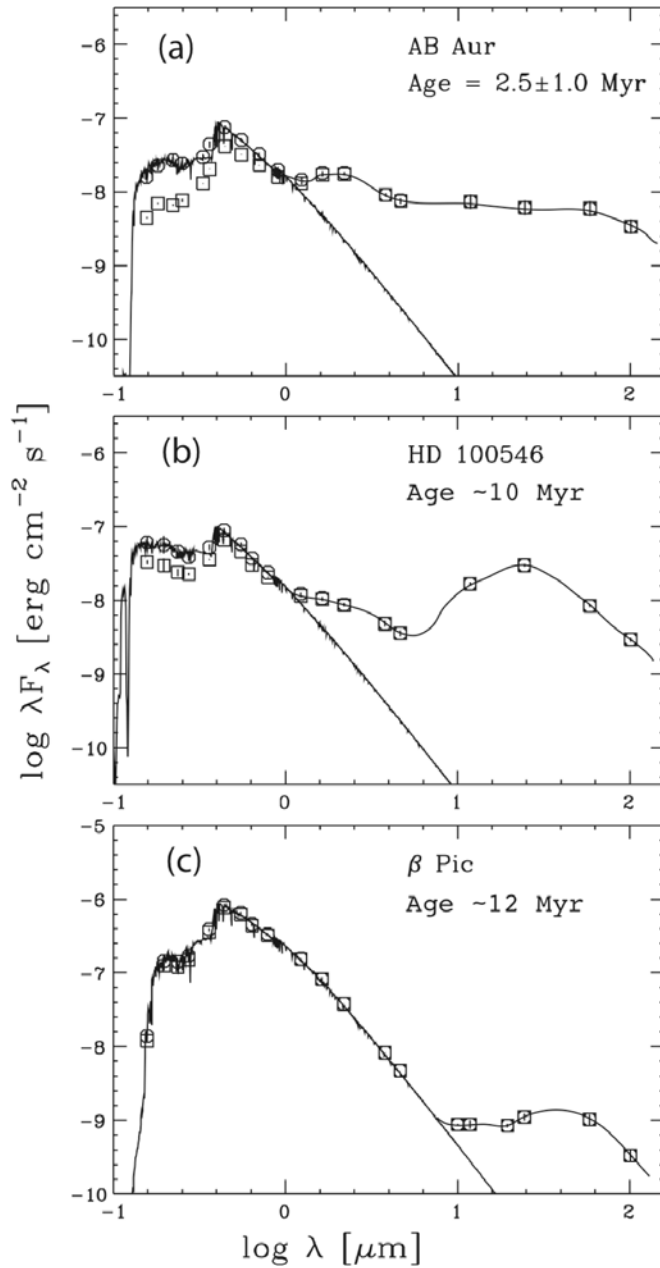


Figure 1.7. SED comparisons for 3 phases of Herbig Ae/Be star disk evolution.

Observed (squares) and extinction-corrected (circles) SEDs for (a) AB Aur and its protoplanetary disk, (b) HD 100546 and its transitional disk, (c) β Pic and its debris disk. Also shown are Kurucz (1991) models fitted to the extinction-corrected SEDs (after van den Ancker 1999).

Meeus et al. (2001) suggested that the two groups could be explained by the following physical characteristics of the disks, which are shown in Figure 1.9. They propose that the disks of both groups consist of three components: (a) an optically thick, geometrically thin disk that extends throughout the inner disk to the outer disk, and which forms at an early stage; (b) a partially optically thin inner disk about 10 AU in radius with an increased scale height which may shield the outer part of the disk; (c) an outer disk that can flare if exposed to the stellar radiation. The controlling physical difference between the two groups is suggested to be in the inner disk. For the Meeus Group I sources, the scale height of the optically thick part of the inner disk is low, and the outer disk is illuminated by the star and it warms and flares (Figure 1.9, top panel). The flaring in the outer disk is responsible for the black body component in the mid-IR for the Meeus Group I SEDs. For Meeus Group II sources, the scale height of the optically thick part of the inner disk is high, and the outer disk is shielded from the star. The outer disk does not flare, and no black body component is needed to fit the mid-IR of the Meeus Group II SEDs (Figure 1.9, bottom panel). The lack of a flared region suggests the Group II disks are more evolved than the Group I disks (Meeus et al. 2001).

The two groups also differ in the amount of total IR excess luminosity. Meeus et al. (2001) also found that the ratio of total IR excess luminosity to total stellar luminosity, L_{IR}/L_* , is on average 0.52 and 0.17 for groups I and II, respectively. Since a star's total IR excess is expected to decrease as grains grow (Beckwith et al. 1990), Meeus et al. (2001) suggest that Group I sources may evolve to Group II sources (i.e. the Group I sources are younger than the Group II sources).

When comparing grains from similar regions of a disk, larger grains radiate at longer wavelengths than smaller grains. Therefore, large grains tend to create shallower slopes in the sub-millimeter than small grains. Meeus et al. (2001) measured the average sub-millimeter slope for the two groups and found that Group II sources have a shallower slope than Group I sources (-2.8 versus -3.6). This suggests that the Group II sources should have, on average, larger grains and should, therefore, be older than the Group I sources.

1.5 Thesis Goal and Approach

Although Meeus et al. (2001) discuss three indicators (mid-IR blackbody component, fraction of total IR excess, sub-millimeter SED slope) that suggest Group I sources evolve to Group II sources, four of the eight Group I sources do not have age estimates in the Meeus et al. (2001) paper. **The goal of this thesis is to test the idea that Meeus Group I sources evolve to Meeus group II sources.** The approach will be to study Group I sources in the Meeus et al. (2001) paper that do not have age estimates. One of them is HD 169142, which has been previously studied by this author in Grady et al. (2007), and the age has been estimated to be 6^{+6}_{-3} Myr. Two others are HD 135344 and HD 139614, for which van Boekel et al. (2005) coarsely estimated ages of 8^{+8}_{-4} Myr and >10 Myr, respectively. The fourth star in Meeus Group I without an age determination is HD 100453, and it will be the primary focus of this work. HD 100453 has a candidate low-mass stellar companion that was reported by Chen et al. (2006). Because a low-mass companion can be used to better constrain the age of a primary Herbig Ae star (see below), confirmation of the candidate companion as a physical companion will be attempted first. Then the age and accretion rate will be determined

and compared to the other sources to determine if the Group I to Group II evolution hypothesis is supported.

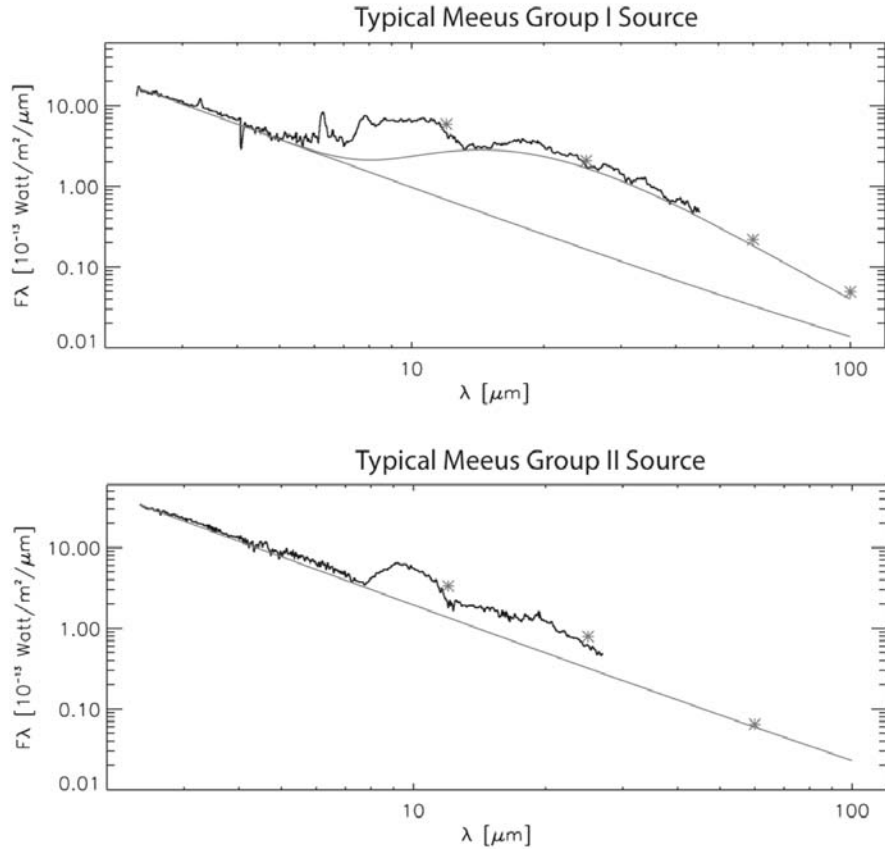
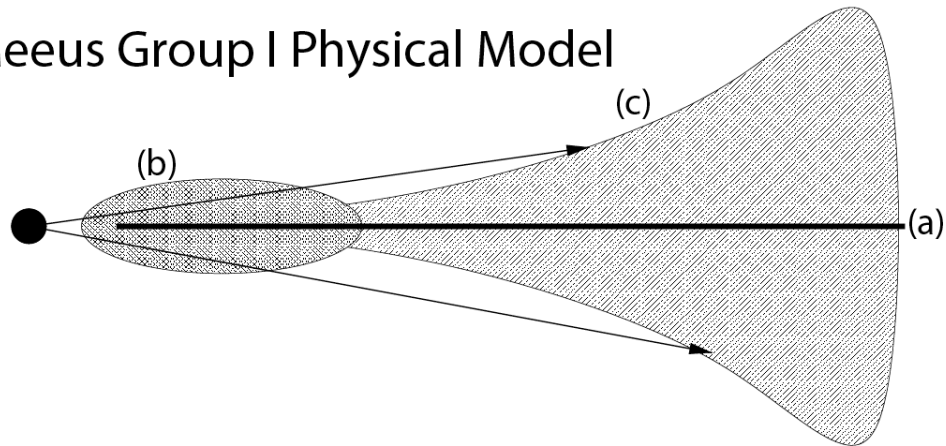


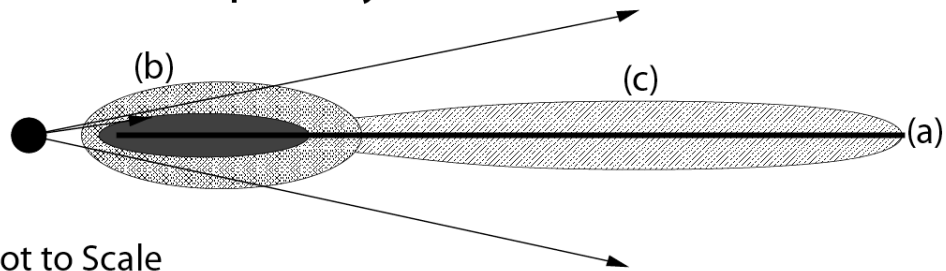
Figure 1.8. Meeus Group I and Group II determination.

The top panel is an example of a Meeus Group I source (HD 179218) in $\log F_\lambda$ versus $\log \lambda$ space. A power law (the straight line in \log - \log space) and a black body are required to fit the continuum of the Group I source. The bottom panel is an example of a Meeus Group II source (HD 150193) requiring only a power-law to fit the continuum. Dark line: Infrared Space Observatory (ISO) Short Wavelength Spectrometer (SWS) spectrum of source; straight light line: power-law fit to continuum; curved light line: sum of power-law and black body fit to continuum; asterisks: Infrared Astronomical Satellite (IRAS) fluxes (after Meeus et al 2001).

Meeus Group I Physical Model



Meeus Group II Physical Model



Not to Scale

Figure 1.9. Meeus Group I and Group II physical models.

Both physical models (not to scale) consist of three components: (a) an optically thick, geometrically thin disk; (b) a partially optically thin inner disk with an increased scale height which may shield the outer part of the disk; (c) an outer disk that can flare if exposed to the stellar radiation. The upper panel shows the case for a mostly optically thin inner disk (Group I). The star illuminates the outer disk surface and causes thermally induced flaring and thus a black body component in the mid-IR of the SED. The lower panel shows a partially optically thick inner disk (Group II) which shields the outer disk from direct stellar radiation, so it does not flare nor generate a black body component in the mid-IR of the SED (after Meeus et al. 2001).

1.6 Characteristics of HD 100453

HD 100453 is also known as IRAS 11307–5402, SAO 239162, HIP 56354 in the literature and has a spectral type of A9Ve (Houk & Cowley 1975). Meeus et al. (2002) suggest that HD 100453 is close to the zero age main sequence (ZAMS) and estimate the age to be ≥ 10 Myr, and the star appears to be a member of the Lower Centaurus Crux Association (Kouwenhoven et al. 2005), which suggests an upper limit for the age of about 20 Myr (Mamajek et al. 2002). These and other characteristics are compiled in Table 1.2. Chen et al. (2006) reported a candidate companion at a projected angular separation of $1''.05$. Hereafter, the candidate companion is also referred to as HD 100453B, star B, the secondary object, or just the secondary.

1.7 Age Determination Techniques

The age of a young star can be estimated by locating it on the pre-main sequence (PMS) tracks of a Hertzsprung-Russell (H–R) diagram. The H–R diagram is developed from theoretical stellar models, and locating a star on it requires knowledge of the star's effective temperature and luminosity. The effective temperature can be estimated from a star's spectral type and the luminosity from its distance and apparent magnitude. Once located on the H–R diagram, a star's age and mass can be determined by examining its position relative to the H–R diagram's isochrones and mass tracks.

Table 1.2Summary of HD 100453A Previously Known Characteristics

Characteristic	Value	Units/System	Reference
Right Ascension	11:33:05.577	FK5	Perryman et al. (1997)
Declination	-54:19:28.54	FK5	Perryman et al. (1997)
Parallax	8.97 ± 0.76	mas	Perryman et al. (1997)
Distance	114^{+11}_{-9}	pc	calculated from parallax
Proper Motion (μ_α)	-36.95 ± 0.78	mas/yr	Perryman et al. (1997)
Proper Motion (μ_δ)	-4.72 ± 0.53	mas/yr	Perryman et al. (1997)
Spectral Type	A9Ve		Houk & Cowley (1975)
Radial Velocity	17	km/s	Acke et al. (2005)
Projected Rotational Velocity ($v \sin i$)	39 ± 4	km/s	Acke and Waelkens (2004)
Age Lower Limit	~10	Myr	Meeus et al. (2002)
Age Upper Limit	~20	Myr	Mamajek et al. (2002)
Mass	1.7	M_\odot	Dominik et al. (2003)
B-band	8.07	mag	Vieira et al. (2003)
V-band	7.78	mag	Vieira et al. (2003)
J-band	6.945 ± 0.026	mag	Cutri et al. (2003)
H-band	6.390 ± 0.038	mag	Cutri et al. (2003)
K-band	5.600 ± 0.021	mag	Cutri et al. (2003)
Variability Amplitude	0.084 ± 0.014	mag	Perryman et al. (1997)

Age estimates have proven problematic for Herbig Ae/Be stars, due to the rapid evolution of the star to the Zero-Age Main Sequence. In practice, reliable dating of isolated A stars is difficult after about 5 Myr (Stauffer 2004). However, low-mass M-type stars move through the H–R diagram much more slowly and can be dated with some accuracy out to ~50 Myr. The identification of M-type star physical companions associated with A stars (e.g. Zuckerman & Song 2004) permits a more accurate dating of the A star, since it is believed that stars which formed out of the same contracting cloud were born coevally. As an example, Figure 1.10 illustrates the PMS H–R diagram for HD 169142 and one of its M-type physical companions. In practice, the luminosity of the A star makes optical detection of low-mass companions within 10" difficult. However, the combination of high angular resolution imaging and multi-wavelength data has revealed low-mass companions to several Herbig Ae stars (e.g. Weinberger et al. 2000; Grady et al. 2004; Feigelson et al. 2006; Chen et al. 2006; Carmona et al. 2007; Grady et al. 2007).

1.8 Instrumentation Requirements

We will use several techniques to study HD 100453A and its environment. In the optical and IR, high contrast, high spatial resolution imaging is required to detect the faint objects near an extremely bright star. As will be discussed, sub-millimeter and millimeter imaging does not require the high contrast capability.

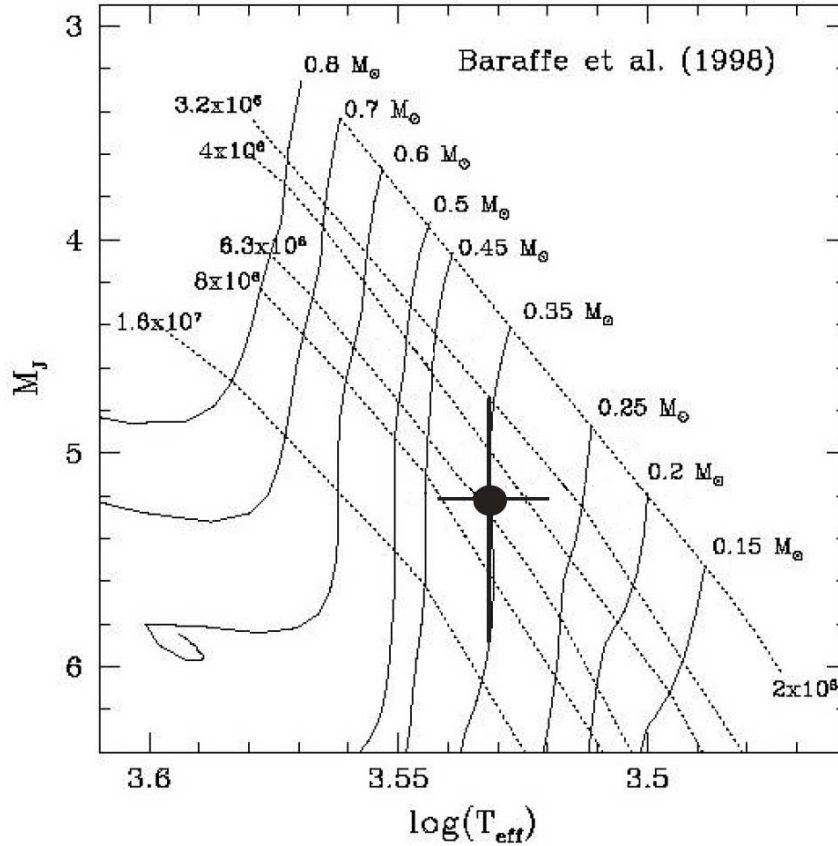


Figure 1.10. H–R diagram for HD 169142.

The H–R diagram was generated from the theoretical models of Baraffe et al. (1998). The mass tracks (solid lines) and isochrones (dotted lines, in years) are shown relative to the J-band absolute magnitude (the J–band filter is centered at $1.215 \mu\text{m}$ and has a FWHM of $0.26 \mu\text{m}$) and the effective temperature. The location of one of the low-mass companions to HD 169142 is marked by the large filled circle and the error bars are indicated by the large cross. Comparing the error bars to the isochrones, it can be seen that the companion, and therefore HD 169142 (see text) have an estimated age of 6^{+6}_{-3} Myr. The error bars in M_J are dominated by the distance uncertainties for HD 169142. The error bars in $\log T_{\text{eff}}$ are dominated by spectral type to effective temperature conversion (after Weinberger et al. 2000; Grady et al. 2007).

1.8.1 High Spatial Resolution Spectroscopy

For an age determination, the spectral type of the candidate companion is needed. Since Chen et al. (2006) report that the angular separation of the candidate companion from the primary is only $1''.05$, high spatial resolution spectroscopy is needed to separate the light of the primary from the secondary. Ground-based astronomy is usually limited to a resolution of about $0''.5 - 1''.0$ because of atmospheric distortion (astronomical seeing). However, an adaptive optics (A/O) unit can significantly increase spatial resolution by measuring the atmospheric distortion and rapidly compensating for it either using deformable mirrors or material with variable refractive properties.

The first choice for determining the spectral type is to obtain optical spectra, but there are no large ground-based telescopes with A/O in the optical. However, the spectral type can also be determined from NIR spectra, and large telescopes with A/O in the NIR are available. The VLT SINFONI integral field NIR spectrograph (Eisenhauer et al. 2003, Bonnet et al. 2004) can be configured to provide a field of view of less than $1'' \times 1''$ and is fed by an A/O unit. It is therefore an ideal instrument for collecting spectra to determine the candidate companion's spectral type. Chen et al. (2006) provide the photometric data we need to determine the luminosity required for locating the candidate companion on the H–R diagram.

1.8.2 High Spatial Resolution Photometry

To determine if the candidate companion is a physical companion to HD 100453A, one needs to verify that the proper motions of the two objects is the same. This can be difficult because the contrast ratio between the A-type star and M-type star, in the optical, is $\sim 1500:1$. By moving to NIR wavelengths, the contrast ratio is reduced to

about $\sim 100:1$ because the peak of the black body radiation curve moves to longer wavelengths as the effective temperature decreases (see Figure 1.3). Since the proper motion of stars at 114 pc is expected to be small ($\sim 50 \text{ mas yr}^{-1}$), one needs high spatial resolution imaging. The VLT NACO adaptive optics instrument (Lenzen et al. 2003; Lagrange et al. 2003) can meet both of these needs, and furthermore, because it was used previously by Chen et al. (2006), instrument-to-instrument variations in positional determination will not be a concern when comparing two epochs of data.

1.8.3 Coronagraphic Imaging and psf-Subtraction

To investigate the disk environment of HD 100453A, one needs techniques to deal with even higher contrast ratios than mentioned above. First, coronagraphy will be utilized, which involves simply placing an opaque, small diameter circular “spot” over the bright object in the field. The spot blocks out much of the light from the offending star, but some diffracted and reflected light still contaminates the field of view. To reduce this contamination, the effects of the point spread function (psf) must be minimized.

The psf describes the response of a telescope and its instrumentation to a point source of light in its field of view. In practice, the instrument’s psf changes an incoming point source’s light into an extended blurry spot. Deconvolution techniques can be used to mathematically reduce the effects of the psf. However, in practice, the physical characteristics of the reflecting and refracting surfaces in a telescope cannot be determined with enough accuracy to obtain the level of contrast needed to image circumstellar disks around A-type stars ($\sim 1 \times 10^6$). To achieve this, one can turn to a technique referred to as psf-subtraction, which involves coronagraphically imaging the star under study (the target star) and a standard star with a spectral type similar to the

target star and without a disk (the psf-star). The spectral types should be similar because the psf is wavelength-dependent. The brightness level of the psf-star image is scaled to account for any differences in distance and luminosity between the psf-star and the target star, and the psf-image is shifted to align the two stars in a common image frame. Finally, the scaled and shifted coronagraphic psf-image is subtracted, pixel by pixel, from the coronagraphic target image.

The psf-subtraction technique greatly reduces the measured flux from the star under the coronagraph, but leaves other objects in the field, such as a circumstellar disk or faint companion, relatively unchanged. However, for coronagraphic psf-subtraction to be most effective, one needs to eliminate differences in the two images due to atmospheric changes. For this capability, the Hubble Space Telescope (HST) is ideal because it can be used to obtain coronagraphic images from space (Pavlovsky et al. 2006b).

The HST coronagraphic capability utilized in this thesis is provided by the Advanced Camera for Surveys (ACS) High Resolution Camera (HRC). This instrument provides coronagraphic imagery with a pixel scale of $0''.025 \text{ pixel}^{-1}$, occulter spot sizes of $0''.9$ and $1''.8$ in radius, and a contrast ratio of $\sim 1 \times 10^6$ (with psf-subtraction) at $\sim 1''$ from the central star. Figure 1.11 demonstrates the contributions to contrast improvement for the coronagraph alone and the coronagraph with psf-subtraction. The disk is difficult to detect in the coronagraphic image (top-left panel), but in the psf-subtracted image, the disk and even disk structure are easily detected. In the range of $1'' - 2''$ from the central star, the HRC camera provides contrast capabilities of $\sim 1 \times 10^5$ in direct mode, $\sim 1 \times 10^6$ in coronagraphic mode, and $\sim 1 \times 10^7$ in coronagraphic mode with psf-subtraction.

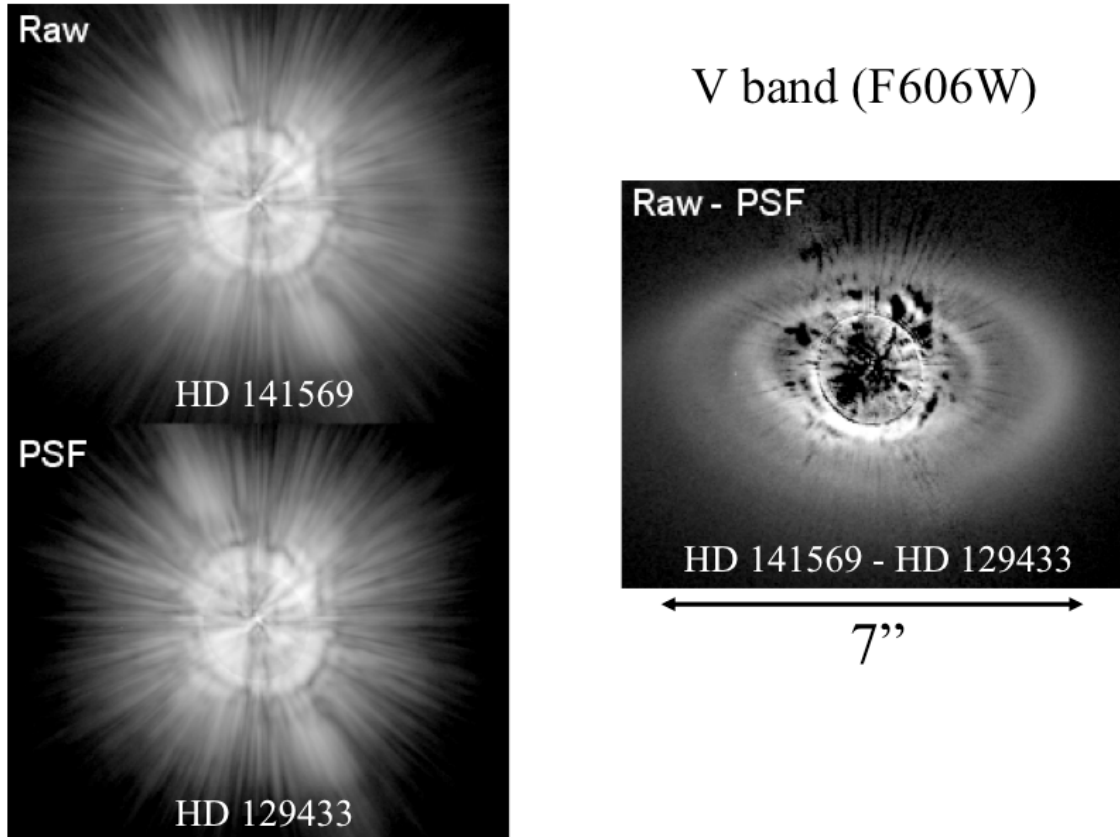


Figure 1.11. Demonstration of ACS coronagraphic imaging performance.

The top-left panel is a coronagraphic image of HD 141569 (the target star without psf-subtraction). The bottom-left panel is a coronagraphic image of HD 129433 (the psf-star). The right panel is the result of subtracting, pixel by pixel, the HD 129433 image from the HD 141569 image. The psf-subtracted image provides clear evidence of a disk and even structure within the disk (after Clampin et al. 2003).

1.8.4 Sub-millimeter Photometry

The literature provides limits on warm and hot molecular gas in the disk of HD 100453A (Carmona et al. 2008), as well as 1.2 mm photometry (Meeus et al. 2002, 2003) that can be used to estimate the dust mass. However, one needs to also understand

the limits on cold gas mass in the disk midplane and in the outer parts of the disk. Cold ($\sim 20 - 100$ K) gas and dust radiate energy in the sub-mm to mm wavelength range. However, stars have negligible radiation at these wavelengths, and therefore coronagraphs are not required. Estimates of cold gas mass in the environment of a star can be determined by observing CO line emission at $868 \mu\text{m}$ in the submillimeter. The Heterodyne Array Receiver Program (HARP) (Dent et al. 2000) at the James Clerk Maxwell Telescope (JCMT) is a sensitive instrument for such measurements.

1.8.5 FUV and X-ray Spectroscopy

Finally, the rate at which mass is accreting from the disk onto the primary star needs to be constrained. Since one cannot measure this rate directly, it is best determined by correlating multiple accretion rate indicators. Accretion is the primary source of Far-Ultraviolet (FUV) continuum detected toward Herbig Ae stars, and it contributes to hard (short wavelength) X-ray production. To determine the accretion rate, one needs to obtain FUV spectra and measure the level of FUV continuum in a line-free region of the spectra. X-ray spectroscopy is also necessary to determine the hardness of the X-ray emission (the relative amount of flux of shorter wavelength X-rays vs. longer wavelength X-rays). However, the atmosphere absorbs most FUV and X-ray radiation before it reaches the ground, so one must utilize space-based instruments for these observations. The Far-Ultraviolet Spectroscopic Explorer (FUSE) can be used to collect FUV spectra, and the Chandra X-ray observatory with the ACIS-S detector (Garmire et al. 2003) can be used to collect X-ray spectra ($E/\Delta E = 10 - 60$).

1.8.6 Summary of Instrumentation

Table 1.3 provides a summary of the instrumentation used in this work, along with an indication of the type of data collected (direct image, coronagraphic image, or spectra), the wavelength range of interest, and the scientific purpose for the data. Detailed information is provided for each instrument in § 2.2.

Table 1.3

Summary of Instrumentation

Instrument	Direct Image	Coron. Image	Spectra	Wave-length	Scientific Purpose
Chandra	✓		✓	X-ray	Accretion Rate
HST ACS HRC	✓			Optical	Companion Location & Photometry
HST ACS HRC		✓		Optical	Disk Detection & Photometry
HST ACS SBC	✓			FUV	Companion Detection
VLT NACO		✓		NIR	Companion Proper Motion & Photometry
VLT SINFONI			✓	NIR	Spectral Type of Companion
FUSE			✓	FUV	Accretion Rate
Phoenix			✓	NIR	Warm Gas Limits
JCMT HARP			✓	Sub-mm	Cold Gas Limits
FEROS			✓	Optical	Accretion Rate

2. THE DISK AND ENVIRONMENT OF HD 100453

This section and associated subsections will be submitted to the Astrophysical Journal for publication. The coauthor names and affiliations are listed below and the contributions of each are listed in the Acknowledgements section. The title of the journal paper will be similar to the title of this thesis.

K. A. Collins^{1,2}, C. A. Grady³, K. Hamaguchi^{4,5}, J. P. Wisniewski^{6,7},
S. Brittain⁸, M. Sitko⁹, W. J. Carpenter¹⁰, G. M. Williger^{1,2},
R. van Boekel¹¹, A. Carmona^{12,11,13}, M. E. van den Ancker¹³, G. Meeus¹⁴,
J. P. Williams¹⁵, G. S. Mathews¹⁵, X. P. Chen¹¹, R. Petre⁶,
B. E. Woodgate⁶, Th. Henning¹¹

¹ Department of Physics and Astronomy, University of Louisville, Louisville, KY 40292

² Kentucky Space Grant Consortium Fellowship under NASA National Space Grant College and Fellowship Program Grant NNG05GH07H

³ Eureka Scientific and GSFC, 2452 Delmer, Suite 100, Oakland CA 96002

⁴ CRESST and X-ray Astrophysics Laboratory NASA/GSFC, Greenbelt, MD 20771

⁵ Department of Physics, University of Maryland, Baltimore, MD 21250

⁶ NASA Goddard Space Flight Center, Greenbelt, MD 20771

⁷ NPP Fellow

⁸ Clemson University, Clemson, SC, 29634

⁹ SSI, University of Cincinnati

¹⁰ University of Cincinnati

¹¹ Max-Planck-Institut für Astronomie, Königstuhl 17, 69117 Heidelberg, Germany

¹² ISDC & Geneva Observatory, chemin d'Eccogia 16, 1290 Versoix Switzerland

¹³ European Southern Observatory, Karl Schwarzschild Strasse 2, 85748 Garching bei München, Germany

¹⁴ Astrophysikalisches Institut Potsdam (AIP), An der Sternwarte 16, 14482 Potsdam, Germany

¹⁵ Institute for Astronomy, University of Hawaii, 2680 Woodlawn Dr., Honolulu, HI 96822

2.1. Introduction

In the following subsections of this section, we utilize observations from the X-ray to the sub-millimeter and present a multi-wavelength study of the HD 100453 system. We investigate the photometry, proper motion, and spectral type of the candidate companion in an effort to confirm the binary hypothesis and refine the age of the system. We also investigate the disk environment of HD 100453A and attempt to constrain the accretion rate, gas content, dust content, and structure of the disk.

Observations and data reduction are described in § 2.2, and the results are detailed in § 2.3. Discussion of the disk and environment of HD 100453A is in § 2.4 and a brief summary is presented in § 2.5.

2.2. Observations and Data Reduction

We have obtained Chandra ACIS-S X-ray imagery, Hubble Space Telescope ACS HRC optical coronagraphic and non-coronagraphic imagery and SBC FUV non-coronagraphic imagery, FUSE FUV spectroscopy, VLT NACO NIR imagery, VLT SINFONI NIR spectroscopy, Gemini South Phoenix echelle NIR spectroscopy, ESO 1.52 m telescope FEROS echelle spectroscopy, and James Clerk Maxwell Telescope Heterodyne Array Receiver Program (HARP) 868 μm spectroscopy. These data are supplemented by VLT K_s and $\text{Br}\gamma$ imagery from Chen et al. (2006), PAH (Polycyclic Aromatic Hydrocarbons) data from Habart et al. (2006), 1.2 mm photometry from Meeus et al. (2002, 2003), archival International Ultraviolet Explorer (IUE) data, and archival Spitzer Space Telescope Infrared Spectrograph (IRS) data.

2.2.1 Imagery

2.2.1.1 Chandra ACIS-S Imagery

HD 100453 was observed by the Chandra X-Ray Observatory as part of the Chandra Cycle 7 program P07200493 (Grady, PI) on 2006 March 10 for 9.7 ksec (sequence ID: 200403) using the Advanced CCD Imaging Spectrometer (ACIS: Garmire et al. 2003). To ensure the highest soft energy response, HD 100453 was placed at the ACIS-S aimpoint, and data were obtained using the default $8.3' \times 50.6'$ field of view. When used as an imager in this configuration, ACIS-S has a resolution of $0''.5$ (FWHM) and obtains pulse height spectra from 0.3 – 8.0 keV.

For analysis, we used the CIAO¹⁶ software package ver. 3.4 (CALDB ver. 3.3.0.1) and generated response matrices and auxiliary files using `psextract` and `mkacisrmf`. To improve the spatial resolution, we utilized the sub-pixel event repositioning (SER) algorithms (Tsunemi et al. 2001; Li et al. 2003, 2004).

For the absolute position determination of the Chandra image frame, we cross-correlated the X-ray sources detected on the same backside-CCD chip (ID=7) with the 2MASS All-Sky Point Source Catalog, Second Incremental Data Release¹⁷. Among 8 X-ray sources other than HD 100453 detected with the `wavedetect` package at above the 4σ significance, 2 sources have 2MASS counterparts. The average offset of the Chandra image is less than $0''.1$ from the 2MASS frame without any positional correction.

We generated a sky coordinate image with a fine spatial resolution of $0''.125$ pixel⁻¹ (Figure 2.1). There are two peaks, each of which corresponds to the position of HD 100453A (NW peak) and to the candidate companion, HD 100453B (SE peak),

¹⁶<http://xc.harvard.edu/ciao/>

¹⁷<http://www.ipac.caltech.edu/2mass/releases/allsky/doc/>

respectively. The color-coded image clearly shows that HD 100453B has harder emission. The image also shows apparent tail structures around either source toward the NW (HD 100453A) and NE-SW (HD 100453B) directions. The point spread function itself does not have such a structure, but we cannot confidently say if the structures are real, considering unknown factors in the image reconstruction process and limited photon statistics.

We extracted X-ray events from a circle with a $0''.6$ radius from each peak (Figure 2.1), which includes $\sim 81\%$ of the total flux from a point source based on a psf image at 0.8 keV generated with `mkpsf`. A total of 51 counts were extracted for HD 100453A and a total of 52 counts were extracted for HD 100453B in the 0.3 – 8 keV energy range. Neither source showed significant time variation during the observation. We extracted an X-ray spectrum of each source from the same source region and subtracted background obtained from a surrounding source free region. Neither of the spectra can constrain the H I column density (N_{HI}) due to the limited photon statistics. Since both stars have small optical extinction, $E(B - V) < 0.08$ (Malfait et al. 1998), we assumed a thin-thermal plasma model (APEC¹⁸ code), without X-ray absorption in the spectral fits. The fitting result and spectra are shown in Table 2.1 and Figure 2.2, respectively. Both sources fit as single temperature, unabsorbed models. The intrinsic X-ray flux increases by 50% for $kT \sim 0.3$ keV plasma ($T \sim 3500$ K) between 0.35 – 2 keV if $N_{\text{HI}} = 6.8 \times 10^{21} \text{ cm}^{-2}$, equivalent to $E(B - V) = 0.08$ (Ryter 1996). We were also able to fit single temperature, absorbed models with $E(B - V) < 0.75$ for the primary star and

¹⁸<http://cxc.harvard.edu/atomdb>

$E(B - V) < 1.24$ for the candidate companion, with comparable reduced χ^2 results. Either model fits satisfactorily.

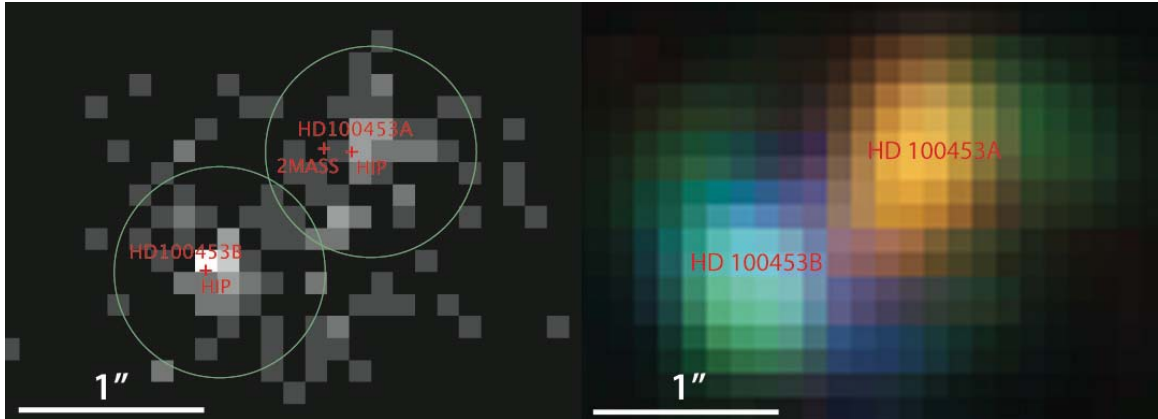


Figure 2.1. Chandra X-ray Imagery of the HD 100453 system.

Left: X-ray image of HD 100453 between 0.35 – 2 keV. Each pixel has $0''.125 \text{ pixel}^{-1}$.

The green circles with $0''.6$ radii show event extraction regions of HD 100453A and HD 100453B. Red crosses show positions of HD 100453A measured with Hipparcos (designated as HIP) and 2MASS (designated as 2MASS). The position of HD 100453B was calculated from the *HIPPARCOS* position of HD 100453A and the separation and position angle in Chen et al. (2006). *Right:* Color-coded X-ray image of HD 100453. The image is smoothed with a Gaussian function with $\sigma = 2$ pixels and color coded in the linear scale to represent 0.35 – 0.7 keV in red, 0.7 – 0.9 keV in green and 0.9 – 2 keV in blue.

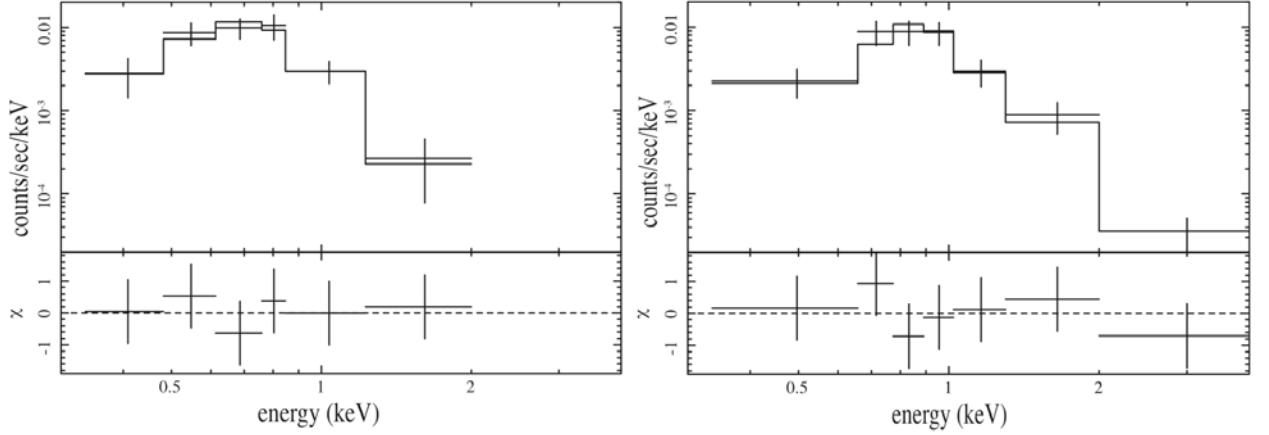


Figure 2.2. Pulse height spectrum of HD 100453A and HD 100453B.

(left) Pulse height spectrum of HD 100453A together with normalized residuals from the single temperature model fit below. The pulse height spectrum is soft, similar to 51 Eri (Feigelson et al. 2006) and typical of X-ray production in winds. (right) Pulse height spectrum of HD 100453B together with normalized residuals from the single temperature model fit below. The pulse height spectrum is harder than for HD 100453A and is typical of a T Tauri star.

Table 2.1

Summary of X-ray Spectral Fit Parameters

	HD 100453A	HD 100453B	Units
kT Peak (kT Range)	.29 (0.24-0.36)	.70 (0.49-0.84)	keV
{Model Parameters}			
F_x^a (0.3-2 keV)	2.7	2.3	10^{-14} ergs cm^{-2} s^{-1}
L_x^a (0.3-2 keV)	6.8	5.7	10^{28} ergs s^{-1}
$\chi^2/\text{d.o.f.}$ (d.o.f.)	0.22 (4)	0.43 (5)	

^adivided by 0.81 from the encircled flux within $0''.6$ circle

2.2.1.2 HST ACS/HRC Imagery

HD 100453 was observed using the coronagraphic mode of the High Resolution Channel (HRC) camera of HST's Advanced Camera for Surveys (ACS) as part of the cycle 12 GTO program 9987 on 2003 November 12. The F606W filter imaging was obtained using the ACS 1".8 diameter occulter spot, yielding a 29".2 × 26".2 field of view with a pixel scale of 0".028 × 0".025. The psf of the HRC is 50 mas in V. HD 87427 (F0V), a star of similar spectral type to HD 100453 (A9V), was observed immediately following HD 100453 to serve as a psf reference star. A summary of the basic parameters of our HST/ACS observations is presented in Table 2.2.

Table 2.2

Summary of HST/ACS Observations

Object	Date	Instrument	Mode	Filter	Exp. Time (s)	Comment
HD 100453	12 Nov 2003	ACS/HRC	Direct	F606W	20	
HD 100453	12 Nov 2003	ACS/HRC	Coron	F606W	2480	
HD 87427	12 Nov 2003	ACS/HRC	Coron	F606W	2000	psf-star
HD 100453	7 Jun 2006	ACS/SBC	Direct	F122M	4 × 524	

The standard HST pipeline was used to perform basic initial data reduction procedures. We used the best available calibration files for this processing, including a correction for the different flat field illumination of the region near the coronagraphic spot. To reject cosmic rays, multiple images were combined using standard pipeline techniques. Standard practices were used to subtract psf signatures from our HST ACS

coronagraphic data (Clampin et al. 2003; Golimowski et al. 2006; Wisniewski et al. 2008). Non-distortion corrected images of our psf reference star were first normalized and aligned to HD 100453 in an iterative manner, using a cubic convolution interpolation function. Residual alignment errors in the resultant best subtraction are estimated to be of order ± 0.05 pixels (Pavlovsky et al. 2006a), and our normalization is estimated to be accurate to $\sim 2\%$ (Clampin et al. 2003). Following the subtraction of a fully registered and scaled psf, MultiDrizzle¹⁹ was used to correct our data for the known geometric distortion of the HRC field of view, yielding an image with $0''.025 \times 0''.025$ size pixels.

Next, SYNPHOT, the synthetic photometry package within STSDAS, was used to determine the correction factor needed to calibrate our data to an absolute photometric scale. We used a synthetic stellar spectral model of HD 508 (A9IV), normalized to a V-band magnitude of 7.79, as a template for HD 100453, and a synthetic spectrum of Xi Ser (F0IV), normalized to a V-band magnitude of 5.72, as a template for HD 87427. All psf-subtracted, distortion corrected images were normalized to the synthetic flux of HD 100453. Note that all photometry reported is based on the STMAG photometric system, and photometry extracted from the coronagraphic data have been corrected for the known 52.5% reduction of flux induced by the occulting spot.

2.2.1.3 HST ACS/SBC Imagery

HD 100453 was observed with HST and the Advanced Camera for Surveys Solar Blind Channel in filter F122M (nominal $\lambda_{\text{eff}} = 1210 \text{ \AA}$, $\text{FWHM} = 60 \text{ \AA}$) on 2006 June 7 as part of HST-GO-10764 (Grady, PI). The HD 100453 data, with total integration time of 2096s, were obtained in 4 exposures within a single spacecraft orbit at a spacecraft

¹⁹ <http://stsdas.stsci.edu/multidrizzle/>

orientation of -82.0755° . See Table 2.2 for a summary of the HST/ACS HD 100453 observations.

The known single source white dwarf reference star HS 2027+0651 was observed with HST/ACS/SBC/F122M on 2002 June 9 as part of calibration program 9020 (De Marchi, PI). One exposure of 400 seconds was obtained. HS 2027+0651 was again observed with HST/ACS/SBC/F122M on 2003 March 19 as part of calibration program 9654 (De Marchi, PI). The data, with a total integration time of 2000s, were obtained in 5 exposures within a single spacecraft orbit. The 5 exposures were then stacked (aligned and then averaged on a pixel-by-pixel basis). HS 2027+0651 was observed a third time with HST/ACS/SBC/F122M on 2007 April 30 as part of program 10864 (Grady, PI). One exposure of 402 seconds was obtained. See Table 2.3 for a summary of the white dwarf observations.

Table 2.3

Summary of White Dwarf HS2027+0651 psf Star Observations

Object	Dataset	Program ID	Date	Exp. Time (s)	Comments
HS2027+0651	J8C102WNQ	9020	2002-06-09	400	
HS2027+0651	J8JQ01RYQ	9654	2003-03-19	400	Exposure 1
HS2027+0651	J8JQ01RZQ	9654	2003-03-19	400	Exposure 2
HS2027+0651	J8JQ01S0Q	9654	2003-03-19	400	Exposure 3
HS2027+0651	J8JQ01S1Q	9654	2003-03-19	400	Exposure 4
HS2027+0651	J8JQ01S2Q	9654	2003-03-19	400	Exposure 5
HS2027+0651	J9OS07011	10864	2007-04-03	402	

For each exposure, the field was dithered using the ACS small-box dither pattern (Gonzaga et al. 2005, 2006, with dither offsets of $\approx 0''.15 - 0''.19$) about the SBC-FIX aperture location. The x and y pixel scales are $0''.034 \times 0''.030$ per pixel resulting in a coverage on the sky of $34''.6 \times 30''.8$.

The data were processed using the default ACS pipeline software (NOAO-IRAF FITS Image Kernel July 2003) including geometric distortion correction and the use of the multi-drizzle algorithm to produce a stacked, geometric distortion corrected image (Pavlovsky et al. 2006a). In the final, geometrically corrected imagery, the pixel scale is $0''.025 \times 0''.025$. HD 100453A was placed at the SBC-FIX aperture (Figure 2.3).

The HD 100453 ACS F122M image, after pipeline processing, has a background level of 1.1×10^{-3} counts pixel⁻¹ s⁻¹ with a standard deviation of 1.3×10^{-3} counts pixel⁻¹ s⁻¹. In our image, there are no diffuse features detectable at the 5σ level or higher, and there are no point sources above our point source detection limit, except for the brightest source in the field, HD 100453A, and an optical ghost to the upper left of the HD 100453A (see Appendix for details). We see no statistically significant evidence of the previously reported candidate companion in the F122M imagery. The circle in Figure 2.3 indicates the expected position of HD 100453B.

The 2002, the stacked 2003, and the 2007 white dwarf images were utilized as SBC/F122M psf images. The three psf datasets were each individually shifted to align the white dwarf peaks with the HD 100453 peak. The psf images were then scaled to match the total flux of HD 100453 within about $0''.5$ radius of the peak. The resulting scale factor utilized was 2.2. The scaled, registered psf images were then used to perform psf-subtraction on the HD 100453 image.

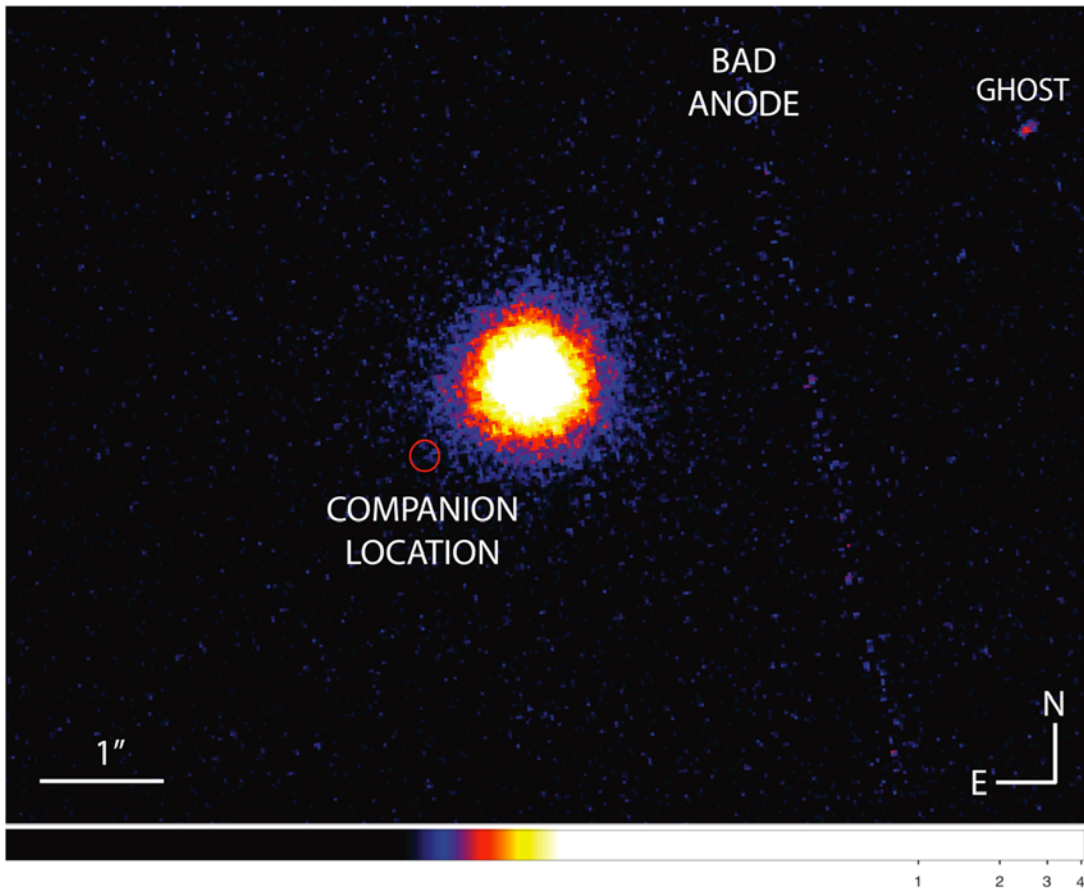


Figure 2.3. FUV image of the HD 100453 system.

A $8''.5 \times 6''.5$ HST ACS SBC image of HD 100453 in the F122M filter (non-coronagraphic), plotted on a *log* scale. The red circle identifies the expected position of the companion. No evidence of the previously reported companion is detected in the F122M FUV filter, suggesting that the companion is non-accreting and outside the disk of the primary.

2.2.1.4 VLT NACO Imagery

HD 100453 was observed with NACO (Lenzen et al. 2003; Lagrange et al. 2003) during the night of 2006 June 22, through the L' -band filter ($3.80 \pm 0.31 \mu\text{m}$), M' -band filter ($4.78 \pm 0.295 \mu\text{m}$), and $\text{Br}\gamma$ narrow band filter ($2.166 \pm 0.01 \mu\text{m}$) with total

exposure times of 4.32 s, 7.84 s, and 10 s, respectively, at an airmass of 1.17 and an ambient seeing of $0''.52$. HD 100453 was previously observed with NACO during the night of 2003 June 2, through the Br γ (2.166 μm) narrow band filter (Chen et al. 2006). A total exposure time of 3.5 seconds was used, at an airmass of 1.15 and an ambient seeing of $0''.9$.

NACO is composed of NAOS, the first Adaptive Optics System on the VLT (Rousset et al. 2003) and CONICA, a 1 – 5 μm imaging, coronagraphic, spectroscopic and polarimetric instrument (Lenzen et al. 1998). For the Br γ data, the S27 camera was used, which provides a pixel scale of 27.15 mas pixel $^{-1}$ and a field of view of about $28'' \times 28''$. Standard pipeline processing was applied, consisting of dark subtraction and flat fielding. For the L'-band and M'-band data, the coronagraphic mode was used with chopping and nodding to reduce the background contamination. In addition, a pupil stop was used for the science observations to reduce stray light. A calibration star was observed in the L'-band and M'-band to facilitate photometry, but without the pupil stop. The science observation photometry includes a reduction of 0.234 magnitudes to account for the pupil stop.

2.2.2 Spectroscopy

2.2.2.1 VLT SINFONI Spectroscopy

HD 100453B was observed with the ESO-VLT Spectrograph for INtegral Field Observations in the Near Infrared (SINFONI) mounted on ESO's UT4 "Yepun" 8m telescope atop Cerro Paranal Chile during the night of 2007 May 19 (Carmona, PI). SINFONI is a near-infrared (1.1 – 2.45 μm) integral field spectrograph fed by an adaptive optics module, installed at the Cassegrain focus of UT4 (Eisenhauer et al. 2003, Bonnet

et al. 2004). The observations were performed with 3 gratings (J, H, K) providing a spectral resolution around 2000, 3000, 4000 in the J, H and K band respectively, each wavelength band fitting fully on the 2048 pixels of the Hawaii 2RG (2k×2k) detector in the dispersion direction (Eisenhauer et al. 2003, Bonnet et al. 2004). We employed the spatial resolution of $0''.025$ per image slice, which corresponds to a field-of-view of $0''.8 \times 0''.8$. HD 100453A was used as a natural AO guide star.

A summary of the SINFONI observations of HD 100453B (RA 11:33:05.655 DEC -54:19:29.144 Equinox 2000) is provided in Table 2.4. No spectral dithering was employed.

Table 2.4

Summary of VLT SINFONI Observations of HD 100453B

Filter	Type	# of Offsets	# Exp. × Exp. Time (s)	Total Exp. Time (s)	Jitterbox Size
K-band	acquisition	1	1 × 0.83	0.83	n/a
K-band	science	5	24 × 2	240	$0''.3$
H-band	science	5	18 × 2	180	$0''.5$
J-band	science	10	12 × 5	600	$0''.5$

To perform the telluric correction, the spectrophotometric standard star HIP 057432 was observed immediately following the science observations employing an exposure time of 50, 40, and 30 seconds in the J, H, K bands, respectively. In each band, two offset positions were taken. At the end of the night, the spectrophotometric standard

star HIP 051940 was observed in the J, H, and K bands employing an exposure time of 50, 40 and 20 seconds respectively. In each band, two offset positions were taken.

The raw frames of the target and standard stars were reduced using the SINFONI pipeline. For a detailed description of the procedure see the SINFONI pipeline manual by Modigliani et al. (2007). From the final stacked wave calibrated datacubes of HD 100453B and the standard stars, the one-dimensional (1-D) spectra of HD 100453B were extracted. We employed the following procedure. Each datacube was stacked in the wavelength direction producing a single two-dimensional (2-D) frame. In each 2-D frame, the center and radius of the psf was determined, as well as the size of background region (i.e., as in conventional aperture photometry). In the case of HD 100453B, we selected a psf radius of 7 pixels and a background region size of 5 pixels for all the three bands. Then we sampled the FOV ($0''.8 \times 0''.8$) by a 2-D frame of 94×90 pixels in the J band, 100×96 pixels in the H band, and 84×80 pixels in the K band. In the case of the standard stars, we selected a psf radius of 15 pixels and a background region size of 10 pixels for all the three bands. For this case, the FOV ($0''.8 \times 0''.8$) is sampled by a 2-D frame of 64×64 pixels in all three bands.

Thereafter, in each plane of the three-dimensional (3-D) data cube (i.e., each wavelength 2-D frame), the average number of counts per pixel in the background region was determined and subtracted from each pixel in the psf region, and the total number of counts in the psf region was summed. In this way the number of counts (corrected for background emission) as a function of wavelength (i.e. for each plane of the 3-D data cube) is obtained. Following this procedure, the 1-D spectrum was determined for HD 100453B and the standard stars in each of the observed bands.

Finally, to correct for telluric absorption, the 1-D extracted science spectrum of HD 100453B was divided by the 1-D extracted spectrum of each standard star. Small offsets of a fraction of a pixel in the wavelength direction were applied to the standard star spectrum until the best signal-to-noise ratio, in the corrected science spectra, was obtained. Since we observed two standard stars, two sets of telluric corrected spectra were obtained for HD 100453B in each band. We selected the spectra that exhibited the best signal to noise ratio. The spectra were normalized by fitting a second-degree polynomial to the continuum (Figure 2.4).

2.2.2.2 FUSE Spectroscopy

HD 100453 was observed by FUSE for the Cycle 3 guest investigator program on 2003 June 10, using the large (30 arcsec) aperture in time-tag mode. The data set identification is C1260101 (PI Grady). The spectra were processed using CalFUSE 3.0.8, and stacked independently by channel segment using the corrcal routine written by S. Friedman. The total exposure was 11788 s, but only exposures that were useful or free of obvious defects (in the case of SiC2B) were included in the summed data. Exposure times by channel segment are listed in Table 2.5.

Table 2.5

Summary of FUSE Observations

Segment	LiF1A	LiF1B	LiF2A	LiF2B	SiC1A	SiC1B	SiC2A	SiC2B
Exp time (s)	8803	9866	7960	9308	7975	9458	7960	11328

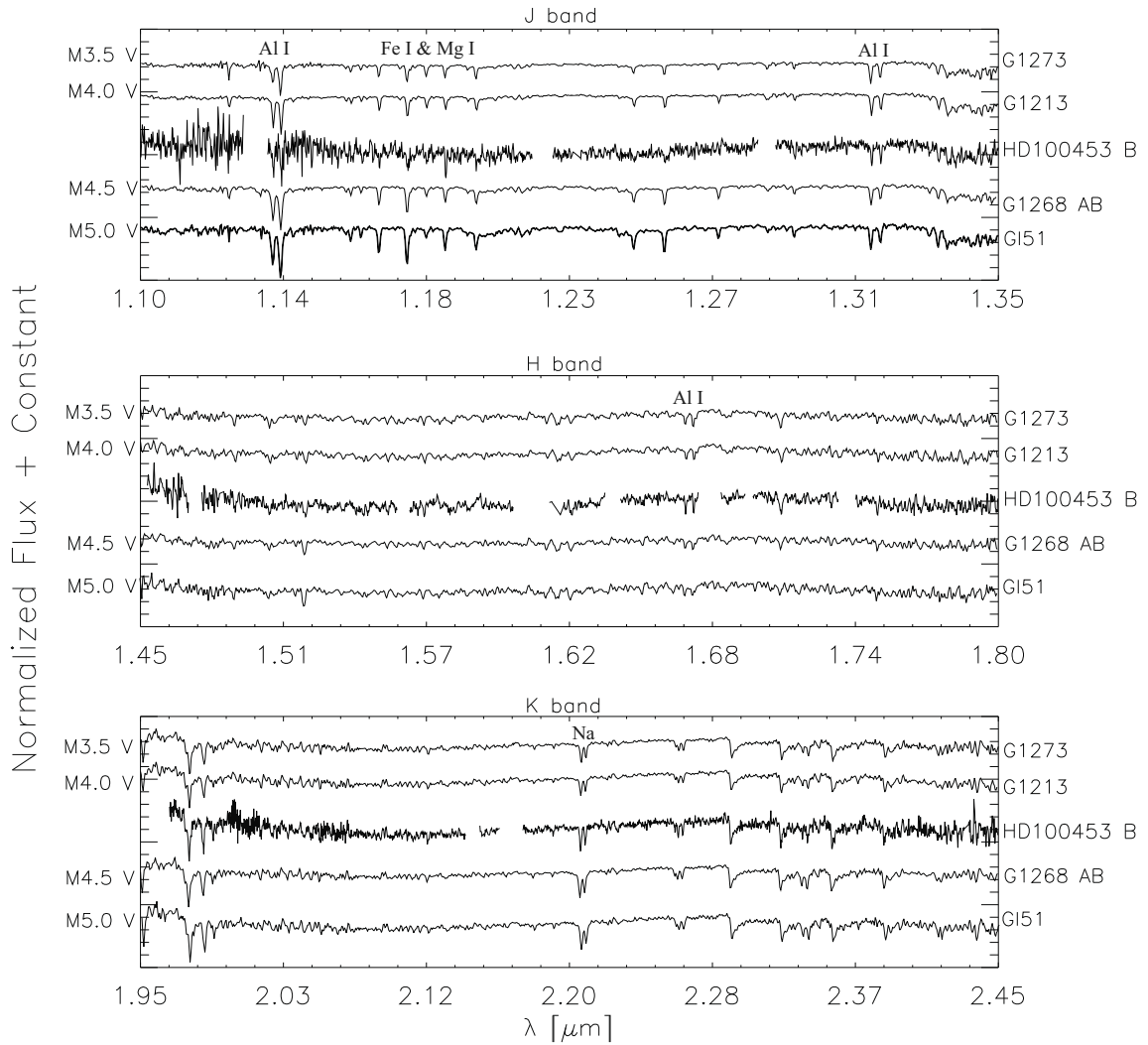


Figure 2.4. SINFONI spectra of HD 100453B in the J, H and K bands.

Regions of poor telluric correction (i.e., strong telluric absorption), and regions in which the spectra of the standard star have spectral features have been removed from the spectra. The spectra of four templates from the IRTF NIR library are over-plotted in each panel. The spectra are continuum-normalized by a second-degree polynomial. See § 2.3.1.1 for line identification.

Emission line profiles for C III $\lambda 977 \text{ \AA}$, O VI $\lambda 1032 \text{ \AA}$ and O VI $\lambda 1036 \text{ \AA}$, Fe II $\lambda 1144 \text{ \AA}$, and C III $\lambda 1176 \text{ \AA}$ were obtained (Figure 2.5). The C III $\lambda 977 \text{ \AA}$ emission profile has an absorption feature centered near 976.4 \AA which is likely O I $\lambda 976.4 \text{ \AA}$ absorption (Figure 2.5a). However, this can not be confirmed due to a lack of continuum in the range of other available O I lines. The sharp absorption feature near 977.2 \AA does not show up in SiC1B. This combined with the sharpness of the edges of the feature suggests that it is an artifact in the SiC2A data. The flux in the O VI $\lambda 1032 \text{ \AA}$ emission profile is $8.8 \times 10^{-14} \pm 3.2 \times 10^{-15} \text{ erg cm}^{-2} \text{ s}^{-1} \text{ \AA}^{-1}$ (Figure 2.5b). The O VI $\lambda 1038 \text{ \AA}$ profile is contaminated with C II $\lambda 1036.3 \text{ \AA}$ and C II $\lambda 1037.0 \text{ \AA}$. The combined flux in the C III $\lambda 1176 \text{ \AA}$ emission profile is $2.1 \times 10^{-13} \pm 3.7 \times 10^{-15} \text{ erg cm}^{-2} \text{ s}^{-1} \text{ \AA}^{-1}$. In a Gaussian decomposition using IRAF splot, we find evidence for two components with an equivalent width ratio of $\sim 0.7:1$ and FWHM ratio of $\sim 0.6:1$ (Figure 2.5c). The Fe II $\lambda 1144 \text{ \AA}$ emission profile was not detected (Figure 2.5d).

We calculate a mean flux of the continuum at $1140 - 1160 \text{ \AA}$ for LiF2B of $1.4 \times 10^{-15} \text{ ergs s}^{-1} \text{ cm}^{-2} \text{ \AA}^{-1}$ with a standard deviation in the mean of $2.3 \times 10^{-16} \text{ ergs s}^{-1} \text{ cm}^{-2} \text{ \AA}^{-1}$. However, the fluxes are clipped at less than $-6 \times 10^{-15} \text{ ergs s}^{-1} \text{ cm}^{-2} \text{ \AA}^{-1}$, so the data are skewed and we are not able to accurately adjust the mean and standard deviation values. Instead we find a 1σ upper limit to the FUV continuum of $1.5 \times 10^{-15} \text{ ergs s}^{-1} \text{ cm}^{-2} \text{ \AA}^{-1}$.

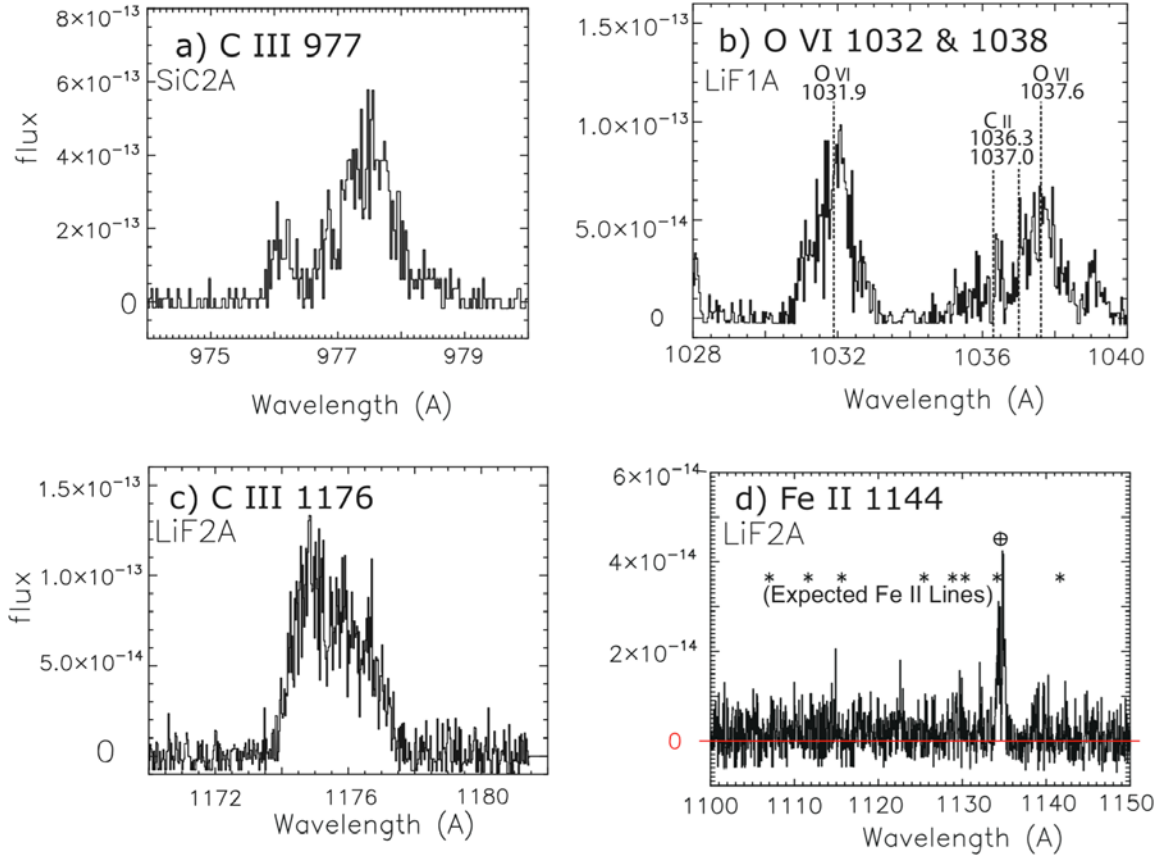


Figure 2.5. FUSE spectra of HD 100453.

All flux is in units of $\text{erg cm}^{-2} \text{s}^{-1} \text{\AA}^{-1}$. a) The C III $\lambda 977 \text{ \AA}$ profile. The detection of C III $\lambda 977 \text{ \AA}$ at 114 pc suggests low extinction toward HD 100453. b) The O VI $\lambda 1031.9 \text{ \AA}$ and O VI $\lambda 1037.6 \text{ \AA}$ profiles. The O VI $\lambda 1038 \text{ \AA}$ profile is contaminated with C II $\lambda 1036.3 \text{ \AA}$ and C II $\lambda 1037.0 \text{ \AA}$. c) The C III $\lambda 1176 \text{ \AA}$ profile. In a Gaussian decomposition using IRAF *splot*, we find evidence for two components with an equivalent width ratio of $\sim 0.7:1$ and FWHM ratio of $\sim 0.6:1$. d) The Fe II $\lambda 1144 \text{ \AA}$ profile. We find no evidence of Fe II emission, suggesting no gas in the inner 1 AU (see text).

2.2.2.3 Gemini South Phoenix Echelle Spectroscopy

The CO observations were taken with the Phoenix echelle spectrograph on Gemini South Observatory on 2007 February 6 with an exposure time of 480 seconds. Phoenix is a high-resolution $\lambda/\Delta\lambda = 50,000$ (4 pixel slit - $0''.34$), near-infrared 1 – 5 μm spectrometer. An individual spectrum is single order and covers a very narrow wavelength range of 0.5% of the central wavelength, corresponding to a radial velocity range of 1500 km/sec (Hinkle et al. 1998; Hinkle et al. 2000; Hinkle et al. 2003). We observed HD 100453 with one M-band setting centered at 4.97 μm . The data were reduced and calibrated using standard reduction techniques, which are described in DiSanti et al. (2001), Brittain et al. (2003), and Brittain (2004). The spectrum was divided by the spectrum of a standard star, HR 5671, to correct for the telluric absorption. The gaps in the spectrum are of areas with less than 50% transmittance (Figure 2.6). The CO emission lines P30 and P31 were not detected above noise (see § 2.3.5.3 for details).

2.2.2.4 JCMT HARP Spectroscopy

We searched for the 345GHz (868 μm) ^{12}CO J = 3–2 line using the Heterodyne Array Receiver Program (HARP) (Dent et al. 2000) at the James Clerk Maxwell Telescope (JCMT) at Mauna Kea, Hawaii, on 2008 February 22 and 24. The weather was stable and dry with a precipitable water vapor level less than 2 mm. The observations were carried out in beam-switching mode with a chop of $120''$. The total on-source integration time was 20 minutes. Calibration was checked via similar observations of IRC+10216 and is estimated to be accurate within 5%. The rms radiation temperature in binned 10 km s⁻¹ channels was 0.0077 K, and the ^{12}CO J = 3–2 emission line was not detected above noise.

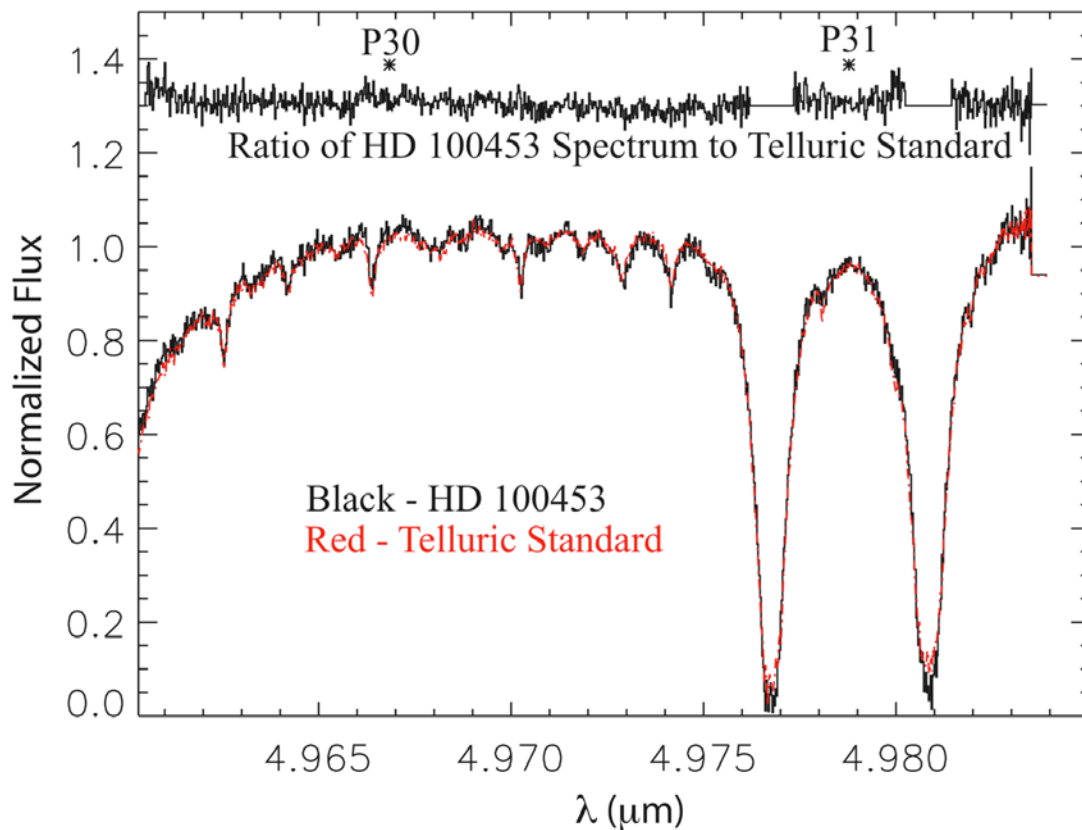


Figure 2.6. Phoenix echelle M-band spectra of HD 100453.

The exposure time is 480 seconds. The upper black line is the HD 100453 spectrum divided by with the HR 5671 (standard star) spectrum to correct for telluric absorption. The gaps in the spectrum are of areas with less than 50% transmittance. The asterisk labeled P30 marks the rest position of the CO $v = 1-0$ P30 rotation-vibration transition line. The asterisk labeled P31 marks the rest position of the CO P31 rotation-vibration transition line. The CO emission lines P30 and P31 were not detected above noise in our observations. The lower black curve traces the HD 100453 spectrum. The lower red curve traces the telluric standard HR 5671 spectrum.

2.2.2.5 ESO 1.52 m FEROS Echelle Spectroscopy

Meeus et al. (2002) observed HD 100453 in February 1999 with the echelle spectrograph FEROS (Kaufer et al. 1999) on the ESO 1.52 m telescope at La Silla (ESO ID 62.L-0508). FEROS has a spectral resolution of $R = 48,000$. The spectrum obtained covered the wavelength range 3700 – 9220 Å. The detailed spectra around Ca II $\lambda 8662.17$ Å were not previously published and are included in this work.

The spectra were reduced in ESO-MIDAS with pipeline reduction software ("context FEROS", e.g. Kaufer et al. 2000). The standard echelle reduction steps include bias subtraction, flat fielding, correction for scattered light and order overlaps, wavelength calibration, and optimal extraction of the spectra. The spectra were normalized by fitting a pseudo-continuum through line-free regions, and then dividing the spectra by this continuum. The spectra show Ca II $\lambda 8662.17$ Å in absorption with no detectable emission component (Figure 2.7).

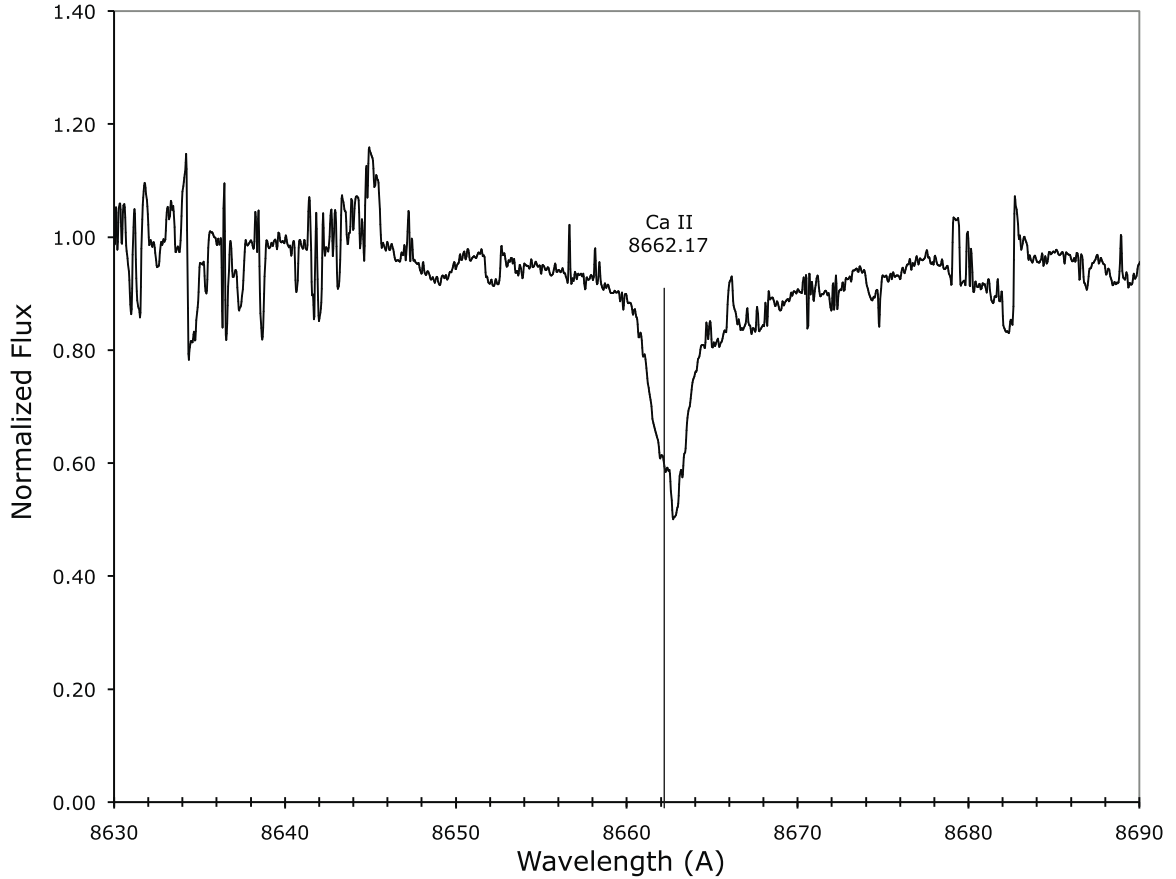


Figure 2.7. Spectra of HD 100453A near the Ca II infrared triplet line $\lambda 8662.17 \text{ \AA}$.

The Ca II $\lambda 8662 \text{ \AA}$ line is in absorption, with no emission component. We estimate an emission upper limit on EW for Ca II $\lambda 8662 \text{ \AA}$ of $5 \times 10^{-3} \text{ \AA}$.

2.2.2.6 IUE Archival Data

We utilize archival IUE datasets SWP53936 and SWP53937 with exposure times of 360 s and 720 s, respectively. The low dispersion, large aperture data were obtained in February 1995 as part of Program ID RM050 (Waelkens, C. – PI). The data indicate Lyman α in emission.

2.3. Results

2.3.1 A T-Tauri Star near HD 100453A

The identification of a companion candidate for HD 100453A is reported in Chen et al. (2006) from VLT NACO NIR photometry. The separation between the candidate companion and HD 100453A is $1''.06$, with a brightness contrast of 5.1 mag at K_s and 4.2 mag at B_{r} . Utilizing a PMS H–R diagram, they found that the photometric data and assumed age range of 10 – 20 Myr are consistent with a $0.3 M_{\odot}$ companion to HD 100453A, corresponding to a spectral type of M3 – M5.

Analysis of both the direct (Figure 2.8) and coronagraphic (Figure 2.9) HST ACS F606W images of HD 100453A reveals clear evidence of a possible companion located at $1''.045 \pm 0''.025$ from the central star at a position angle of $126 \pm 1^{\circ}$ measured E of N. We extracted crude photometry for the secondary from both images, using a small $0''.1$ aperture and aperture corrections estimated via SYNPHOT. The resultant photometry from the direct ($m_{\text{F606W}} = 15.6$) and coronagraphic ($m_{\text{F606W}} = 15.8$) images is consistent, as summarized in Table 2.6. The dominant source of uncertainty in these values is clearly related to the relative amount of contamination contributed by the saturated central source in the direct imaging data and the contamination from significant psf-subtraction residuals in the coronagraphic imaging. Given the range of derived photometry, we suggest an approximate m_{F606W} magnitude for the secondary of 15.7 ± 0.2 . We found that the aperture adjustments suggested by Bohlin (2007) to compensate for a shift in λ_{eff} for the F606W filter due to an M-type star are negligible (less than 0.03 magnitudes).

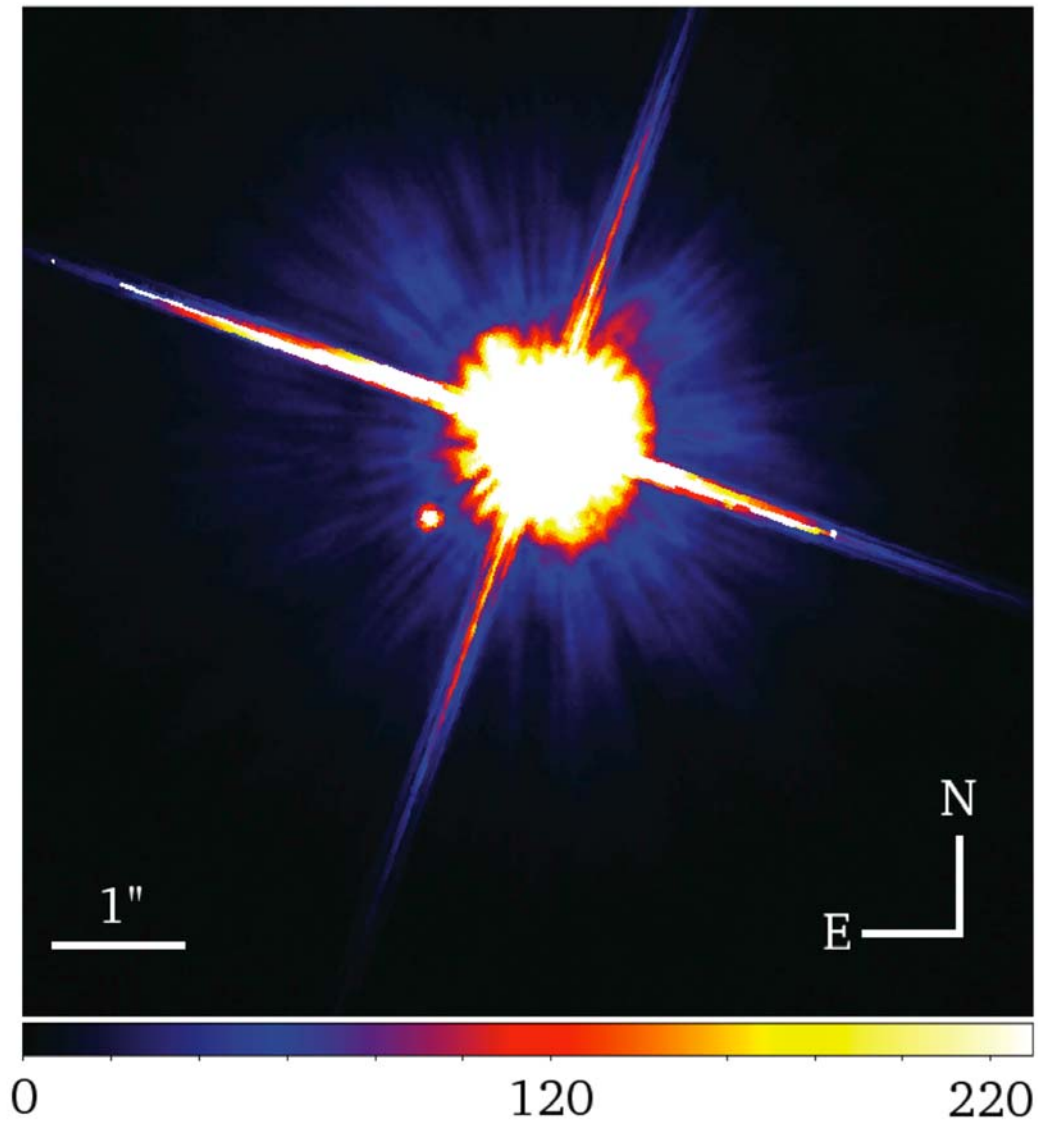


Figure 2.8. HST F606W direct image of the HD 100453 system.

A $7''.5 \times 7''.5$ direct F606W image of HD 100453A taken with the HST/ACS/HRC camera. While the central HD 100453A source is clearly saturated, a distinct second source is clearly visible $\sim 1''.05$ southeast from HD 100453A, at a position angle of 126° .

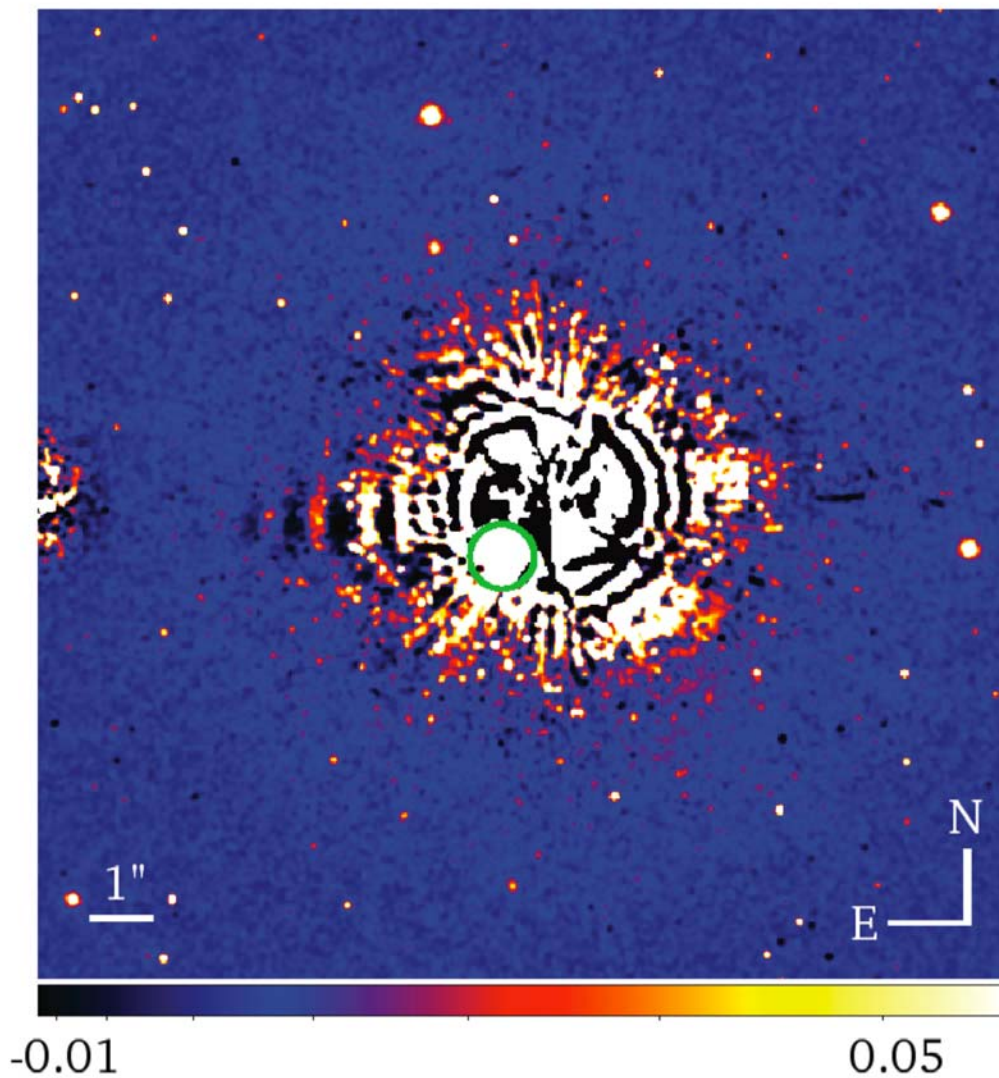


Figure 2.9. HST F606W coronagraphic image of the HD 100453 system.

A $15''.0 \times 15''.0$ psf-subtracted coronagraphic image of HD 100453 in the F606W filter, plotted on a linear scale and smoothed using a 3×3 Gaussian kernel. No evidence of an extended scattered light disk is seen at a level of $\sim 21.2 \text{ mag arcsec}^{-2}$. The secondary companion, identified within the green circle, is clearly visible through the psf-subtraction residuals and consistent with the companion identified in direct imaging.

Analysis of the HST/ACS/SBC/F122M psf-subtracted image reveals that the candidate companion is not detected in the FUV (Figure 2.10). The mean background level around the expected location of the secondary object is 1.1×10^{-3} counts sec^{-1} with a standard deviation of 1.3×10^{-3} counts sec^{-1} . We find no source detections above a 5σ limit outside a $0''.2$ radius from HD 100453A. The number of counts per second above mean background within a 5×5 pixel region at the candidate companion's expected location is 0.031 counts sec^{-1} . To find the corresponding point source flux, we utilized the HST exposure time calculator (ETC) for the SBC with filter F122M, a Lyman α emission line point source of width 5 \AA , and no continuum. We find the corresponding upper limit on Lyman α flux of the candidate companion to be 2.55×10^{-15} erg $\text{cm}^{-2} \text{ s}^{-1}$.

To get a better understanding of how other young M-type stars would compare in Lyman α to the M-type candidate companion of HD 100453A, we investigated AT Mic. AT Mic has a spectral type of M4.5Ve, a distance of 10 pc, an age of 12 Myr, and is a member of the β Pictoris Moving Group. We reviewed all 17 of its IUE SWP low dispersion, large aperture datasets and derived an integrated Lyman α flux for AT Mic of $\sim 5 \times 10^{-12}$ erg $\text{cm}^{-2} \text{ s}^{-1}$. Scaling the AT Mic flux from 10 pc to 114 pc results in an equivalent flux of $\sim 4 \times 10^{-14}$ erg $\text{cm}^{-2} \text{ s}^{-1}$. Comparing with the HD 100453B Lyman α flux upper limit of 2.55×10^{-15} erg $\text{cm}^{-2} \text{ s}^{-1}$, the data indicate that HD 100453B is either later in spectral type and/or less active than an M4.5Ve at 12 Myr.

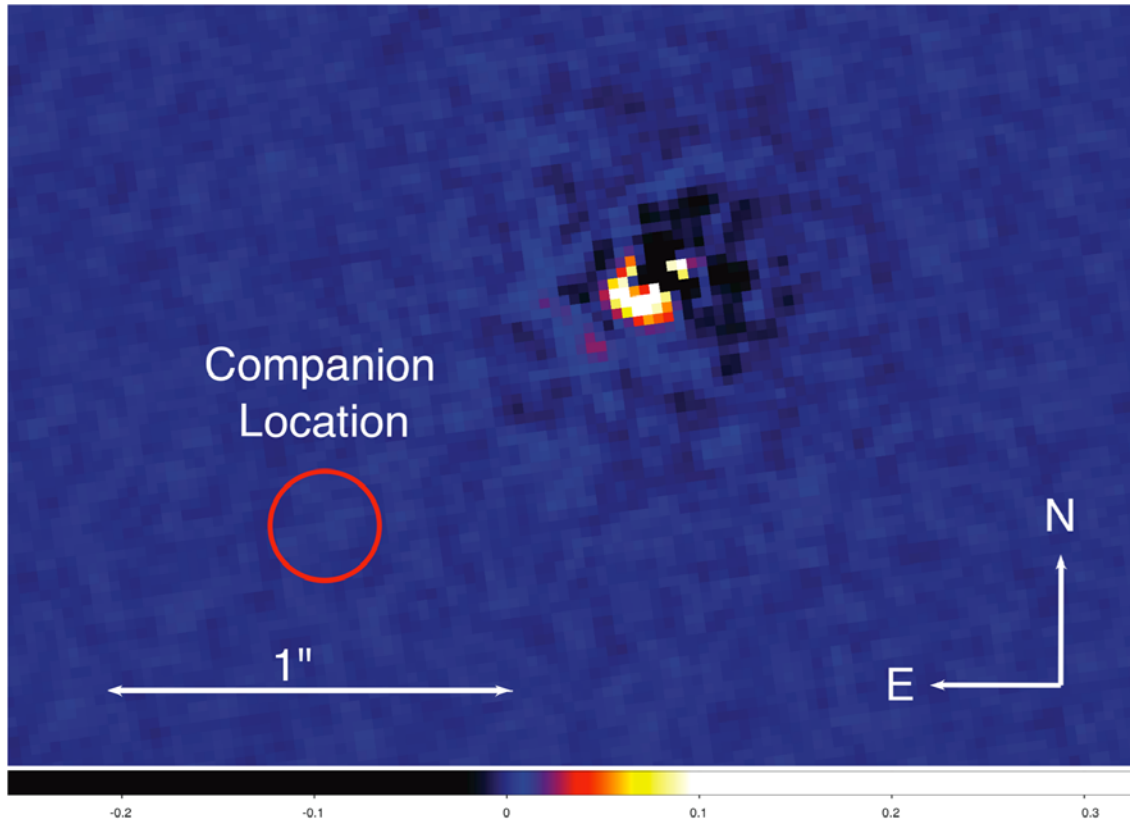


Figure 2.10. HST F122M FUV psf-subtracted image of the HD 100453 system.

A $2''.8 \times 1''.9$ HST/ACS/SBC psf-subtracted image of HD 100453 in the F122M filter (non-coronagraphic), plotted on a linear scale. No significant residuals exist outside a radius of $0''.2$ from the star's peak. The red circle identifies the expected location of the companion.

2.3.1.1 Spectral Type Determination

The spectral type of HD 100543B was established by comparison of our SINFONI spectra with the IRTF NIR spectral library²⁰ (Rayner et al. in prep). In Figure 2.4 we present the continuum normalized J, H, and K spectra of HD 100453B and the

²⁰ <http://irtfweb.ifa.hawaii.edu/spex/spexlibrary/IRTFlibrary.html>

continuum normalized spectral templates of M3.5V to M5.0V stars from the IRTF NIR spectral library. We generally use strong neutral species absorption (e.g. Na, Fe, Mg, K, Al) and CO for the spectral classification.

We first consider the J band spectrum. We observe two absorption features at 1.14 μm and 1.32 μm (Al I). The strength of these features are consistent with spectral types ranging from M3.5V to M5.0V (note that the left peak of the 1.14 μm line is too strong to be consistent with M3.5V, however, given the S/N of the spectra at this wavelength it is difficult to rule out the M3.5V spectral type). Now, we observe that between 1.16 μm and 1.20 μm (includes Fe I, Mg I lines), and between 1.25 μm and 1.27 μm , the absorption features observed in HD 100453B are much weaker than in the spectral type M5.0V. This indicates that HD 100453B should be earlier than M5.0V.

Next we consider the H band spectrum. We observe a double peaked Al I absorption line at 1.67 μm . This feature is present in the M3.5V spectra and M4.0V spectra, but is barely seen in the M4.5V spectra and is not observed in the M5.0V spectra (again suggesting that M5.0V is not consistent with the HD 100453B spectra). Furthermore, the strength of the absorption feature near 1.52 μm is consistent with spectral types M3.5V to M4.5V.

Finally let us consider the K band spectrum. We observe the triplet at 1.97 μm and the Na doublet at 2.20 μm . The depths of these lines are more consistent with the depths of the M4.5V and M5.0V lines than the depths of the M3.5V or M4.0V lines. Given this ensemble of characteristics, we conclude that the best match to the HD 100453B J, H, and K band spectra is the spectral type of M4.0V to M4.5V. The source does not exhibit Br γ in emission, suggesting that HD 100453B is not accreting.

For a consistency check, we estimated the likely spectral type of HD 100453B from the F606W photometry by using SYNPHOT (Laidler et al. 2007) to calculate the expected m_{F606W} fluxes for a range of stellar sources renormalized to the known distance of 114 pc for HD 100453 (Perryman et al. 1997). The observed candidate companion flux is consistent with that expected from a main sequence M2.5V-type star (± 1 sub-types), but given the PMS nature of the companion, the magnitude will be about 1.5 – 2 magnitudes fainter before reaching the main sequence (Siess et al. 2000). Cox et al. (2001) show that a dimming of about 1.5 – 2 magnitudes from a spectral type M2.5V-type star is a spectral type M4.0V-type star. Therefore, the F606W photometry suggests a spectral type of M4.0V (± 1 sub-types) for HD 100453B, in good agreement with the SINFONI derived spectral type range.

2.3.1.2 Photometry

Photometric analysis of our VLT NACO L'-band and M'-band coronagraphic imagery for HD 100453B reveals that, including a reduction of 0.234 magnitudes to account for the pupil stop used during the science observations, $L' = 10.13 \pm 0.1$ magnitudes and $M' = 9.99 \pm 0.1$ magnitudes. Bessell and Brett (1988) indicate that $L = L' + 0.14$ for a spectral type M4.0V star. Then for HD 100453B, we have $L = 10.27 \pm 0.1$. Chen et al. (2006) determined $K_s = 10.66 \pm 0.1$ for HD 100453B. Persson et al. (1998) provide measurements of both K and K_s for several stars of similar spectral type. The result is that for M-type stars, $K \cong K_s - 0.02$ magnitudes, so we adopt $K = 10.64 \pm 0.1$ for HD 100453B. Following Sirianni et al. (2005), we convert our m_{F606W} magnitude of 15.7 ± 0.2 to V-band magnitude using $B - V = 1.6$ (Kenyon and Hartmann 1995). The result is $V = 15.87 \pm 0.2$. Comparison of the V-K and V-L colors

of HD 100453B to those of an unreddened M4V star compiled by Kenyon & Hartmann (1995), indicates $E(V - K) = -0.03 \pm -0.20$ and $E(V - L) = 0.11 \pm -0.20$. These colors indicate that HD 100453B has no IR excess in the K-band or L-band. See Table 2.6 for a summary of the photometry.

To determine $\log L_x/L_{\text{bol}}$ for the candidate companion, we utilize the V-band magnitude of 15.87 and the bolometric correction for an M4.0 star of -2.56 (Kenyon & Hartmann 1995) to arrive at a value of $L_{\text{bol}} = 1.86 \times 10^{32} \text{ erg s}^{-1}$, assuming a distance of 114 pc. From our Chandra data for the candidate companion (Table 2.1), we have $L_x = 5.7 \times 10^{28} \text{ erg s}^{-1}$ in the range 0.3 – 2.0 keV. The result is $\log L_x/L_{\text{bol}} = -3.51$, which indicates the candidate companion is a T Tauri star (Feigelson et al. 2003).

Table 2.6Summary of Photometry

Object	Mode	Filter	magnitude	Notes
HD 100453B	Direct	m _{F606W}	15.6	(used in line 3)
HD 100453B	Coron	m _{F606W}	15.8	(used in line 3)
HD 100453B	Combined	m _{F606W}	15.7 ± 0.2	M4.0V (± 1 sub-types)
HD 100453B	Direct	K _s	10.66 ± 0.1	Chen et al. (2006)
HD 100453B	Coron	L'	10.13 ± 0.1	- - -
HD 100453B	Coron	M'	9.99 ± 0.1	- - -
HD 100453B	Calculated	V	15.87 ± 0.2	(see text)
HD 100453B	Calculated	K	10.64 ± 0.1	(see text)
HD 100453B	Calculated	L	10.27 ± 0.1	(see text)
HD 100453A	Direct	V	7.78	Vieira et al. (2003)
HD 100453A Disk	Coron	m _{F606W}	>21.8-21.9 (mag arcsec ⁻²)	1σ limit
HD 100453A Disk	Coron	m _{F606W}	>21.1-21.2 (mag arcsec ⁻²)	2σ limit

Note: — HST and VLT derived photometry for the HD 100453 system. The V, K, and L magnitudes are derived from the m_{F606W}, K_s, and L' magnitudes, respectively (see text). The HD 100453A disk values correspond to the 1σ and 2σ limiting surface magnitudes of the scattered light disk.

2.3.1.3 Relative Proper Motion

Based on the proper motion (PM) as measured by Hipparcos (Perryman et al. 1997), the HD 100453 system PM is $\mu_\alpha = -36.95 \pm 0.78$ mas yr⁻¹ (west) and $\mu_\delta = -4.72 \pm 0.53$ mas yr⁻¹ (south). Over a period of three years, the system has moved 110.85 ± 2.34 mas west and 14.16 ± 1.59 mas south or 111.75 ± 2.83 mas in the direction 262.72 ± 0.96 degrees E of N.

Now we consider star B, which is the 1".05 candidate companion referred to as HD 100453B in Chen et al. (2006). The relative positions of the primary star and star B in the 2003 and 2006 VLT NACO imagery were determined by fitting 2D Gaussians to the Br γ narrow band images at the approximate positions of each star. For each epoch of data, no saturation exists and no residuals can be seen above the noise level for either the primary or star B. The separation and position angle (PA) found for the 2003 epoch data are $1".054 \pm 0".007$ and 127.19 ± 0.30 degrees E of N, respectively. The separation and PA found for the 2006 epoch data are $1".047 \pm 0".005$ and 128.22 ± 0.28 degrees E of N, respectively. Comparing the positions for these two epochs, we find a relative motion of 20.11 ± 10.75 mas at 238.40 ± 28 degrees E of N or 18.33 ± 9.80 mas in the direction of system PM. We find that the relative motion of star B with respect to the primary star is $16 \pm 9\%$ of the system PM. Thus, we show that HD 100453A and HD 100453B have common proper motion.

Given our SINFONI determination of the spectral type of M4.0V to M4.5V, we confirm that HD 100453B is stellar in nature, has a cool atmosphere, and is not in the red giant or red supergiant phase (i.e. is not a high luminosity class background star). This result, combined with our result that HD 100453A and HD 100453B are comoving,

supports the binary hypothesis. We therefore firmly conclude that HD 100453B is a companion to HD 100453A.

2.3.2 A Third Object in the Field

In the HST/ACS/HRC/F606W direct image (observed November 2003), we detect a faint object at approximately $0''.8$ from HD 100453A at a position angle of approximately 30° east of north. For clarity, we refer to this object as star C in this work. We also obtained archival VLT NACO J-band coronagraphic imagery (observed June 2006), and we detect a faint object near the same location. Based on crude photometry, the object is very roughly 3 magnitudes fainter than HD 100453B in both the F606W filter and in the J-band filter. If we assume star C is at the same distance as the HD 100453 system, then the spectral type would be very roughly M7 – M8, based on the spectral type of HD 100453B.

We now examine the relative proper motion of star C compared to the proper motion of the primary star. The location of the primary star has been determined in each image by finding the intersection of the diffraction spikes. Although we use this method, it is important to note that the optical axis of NACO does not coincide with the optical axis of the Nasmyth focus. This means that while the de-rotator corrects for the adapter rotation, the spike will move in a non-symmetric pattern, leading to possible inaccuracies in defining the location of the star under the coronagraph (D. Dobrzycka, private communication). In the ACS image, the position of HD 100453B is assumed to be at the peak brightness of the object. In the NACO adaptive optics image, HD 100453B is saturated, creating a doughnut shaped object with no peak pixel near the centroid. For this reason, we assume the geometric centroid of the object to be the position of

HD 100453B. For both epochs, the position of star C was assumed to be at the peak brightness of the faint object. Figure 2.11 is an overlay of the NACO image onto the ACS image with both images oriented such that north is up and east is to the left. The position of the NACO image has been shifted so that the location of the primary star coincides with the location of the primary star in the ACS image. The elapsed time between the ACS and NACO images is about 2.5 years. Accounting for the relative motion of HD 100453B determined from the Br γ imagery, the 2006 NACO image has been stretched to place HD 100453B in the appropriate position relative to the 2003 ACS position. For clarity, the centers of the ACS and NACO diffraction spikes and object locations have been marked in red and blue, respectively. The relative motion of star C has a magnitude that is consistent with, and a direction opposite to, the proper motion of HD 100453A. With this crude methodology, we find that the net proper motion of star C is approximately zero, suggesting that it is likely a background star.

2.3.3 The Age of the System

Age estimates have proven problematic for Herbig Ae stars due to the rapid evolution of the star to the Zero-Age Main Sequence. However, the identification of comoving low-mass stars which are associated with A stars (e.g. Zuckerman & Song 2004) permits independent dating of the A star.

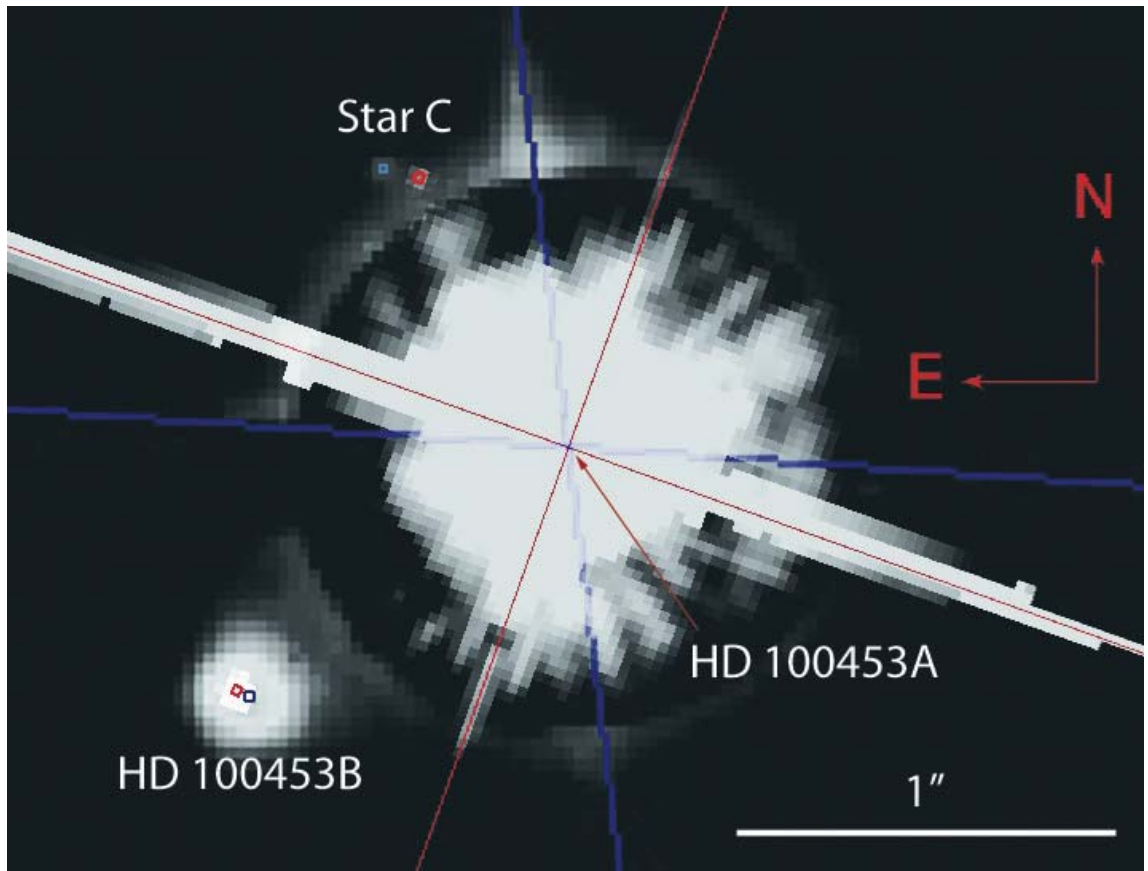


Figure 2.11. Relative proper motion for star C.

The image shows an overlay of the June 2006 NACO image onto the November 2003 ACS image with both images oriented such that north is up and east is to the left. For clarity, the center of the ACS and NACO diffraction spikes and object locations have been marked in red and blue, respectively. The *relative* motion of star C has a magnitude that is consistent with, and a direction opposite to, the *proper* motion of HD 100453A. We find that the net proper motion of star C is approximately zero, suggesting that it is likely a background star.

2.3.3.1 Companion Star H-R Diagram

Recalling that the companion to HD 100453A has spectral type M4.0V – M4.5V, $K = 10.64 \pm 0.1$ magnitudes, and a distance of 114^{+11}_{-9} pc, we use the Siess et al. (2000) PMS stellar model online “WWW tools”²¹ (hereafter referred to as the Siess tools) along with the Kenyon and Hartmann (1995) conversion tables to determine the bounds on the age of the companion and thus HD 100453A. We use the data in Kenyon and Hartmann (1995) to convert the measured spectral type range of M4.0V – M4.5V to an effective temperature range. The results are $T_{\text{eff}} = 3300 \text{ K} - 3400 \text{ K}$. We use the Siess tools to create a PMS Hertzsprung-Russell (H-R) diagram containing isochrones and mass tracks with m_K as a function of $\log T_{\text{eff}}$ (Figure 2.12).

The error bars in m_K are dominated by the uncertainty in the K-band photometry and the uncertainty in distance to the system. The error bars in $\log T_{\text{eff}}$ are dominated by the uncertainty in the determination of the spectral type. We find that the mass of HD 100453B is $0.21 - 0.23 M_{\odot}$ and that the age range for HD 100453B and the entire system, is $10 - 15 \text{ Myr}$. We also plotted HD 100453B on the tracks of Baraffe et al. (1998). We find that the mass of HD 100453B is $0.24 - 0.30 M_{\odot}$ and that the age range for the HD 100453 system is $11 - 18 \text{ Myr}$.

The age estimate of the system based on both the Siess et al. (2000) and the Baraffe et al. (1998) models is in agreement with the Kouwenhoven et al. (2005) result that HD 100453A is a member of the Lower Centaurus Crux Association, which places an upper limit for the age at about 20 Myr (Mamajek et al. 2002). We conclude that the

²¹ <http://www-astro.ulb.ac.be/~siess/prog.html>

age of the HD 100453 system is 14 ± 4 Myr and that the mass of HD 100453B is $0.21 - 0.30 M_{\odot}$.

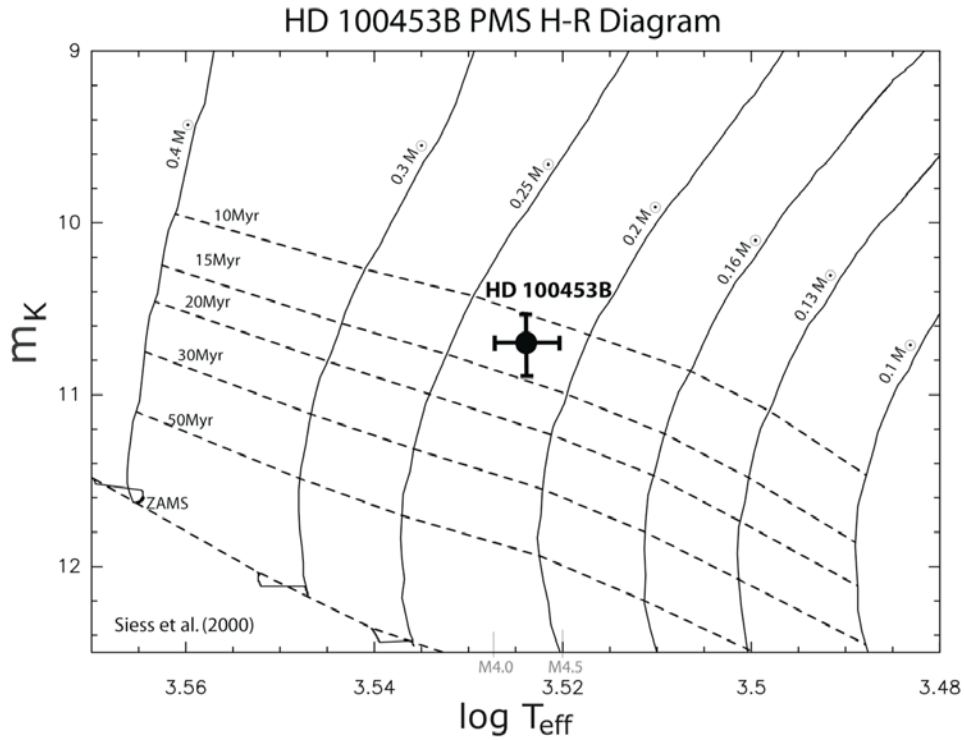


Figure 2.12. Hertzsprung-Russell diagram for HD 100453B.

The solid cross locates HD 100453B in the diagram and demonstrates the relation to the mass tracks and isochrones. The error bars in m_K are dominated by the uncertainty in the K-band photometry and the uncertainty in distance to the system. The error bars in $\log T_{\text{eff}}$ are dominated by the uncertainty in the determination of the spectral type. Based on the Siess et al. (2000) models, we find the age of the system to be in the range 10 – 15 Myr and that the mass of HD 100453B is in the range $0.21 - 0.23 M_{\odot}$.

2.3.3.2 Primary Star H-R Diagram

To validate our age result, we examine the H–R diagram of HD 100453A. We utilize V-band photometry to avoid contamination problems induced by the IR excess

contributed by the circumstellar disk, and we correct the photometry for reddening along the HD100453A sight line. Using 51 Eri (F0V) as a reference ($B - V = 0.28$, Johnson et al. 1966) and a grid of colors from Cox et al. (2001), we calculate $B - V = 0.27$ for an A9V star. Based on the observed magnitudes in Table 1.2, the color excess for HD 100453A is $E(B - V) = 0.02$. Assuming $R = 3.1$, then $A_v = 0.06$ and $V_{\text{intrinsic}} = 7.72$. Inspection of the spatially resolved large aperture spectral image for IUE SWP53937 reveals circumstellar Lyman α emission above the geocoronal background. Detection of such emission indicates $E(B - V) \leq 0.08$ for selective extinction by the diffuse ISM (Roberge et al. 2001). Additional evidence of low reddening for HD 100453A has been extracted from our FUSE data. The detection of C III $\lambda 977 \text{ \AA}$ emission (Figure 2.5a) from a star at 114 pc, suggests low extinction toward HD 100453 (Sasseen et al. 2002).

We use the Siess tools to create a PMS H–R diagram containing isochrones and mass tracks with m_v as a function of $\log T_{\text{eff}}$ (Figure 2.13). The error bars in m_v are dominated by the uncertainty in the distance to the system. The error bars in $\log T_{\text{eff}}$ are dominated by the uncertainty in the determination of the spectral type. We assign an uncertainty of ± 0.5 sub-types and use the conversion data in Kenyon and Hartmann (1995) to determine an effective temperature range of $T_{\text{eff}} = 7300 \text{ K} - 7500 \text{ K}$. We find that the mass of HD 100453A falls within the range $1.6 M_{\odot}$ to $1.8 M_{\odot}$, consistent with the published value of $1.7 M_{\odot}$. ZAMS arrival is at $\sim 40 \text{ Myr}$ for this mass range. The corresponding age is from 10 Myr to the ZAMS, consistent with the result above that the age of the system is $14 \pm 4 \text{ Myr}$. Dating the system through a low mass companion has significantly refined the age of the A star from 10 Myr – ZAMS to $14 \pm 4 \text{ Myr}$. The

Baraffe et al. (1998) tracks cannot be compared for the A star because the models only provide data for mass tracks up to $1.4 M_{\odot}$.

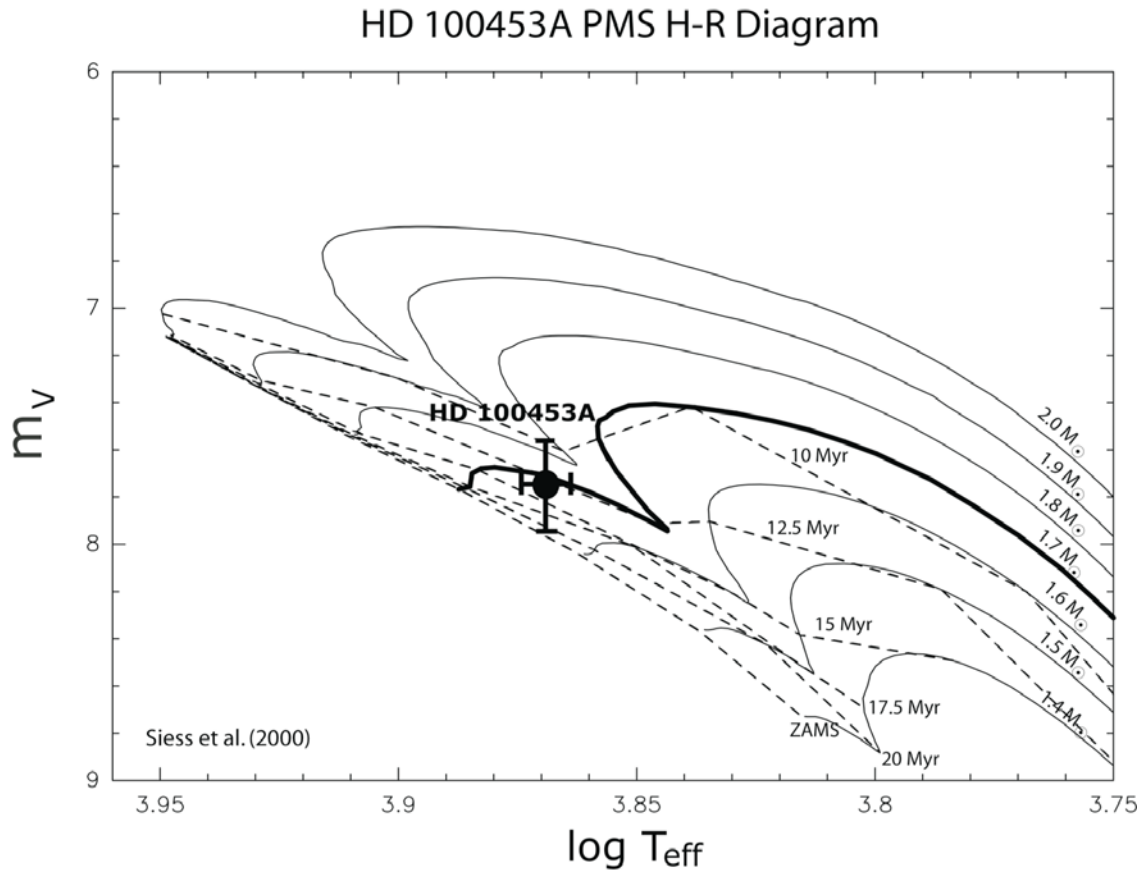


Figure 2.13. Hertzsprung-Russell diagram for HD 100453A.

The solid cross locates HD 100453A in the diagram and demonstrates the relation to the mass tracks and isochrones. The error bars in m_V are dominated by the uncertainty in the distance to the system. The error bars in $\log T_{\text{eff}}$ are dominated by the uncertainty in the determination of the spectral type. We find that the age of HD 100453A is from 10 Myr – ZAMS. We find that the mass of HD 100453A falls within the range $1.6 - 1.8 M_{\odot}$.

2.3.4 Accretion and Mass Loss of the Primary

Accretion onto PMS stars produces not only enhanced emission in transitions otherwise associated with chromospheres and transition regions, but also an enhanced UV continuum flux which can be detected against the light of a late A star shortward of 2000 Å, plus jets and/or Herbig-Haro knots, which can be imaged in Lyman α (Calvet et al. 2004; Grady et al. 2004). These emission characteristics are seen both for Meeus group I objects like AB Aur (Endres et al. 2005), and for Meeus group II disks like HD 163296 (Devine et al. 2000), HD 104237 (Grady et al. 2004), and MWC 480 (Stecklum et al. 2007).

2.3.4.1 H α Emission

Garcia Lopez et al. (2006) measured weak Br γ emission, suggesting that the star is accreting at a rate below $10^{-8} M_{\odot} \text{ yr}^{-1}$. Manoj et al. (2006) surveyed H α profiles for 91 Herbig B-, A-, and F-type stars, and found H α in emission for HD 100453A with an equivalent width (EW) of -0.8 \AA . Acke et al. (2005) measured the H α profile in absorption, with an EW = 1.5. These two EW measurements combined, indicate a weak, variable H α profile. Of the 91 Herbig stars in Manoj et al. (2006), HD 100453 has the weakest H α emission line. Of the 49 Herbig stars in Acke et al. (2005), HD 100453A has the only H α profile in absorption. All other stars in the survey show H α in emission and most have EWs in the range 10 – 100 Å. With H α emission being an indicator of accretion activity, HD 100453A is at best a very weak accretor.

2.3.4.2 FUV Limits

We present a collection of data (Grady et al. 2006) for several Herbig Ae/Be stars suggesting a power law relationship between accretion rate and FUV continuum flux (Figure 2.14). Garcia Lopez et al. (2006) (GL06) determined accretion rates for these stars based on net Br γ emission. The GL06 accretion rates are plotted in red against FUSE FUV continuum flux. Note the linear relationship between log FUV continuum flux and log accretion rate for all stars except HD 100453A (GL06). From our FUSE spectra, we extracted the log FUV continuum upper limit of -14.8 for HD 100453A and plotted it (in blue) on the line to estimate an accretion rate based on FUV continuum. The HD 100453A corresponding upper limit of -9.6 for log accretion rate was then determined from the graph and corresponds to an upper limit on accretion rate of $2.5 \times 10^{-10} M_{\odot} \text{ yr}^{-1}$. GL06 suggested that HD 100453A has an accretion rate of $9.12 \times 10^{-9} M_{\odot} \text{ yr}^{-1}$ based on net Br γ emission. Br γ emission can be due to accretion and to stellar activity and could also be due to the companion. However, Chen et al. (2006) imaged HD 100453 in Br γ and resolved the companion with a measured contrast ratio of 4.2 magnitudes. Thus only 2% of the Br γ flux is contributed by the secondary, which is insignificant. If Br γ emission is solely due to accretion, one would expect a high level of FUV continuum. We see a very low level of FUV continuum and therefore infer that the Br γ emission has a substantial activity component causing the GL06 accretion rate upper limit to be excessively high. It is also likely that other hydrogen lines exhibit evidence of activity as well, and that a non-trivial component of the weak H α profile originates from activity rather than accretion.

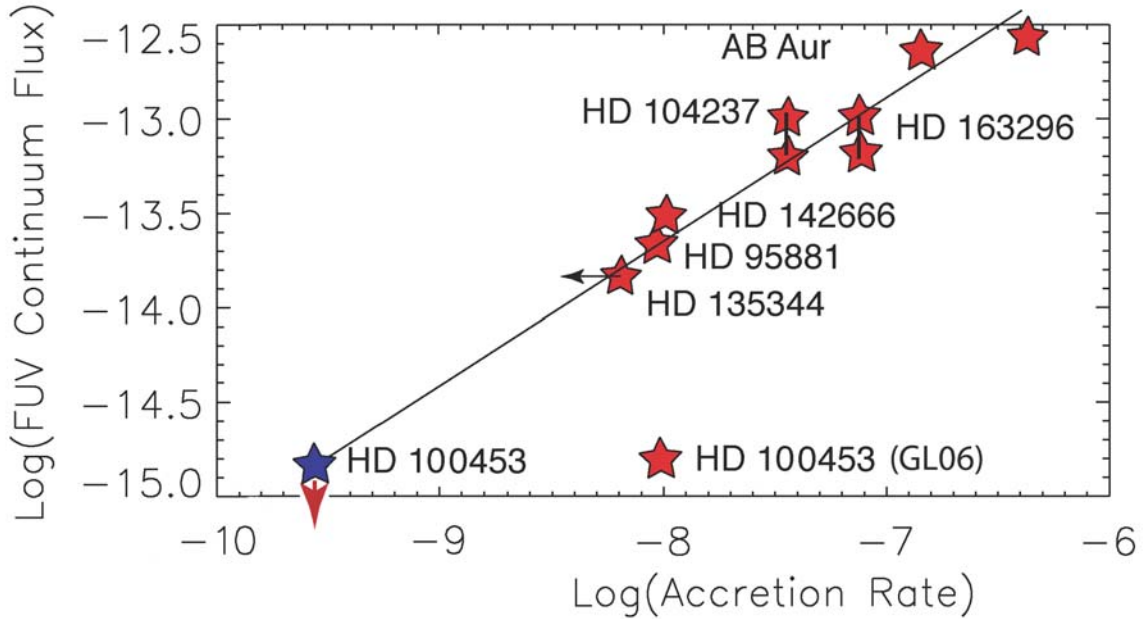


Figure 2.14. *log* FUV continuum vs. *log* accretion rate for Herbig Ae stars.

Accretion rates (determined from Br γ emission) are plotted in red against FUV continuum flux for several Herbig Ae stars. Note the linear relationship for all stars except HD 100453 (marked GL06), suggesting Br γ is contaminated by stellar activity. From our FUSE spectra, we extracted the *log* FUV continuum upper limit of -14.8 for HD 100453 and plotted it (in blue) on the line to estimate an accretion rate based on FUV continuum. The corresponding upper limit on accretion rate is $2.5 \times 10^{-10} M_{\odot} \text{ yr}^{-1}$.

Given the HD 100453B spectral type of M4.0V-M4.5V, we considered the UV spectrum of 2MASSWJ1207334-393254 (2M1207 hereafter) presented by Gizis et al. (2005). 2M1207 is a brown dwarf with spectral type of M8 and mass of $25 M_{\text{J}}$ (Gizis 2002) and is a weak accretor (Gizis et al. 2005). We used the 2M1207 UV emission lines detected by Gizis et al. (2005), scaled to the distance of HD 100453B, as a source in the ACS imaging exposure time calculator (ETC). The ETC shows that this weakly accreting

M8 brown dwarf would have been detected in our F122M imagery at above the 5σ level. Given our spectral type of M4.0V – M4.5V for HD 100453B, the non-detection of HD 100453B in our F122M image suggests that the candidate companion is non-accreting and is likely outside the disk of the primary.

2.3.4.3 Ca II $\lambda 8662$ Å Limits

Accretion rates based on the IR SED (D’Alessio et al. 2005) are biased toward the outer disk and can be significantly inaccurate for Herbig Ae type stars (Grady et al. 2007). However, Ca II $\lambda 8662$ Å traces material reaching the star and in certain cases is known to provide a more accurate indication of accretion rate. In classical T Tauri stars, the flux in the Ca II $\lambda 8662$ Å emission line is known to correlate very well with the accretion rate inferred via other means (Muzerolle, Hartmann & Calvet 1998). Mohanty et al. (2005) have extended this technique into the ultra low mass regime and have shown that Ca II $\lambda 8662$ Å is also a very good indicator of the accretion rate for brown dwarfs. We extend this technique to Herbig Ae stars.

Hamann & Persson (1992) present a survey of 32 Herbig Ae/Be stars including equivalent widths for various optical and NIR emission lines and found HD 163296 has a Ca II $\lambda 8662$ Å EW of 4.18 Å. Wassel et al. (2006) found that the accretion rate for HD 163296 is $1 \times 10^{-7} M_{\odot} \text{ yr}^{-1}$. Meeus et al. (2002) present HD 100453 observations conducted with the FEROS echelle spectrograph on the ESO 1.52 m telescope, covering parts of the 3700 – 9220 Å spectral range. However, the detailed spectra in the range of Ca II $\lambda 8662$ Å were not published, so we present them in this work (Figure 2.7). The Ca II $\lambda 8662$ Å line is in absorption and has no detectable emission component above 3σ . To determine an upper limit on Ca II $\lambda 8662$ Å emission EW, we assumed an unresolved

emission line well described by a Gaussian with height equal to 3σ of the normalized continuum in the feature-free region between $8652.78 - 8656.11 \text{ \AA}$, and with a FWHM equal to the FEROS spectral resolution of 0.18 \AA . We find a 4σ (2 pixel resolution element) upper limit on Ca II $\lambda 8662 \text{ \AA}$ EW of $4 \times 10^{-3} \text{ \AA}$ for HD 100453. Assuming a linear relation between Ca II $\lambda 8662 \text{ \AA}$ EW and accretion rate, we obtain a 4σ upper limit on the accretion rate for HD 100453 of $1 \times 10^{-10} M_{\odot} \text{ yr}^{-1}$. This estimate is consistent with the previous derived upper limit of $2.5 \times 10^{-10} M_{\odot} \text{ yr}^{-1}$ based on the FUV continuum level.

2.3.4.4 X-Ray Limits

From our Chandra data, L_x in the range $0.3 - 2 \text{ keV}$ for HD 100453A is $6.8 \times 10^{28} \text{ erg s}^{-1}$ and is just below the low end of the range for actively accreting Herbig Ae stars of $L_x \geq 10^{29} \text{ erg s}^{-1}$ (Hamaguchi et al. 2005; Swartz et al. 2005; Feigelson et al. 2003; Skinner et al. 2004; Stelzer et al. 2006a) but is $\sim 10^2$ higher than Beta Pictoris Moving Group (BPMG) early- to mid-A stars (Hempel et al. 2005). The spectrum is also much softer than typical for strongly accreting Herbig Ae stars and is $5\times$ below the T Tauri companion above 1 keV . It most closely resembles BPMG early F stars such as 51 Eri (Feigelson et al. 2006; Stelzer et al. 2006b), and is typical of X-ray production in winds. L_x / L_{bol} is also typical of early F stars, suggesting a similar magnetic field configuration. The X-ray luminosity is not indicative of strong mass accretion activity.

2.3.4.5 Jet and HH Knot Limits

We can derive a crude estimate on mass loss rate by using the fact that Herbig-Haro (HH) knots are Ly α bright (Grady et al. 2004; Devine et al. 2000) for low extinction lines of sight. HD 163296 has HH knot Lyman α surface brightness of about

$5 \times 10^{-14} \text{ erg cm}^{-2} \text{ s}^{-1} \text{ arcsec}^{-2}$ corresponding to a mass loss estimate of $1 \times 10^{-8} M_{\odot} \text{ yr}^{-1}$ (Wassell et al. 2006). Using the HST ACS ETC, HD 163296 knots would produce about $2.0 \text{ counts s}^{-1} \text{ arcsec}^{-2}$ in filter F122M. To detect extended sources in the HST F122M psf-subtracted image, we have binned the image into $1'' \times 1''$ pixels. The resulting background has a mean of $8 \times 10^{-4} \text{ counts s}^{-1} \text{ arcsec}^{-2}$ with $\sigma = 1 \times 10^{-4} \text{ counts s}^{-1} \text{ arcsec}^{-2}$. We find no surface brightness detections over $1'' \times 1''$ above a 3σ limit outside a $0''.2$ radius from the peak location of HD 100453A. Therefore, the HH knot surface brightness 3σ upper limit is $\sim 6000\times$ lower than the HD 163296 knot surface brightness. If we assume the worst case scenario that a knot is centered on the corner of a binned pixel, then only 25% of the counts will be in a single binned pixel and we must reduce the factor to 1500. Adjusting for distance, the overall scale factor is ~ 1700 . If we assume a linear relationship between knot surface brightness and mass loss rate, we obtain a crude upper limit for the HD 100453A mass loss of $6 \times 10^{-12} M_{\odot} \text{ yr}^{-1}$. The typical outflow rate to accretion rate scale factor of PMS stars is $\sim 10\%$ (Hartmann 2005), which implies an accretion rate upper limit for HD 100453A of $\sim 6 \times 10^{-11} M_{\odot} \text{ yr}^{-1}$. We find that even this crude methodology predicts an accretion rate upper limit that is consistent with the likely gas-deficient nature of the disk and the other four accretion rate indicators. Table 2.7 summarizes the accretion rate results.

Table 2.7Summary of Accretion Rate Indicators

Accretion Indicator	Accretion Level	Significance
FUV Continuum	$< 2.5 \times 10^{-10} M_{\odot} \text{ yr}^{-1}$	1σ
Lack of Ca II $\lambda 8662 \text{ \AA}$ emission line	$< 1.0 \times 10^{-10} M_{\odot} \text{ yr}^{-1}$	4σ
Lack of HH Knots in Ly α	$< \sim 6 \times 10^{-11} M_{\odot} \text{ yr}^{-1}$	factor of 10
H α	weak accretor	–
X-ray	not strong accretor	–
Adopted Accretion Rate Upper Limit	$< 2.5 \times 10^{-10} M_{\odot} \text{ yr}^{-1}$	$\sim 1-2\sigma$

2.3.5 Constraints on Disk Structure

The SED of HD 100453A has strong IR excesses in both the NIR and FIR (Meeus et al. 2002). However, it has an absence of small, warm dust emission from the disk surface compared to the average for Herbig Ae stars, as evidenced by a lack of the $10 \mu\text{m}$ silicate feature in its mid-IR spectrum (Meeus et al. 2001). Note however that large warm silicate grains of a few μm in size may still be present. Dominik et al. (2003) calculate stellar flux F_* from a source's SED by integrating the Kurucz model fit to the optical and UV spectrum (e.g. Figure 1.7). To compute the emission from the disk, they subtract the Kurucz model from the SED and integrate the excess flux from $2 - 7 \mu\text{m}$ to define F_{NIR} and from $7 \mu\text{m}$ to infinity to define F_{FIR} . The sources in the Meeus et al. (2001) have a mean $F_{\text{NIR}}/F_* = 0.16$ and mean $F_{\text{FIR}}/F_* = 0.23$. HD 100453A has $F_{\text{NIR}}/F_* = 0.22$ and $F_{\text{FIR}}/F_* = 0.29$, numerically demonstrating its higher than average excess in the NIR and

FIR. Such an SED suggests that dust intercepts a significant portion of the primary star's luminosity in both the inner and outer parts of the disk.

2.3.5.1 Spatially Resolved PAH Features

The mid-IR spectrum of HD 100453A is rich in polycyclic aromatic hydrocarbons (PAH) features, which have been spatially resolved out to $\sim 0''.3$ (Habart et al. 2006), or a projected distance of about 40 AU from the central star. The PAH emission decreases more rapidly than r^{-2} from a radial distance of $\sim 0''.1$ AU to $\sim 0''.3$ AU and could be due to low SNR in the data, a lack of carbon dust outside a radial distance of $\sim 0''.3$ AU, or low excitation conditions because of the late type of the central A star. Habart et al. (2006) describe the PAH detection as marginally resolved, but conclude that the small spatial extension seen in the system is real, based on simulated observations similar to those of HD 100453A.

2.3.5.2 Limiting Surface Brightness

Figure 2.9 illustrates the psf-subtracted, fully calibrated coronagraph image of HD 100453 in the HST/ACS/HRC F606W filter, using a linear intensity scale and a 3 pixel Gaussian kernel smoothing function. All of the observed features in this image within $\sim 3''.0$ of the central star are well known instrumental artifacts, whose characteristics and origin are discussed in depth elsewhere (Clampin et al. 2003; Krist et al. 2005). The alternating bands of positive and negative flux which dominate within a radial distance of $2''.25$ and extend to a lesser extent out to a radial distance of $3''.0$, as well as all narrow radial spikes, are residuals due to incomplete psf-subtraction. The minor extension of these residuals in the E–W direction (position angle of 90° and 270°)

is a known imperfection arising from the 3".0 diameter occulting spot and its occulting finger, which is seen at the eastern edge of the displayed field of view.

To establish the limiting null detection of HD 100453A's scattered light disk in the F606W filter, we extracted the median azimuthally averaged radial profile surface brightness behavior of the image. Outside of the region dominated by psf-subtraction residuals ($> 3".0$), the 1σ limiting surface brightness of the disk is 21.8 – 21.9 mag arcsec⁻² (Figure 2.15). As a more conservative estimate, Figure 2.15 also illustrates the 2σ limiting surface brightness of the scattered light disk, which is $\sim 21.1 - 21.2$ mag arcsec⁻² outside of 3".0.

The non-detection of the scattered light disk outside the 0".9 diameter occulting spot could indicate a complete absence of material at $r > 0".9$, or that dust at $r > 0".9$ is not being illuminated, or that the grain size distribution or optical depth of the disk is such that little scattered light is produced in the F606W filter band.

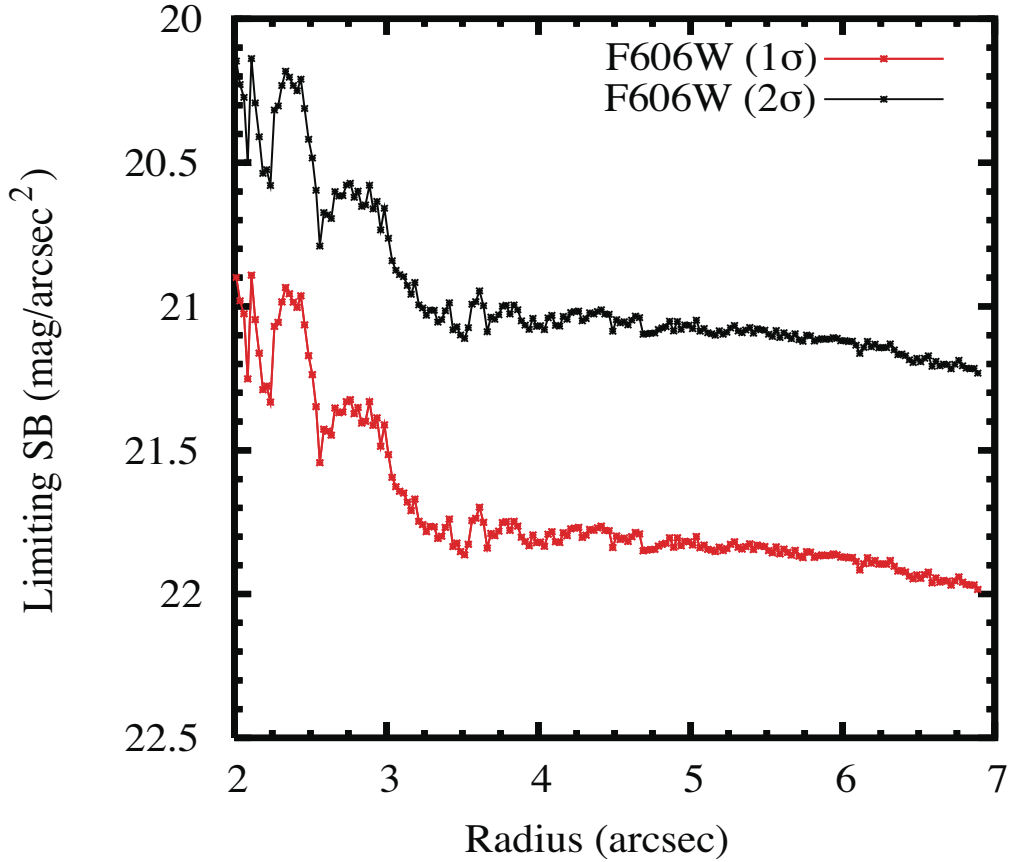


Figure 2.15. Limiting surface brightness of HD 100453A’s scattered light disk.

We have a null detection of the scattered light disk in our F606W data. Both the 1σ (red) and 2σ (black) limiting surface brightness detection levels were computed from median azimuthally averaged radial profiles of the system.

2.3.5.3 The Inner Disk

Carmona et al. (2008) searched for H_2 $0 - 0$ S (2) ($J = 4 - 2$) emission at $12.278 \mu\text{m}$ and H_2 $0 - 0$ S (1) ($J = 3 - 1$) emission at $17.035 \mu\text{m}$ and did not detect either toward HD 100453A. Stringent 3σ upper limits to the integrated line fluxes and the mass of optically thin warm gas ($T = 150, 300$ and 1000 K) in the disks were derived. They determined that the disk of HD 100453A contains less than a few tenths of Jupiter mass

of optically thin H₂ gas at 150 K, and less than a few Earth masses of optically thin H₂ gas at 300 K and higher temperatures.

Brittain et al. (2007) detected warm CO P30 and P31 emission around every Herbig Ae/Be star with an optically thick disk, i.e., $E(K - L) > 1$. Although $E(K - L) = 1.3$ for HD 100453A, we detect no CO emission lines in the Phoenix echelle spectrograph data near 4.97 μm (Figure 2.6). Figure 2.16 illustrates the relationship between CO luminosity and NIR excess for several sources discussed in Brittain et al. (2007) and HD 100453A (the filled oval). It is clear that HD 100453A is an anomaly.

To determine an upper limit on P30 luminosity, we assumed an unresolved emission line well described by a Gaussian instrument profile with height equal to the standard deviation of the normalized continuum. Based on the M-band magnitude given in Malfait et al. (1998), our derived 2σ upper limit on P30 line luminosity is 1×10^{20} W. Figure 2.17 illustrates CO luminosity vs. mass accretion rate for several sources discussed in Brittain et al. (2007) and HD 100453A (the filled oval). The luminosity and accretion rate data were taken from Brittain et al. (2007) except for HD 100453A. The HD 100453A upper limit on mass accretion rate plotted is the average of the mass accretion rate upper limits determined by three methods previously in this work. We see that the HD 100453A data point is consistent with a general relationship between CO luminosity and mass accretion rate.

We see no pumped Fe II emission in the FUSE data (Figure 2.5d). Three scenarios can lead to this result. First, if there is high extinction toward HD 100453A, the Fe II emission may not be detected. However, there is very low extinction toward HD 100453A. Second, if there is no Lyman α to pump the transitions, we will detect no

Fe II emission. However, IUE SWP53937 shows well-exposed Lyman α emission superposed on the geocoronal background in the large ($20'' \times 10''$) aperture. Third, no gas within 1 AU of a star will result in an Fe II non-detection (Harper et al. 2001). An Fe II non-detection with low extinction and abundant Lyman α to pump suggests no atomic Fe II within 1 AU of HD 100453A.

We compare X-ray pumped Ne II $\lambda 12.8 \mu\text{m}$ emission from HD 100453A to the spectral type G8 T Tauri star T Chamaeleontis (T Cha), which is a ROSAT All-Sky Survey (RASS) X-ray source with $\log L_x \geq 29.9$ and $d \geq 140$ pc (Alcala et al. 1993) and which has a transitional disk (Lahuis et al. 2007). We scale this luminosity using an updated estimate of $d = 63$ pc (Lahuis et al. 2007), and obtain $\log L_x \approx 29.2$. T Cha has an observed Ne II $\lambda 12.8 \mu\text{m}$ line flux of $3.2 \times 10^{-14} \text{ erg cm}^{-2} \text{ s}^{-1}$ (Lahuis et al. 2007). Scaling the Ne II line flux to the distance of HD 100453A, we obtain $1 \times 10^{-14} \text{ erg cm}^{-2} \text{ s}^{-1}$.

HD 100453 is an X-ray source with $\log L_x = 28.8$. Scaling from the T Cha line flux and X-ray luminosity, for an equivalent inner disk gas density, we expect an HD 100453A Ne II $\lambda 12.8 \mu\text{m}$ line flux of $4 \times 10^{-15} \text{ erg cm}^{-2} \text{ s}^{-1}$. Investigating Spitzer IRS spectra for HD 100453A, we find no evidence of a Ne II $\lambda 12.8 \mu\text{m}$ emission line. However, due to the noise in the spectral region of $12.8 \mu\text{m}$, the 3σ upper limit on detection of the Ne II line is $5 \times 10^{-14} \text{ erg cm}^{-2} \text{ s}^{-1}$. Thus, we cannot reliably exclude the existence of Ne II gas, at the density of T Cha, in the inner disk of HD 100453A.

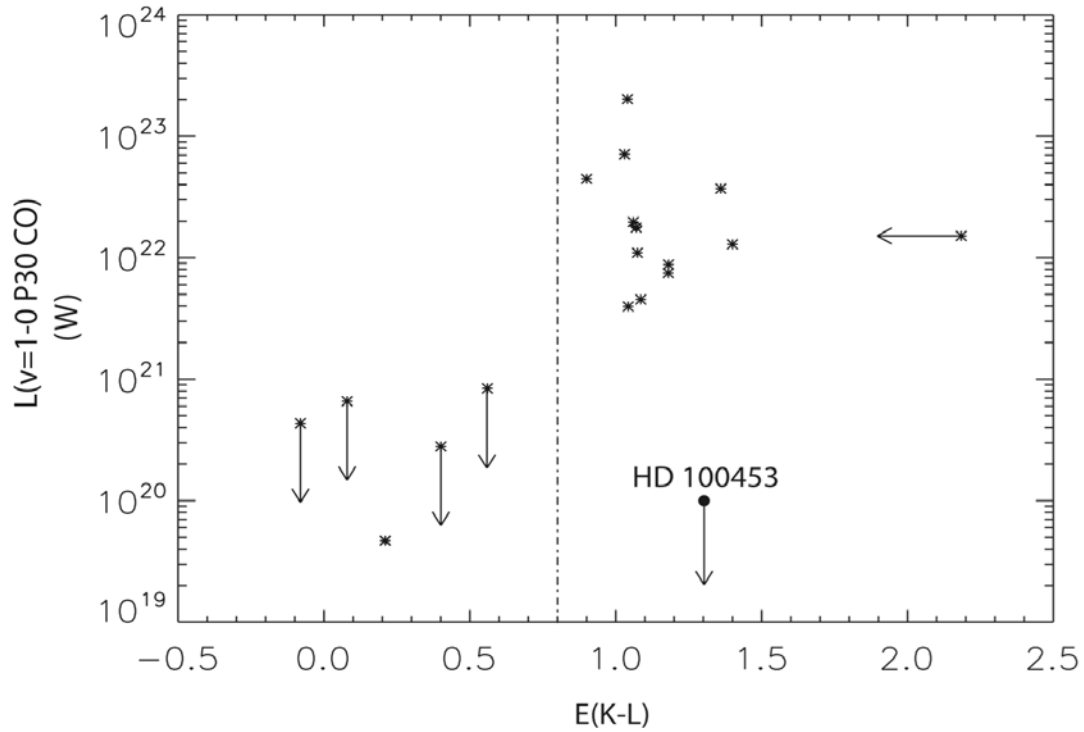


Figure 2.16. Herbig Ae/Be star CO luminosity vs. NIR excess.

All of the Herbig Ae/Be stars with an optically thick disk (i.e. $E(K - L) > 1$) have detected CO emission, except HD 100453A which is indicated by the filled circle (after Brittain et al. 2007). We set a 2σ upper limit for the luminosity of HD 100453 of 1×10^{20} W, based on the noise floor of the spectrum. A level of $E(K - L) = 1.3$ indicates hot dust in the system and no CO emission suggests reduced levels of gas within ~ 1 AU. The combination suggests an advanced evolutionary state of the circumstellar disk.

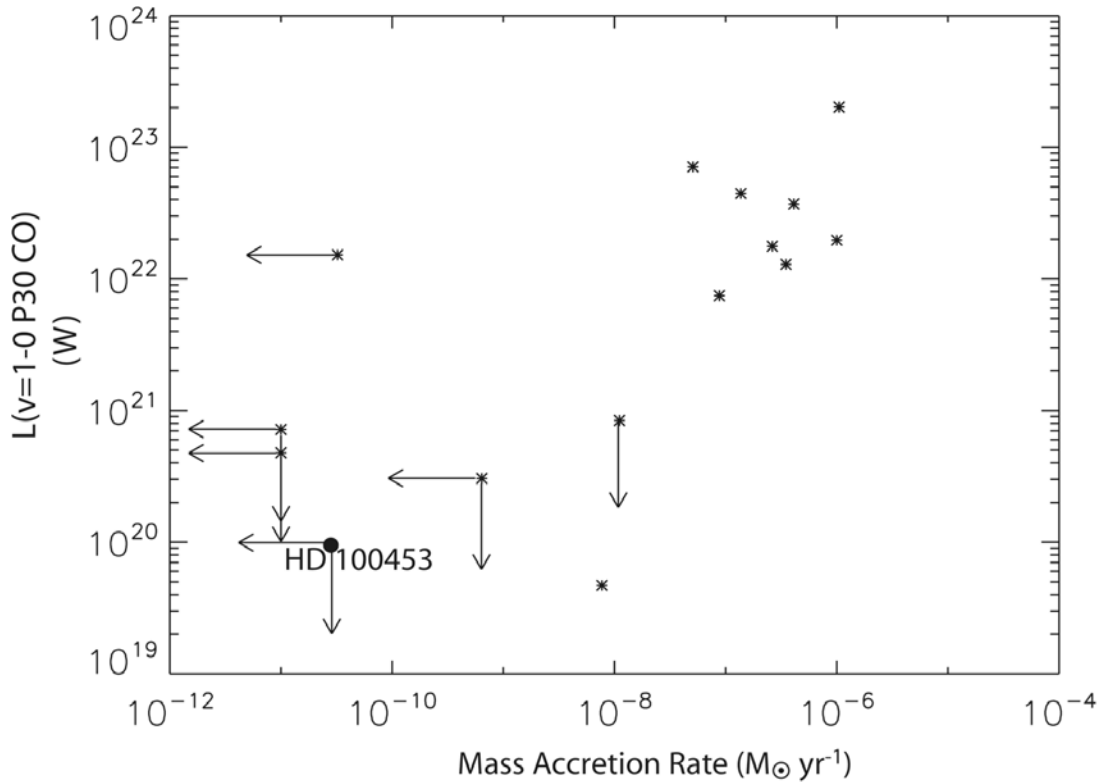


Figure 2.17. Herbig Ae/Be star CO luminosity vs. mass accretion rate.

The luminosity and accretion rate data were taken from Brittain et al. (2007) except for HD 100453 (the filled circle). The 2σ upper limit on luminosity for HD 100453 of 1×10^{20} W was determined from the noise level within the observed spectrum and assuming a Gaussian instrumental line profile. The upper limit on mass accretion rate plotted is the average of the mass accretion rate upper limits determined by three methods within this work (see § 2.3.4). We see that the HD 100453 data point is consistent with a general relationship between CO luminosity and mass accretion rate.

2.3.5.4 The Outer Disk

We detect no $^{12}\text{CO } J = 3-2$ (868 μm) emission toward HD 100453A/B.

The 1σ upper limit on the integrated intensity in binned 10 km s^{-1} channels is

$I_{\text{CO}} < 0.0077 \text{ K km s}^{-1}$. Compared to the CO survey by Dent et al. (2005), our non-detection, normalized to a distance of 100 pc, corresponds to an integrated intensity, $I_{\text{CO}} < 0.01 \text{ K km s}^{-1}$, an order of magnitude lower than any of their detections.

The 3σ upper limit on the integrated intensity in binned 5 km s^{-1} channels is $I_{\text{CO}} < 0.042 \text{ K km s}^{-1}$. This corresponds to a 3σ upper limit on CO column density of $N_{\text{CO}} < 2.0 \times 10^{13} \text{ cm}^{-2}$, which is well below the optically thin condition ($N_{\text{CO}} < 1 \times 10^{15} \text{ cm}^{-2}$). The 3σ upper limit on $N_{\text{CO}} < 2.0 \times 10^{13} \text{ cm}^{-2}$ corresponds to a 3σ upper limit on the cold gas mass of $< 1.7 \times 10^{-4} M_{\text{J}}$ (following Scoville et al. 1986), assuming an excitation temperature of 50 K, a CO abundance of $[\text{CO}]/[\text{H}_2] = 1 \times 10^{-4}$ (as in the ISM), optically thin emission, and allowing for 10% He by number.

Meeus et al. (2002, 2003) detected strong continuum emission at 1.2 mm. The conversion to mass depends on the value of the dust opacity per unit mass, κ . For $\kappa = 2.5 \text{ cm}^2 \text{ g}^{-1}$, appropriate for protoplanetary disks at this wavelength, the measured flux of 265 mJy corresponds to a dust mass of $0.08 M_{\text{J}}$ (following Andrews & Williams 2005). For debris disks, $\kappa = 1.2 \text{ cm}^2 \text{ g}^{-1}$ (scaled from a value at $850 \mu\text{m}$ in Zuckerman & Becklin 1993), the inferred dust mass is $0.16 M_{\text{J}}$. The mass is approximately linearly dependent on temperature and we have assumed 50 K in the above. In either case, the gas-to-dust ratio in the cold outer disk (more than $\sim 20 \text{ AU}$ from the central star) is no more than 2×10^{-3} , assuming optically thin emission and a CO abundance typical of the ISM. If the CO is significantly depleted by a factor of 1000, then the total cold gas mass upper limit is $0.17 M_{\text{J}}$, which corresponds to a gas-to-dust ratio of no more than 2:1 in the outer disk.

2.4. Discussion

HD 100453A is currently the oldest known Herbig Ae star and is coeval with the Beta Pictoris moving group. The disk is intermediate in character between those associated with younger, actively accreting Herbig Ae stars, and debris disks. Despite the large NIR excess, there is no compelling evidence for molecular gas residing in the disk or accretion onto the star.

Figure 2.18 summarizes the known constraints on the disk structure. The inner rim of the disk is estimated to be at less than ~ 0.5 AU based on the effective temperature of the NIR black body component. The outer disk radius is >40 AU based on the PAH data, the scattered light disk outer radius is <250 AU based on the HST coronagraphic data, and the disk is optically thin (in the optical and NIR) by a projected radius of 90 AU (an uncertain quantity, because the system inclination is not well constrained) based on the detection of star C, which is likely a background star. The companion is at a projected distance of ~ 120 AU, and the trough in the SED between the NIR and MIR black body components may indicate a shadowed region or a gap in the disk.

We have analyzed three quantitative accretion rate indicators (non-detections of FUV continuum, Ca II emission, and jets/knots) and two qualitative accretion rate indicators (H α and X-ray emission) in this work. While it can be argued that any one of the indicators may not firmly constrain the accretion rate, the combination of all five is quite meaningful. From our FUSE, FEROS Ca II $\lambda 8662$ Å, and HST/ACS SBC data, we find that three independent observations and methodologies result in accretion rate upper limits between 2.5×10^{-10} and $6 \times 10^{-11} M_{\odot} \text{ yr}^{-1}$. In addition, variable, weak H α emission is sometimes present, and may indicate either variable stellar activity or variable, low levels

of accretion, but this will need to be further explored. We adopt an accretion rate upper limit of $2.5 \times 10^{-10} M_{\odot} \text{ yr}^{-1}$ ($\sim 1-2\sigma$).

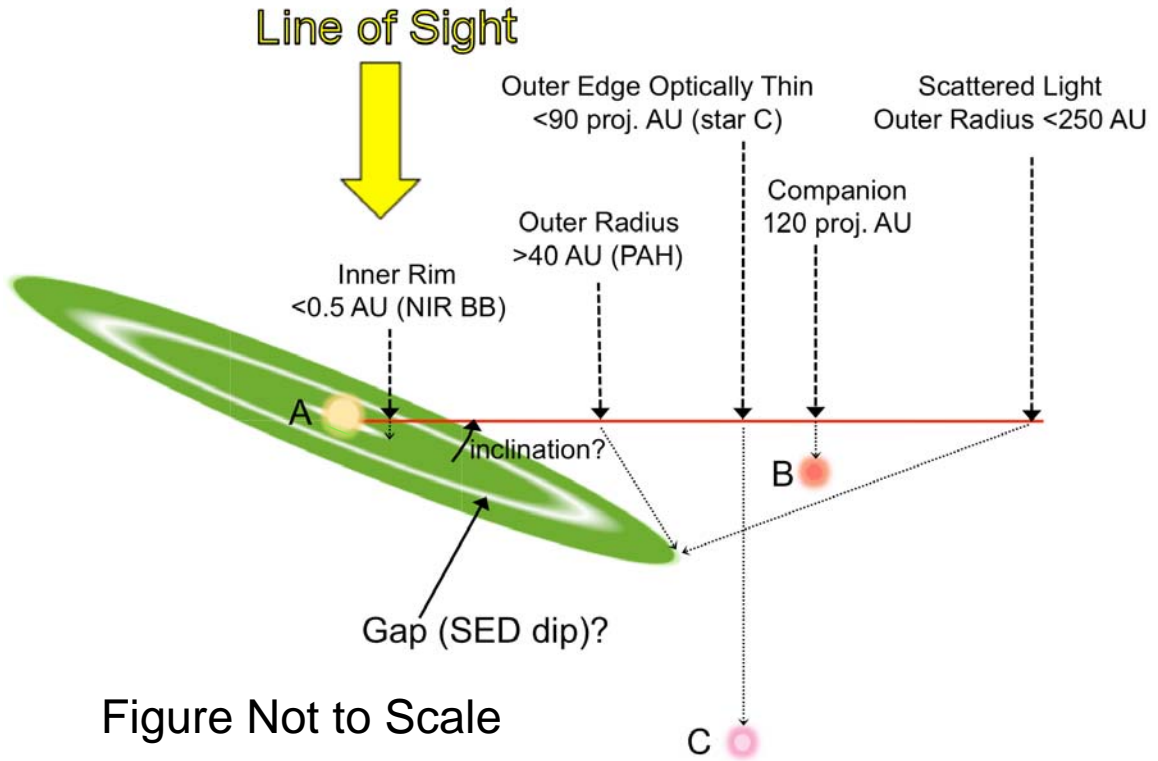


Figure Not to Scale

Figure 2.18. Summary of Disk Structure Constraints.

HD 100453A, HD 100453B, and star C are shown along with the disk environment oriented at an arbitrary angle (as the system inclination is not well constrained). The outer radius is likely >40 AU based on the PAH data, and the scattered light disk is <250 AU. The outer edge of the disk is optically thin by a projected radius of <90 AU. The trough in the SED between the NIR and MIR black body components may indicate a shadowed region or a gap in the disk.

The non-detection of warm CO and H₂ emission toward HD 100453A indicates that there is little optically thin gas in the inner disk ($R < 20$ AU). Carmona et al. (2008) found that the disk of HD 100453A contains less than 0.1 M_J of optically thin H₂ gas at 150 K, and less than an Earth mass of optically thin H₂ gas at 300 K and higher temperatures. This has two possible explanations. (1) The first is that little warm gas (CO and H₂) and dust exist in the inner disk. The medium is optically thin (because of the low density of dust), but the mass of gas is so low that the emission flux level is not detectable. (2) The second possibility is that there is warm gas residing in the optically thick disk midplane. In this case, any line emission originates from the optically thin molecular surface layer of the disk. However, there is so little gas in the surface layer that the emission level is not detectable (Carmona et al. 2008). Present data do not allow us to distinguish between these two scenarios, but our very low accretion rate upper limit suggests reduced amounts of gas in the inner disk, even for the optically thick case.

Our non-detection of cold CO emission (3σ upper limit of $N_{\text{CO}} < 2.0 \times 10^{13} \text{ cm}^{-2}$) meets the optically thin condition ($N_{\text{CO}} < 1 \times 10^{15} \text{ cm}^{-2}$). However, it is likely that the cold CO is depleted due to the freezing of gas molecules onto dust particle surfaces, and once frozen onto dust particles, we do not detect the CO molecules. For the case of significant CO depletion by a factor of 1000 compared to the canonical ISM abundance, we find an upper limit on the gas:dust ratio of $\sim 2:1$, which is quite low compared to the typical ratio of 100:1 in a gas-rich protoplanetary disk. We therefore conclude that the outer disk is gas-poor and that substantial gas has been removed from the disk environment.

At an age of 14 ± 4 Myr, HD 100453A maintains high levels of NIR and FIR excess, an absence of accretion signatures across a large range of wavelengths, and

insignificant amounts of warm and cold molecular gas in the disk. The combination of these features suggests the disk of HD 100453A does not fit the classical definition of a protoplanetary disk, a transitional disk, or a debris disk. The high level of NIR excess indicates the inner disk is still surviving and excludes HD 100453A from the transitional disk and debris disk classifications. HD 100453A is a rather old PMS star where the inner disk is surviving on a surprisingly longer timescale than is typically expected (Strom et al. 1989). Its gas-poor nature excludes it from the protoplanetary disk classification.

In order to produce the levels of IR excess associated with HD 100453A, the dust in the disk must intercept a significant portion of the star's luminosity, which is inconsistent with a flat disk geometry. Meeus et al. (2001) included HD 100453A as a member of group I, which contains stars for which the continuum can be reconstructed by a power-law and a black body in the mid-IR. Furthermore, they suggest a flaring disk as a possible physical geometry that could explain such an SED. Flared disks require some level of gas to sustain hydrostatic equilibrium (Chiang & Goldreich 1997), which determines the scale height in the disk. If the disk of HD 100453A is indeed flared, some level of gas must still exist within the disk.

An alternate explanation could be that HD 100453A is a debris disk, and that the IR excess we detect is from mostly second-generation dust that is being created and dispersed from the disk midplane by collisions of massive bodies within the disk (e.g., Habing et al. 2001). Only a small amount of dust ($< 0.1 M_J$) is required to produce the observed SED. The gas-poor nature of the disk suggests that this explanation might be favored over a typical flared disk geometry.

If HD 100453 does indeed have undetected, optically thick gas in the inner disk, it is remarkable that very little, if any, is accreting onto the star. However, this could be explained by a massive body orbiting HD 100453A inside the inner rim of the disk, similar to TW Hydrae (Setiawan et al. 2008). In this case, the disk could still be in the transitional phase, but the gas-giant has cut off the accretion flow to the star and may have accreted much of the gas from the disk.

The M-type companion located at a projected distance of 120 AU from the primary star is likely to have tidally truncated the outer edge of the disk. Although tidal truncation is possible in any case, it is better constrained if the companion is in the plane of the disk, and if the disk is geometrically thin and is primarily governed by gas pressure and viscosity, but not by self-gravity (Artymowicz & Lubow 1994). With these assumptions, and for the mass ratio of HD 100453A and its companion, Artymowicz & Lubow (1994) predict the outer edge of the disk will be truncated at a projected distance of ~ 50 AU, assuming a circular orbit, and even closer in, if the orbit of the companion is eccentric. A projected disk outer radius of 40 – 50 AU is in agreement with the spatially resolved PAH emission out to a projected distance of ~ 40 AU, and the detection of a likely background star at a projected distance of ~ 90 AU.

Low-mass stellar companions can be reliably identified via their X-ray fluxes and spectra, and with lower contrast to the central A star via their UV emission. No companion objects to HD 100453A were seen in close proximity to the star in the HST/ACS/SBC psf-subtracted Ly α imagery. The ACS F122M imagery firmly excludes the presence of any object more luminous than M3.5V within the disk, exterior to $0''.3$. The detection limit is M3.0V at $0''.25$, and M0V at $0''.125$. Our Chandra data indicate that

any source with a spectrum similar to the $1''.05$ companion to HD 100453A must be $2\times$ less X-ray luminous, thus excluding a stellar coronal source down to M5.0V. Non-accreting brown dwarfs have X-ray spectra similar to HD 100453A at $t = 8$ Myr (Tsuboi et al. 2003), but are an order of magnitude fainter than the Chandra source at the location of the Herbig star. Thus, we cannot exclude the presence of a sub-stellar X-ray source, such as a brown dwarf (generally, spectral types later than M5), within the disk of HD 100453A. While wide star + brown dwarf binaries are known for both the TW Hya association and the BPMG (Feigelson et al. 2006; Stelzer et al. 2006b), none have been identified within 50 AU of a Herbig Ae primary and moreover, residing within a protoplanetary disk.

2.5. Summary of Results

In this work, we have used multi-wavelength observations from the X-ray to the millimeter to confirm the binary hypothesis, refine the age of the system, determine the accretion rate, and to constrain the size, gas content, and dust content of the disk environment of HD 100453A.

- We find that HD 100453B is indeed the physical companion to HD 100453A and is separated by a projected distance of about 120 AU and has $L_x/L_{\text{bol}} = -3.51$, confirming that HD 100453B is a T Tauri star.
- We find that the age of the system is 14 ± 4 Myr and that the mass of the companion is $0.21 - 0.30 M_{\odot}$.
- We find little evidence of accretion or jet activity for HD 100453A. Our data suggest an accretion rate upper limit of $2.5 \times 10^{-10} M_{\odot} \text{ yr}^{-1}$ ($\sim 1-2\sigma$), using five independent methods.
- PAH emission from the disk is marginally resolved out to ~ 40 AU (Habart et al. 2006), but we detect a likely background star at $\sim 0''.8$ (projected distance of ~ 90 AU), and we see no evidence of a scattered light disk outside $2''.25$ (~ 250 AU). It is possible that the disk has been tidally truncated by the companion at less than a projected distance of ~ 50 AU.
- Based on the 1.2 mm continuum flux from the literature, we find that the disk of HD 100453A contains $\sim 0.1 M_J$ of cold dust.

- The combination of *at best* a very low accretion rate and the non-detection of several gas tracers suggests that the disk is gas-poor. We find that the CO $J = 3-2$ emission is optically thin, the disk contains no more than $\sim 0.2 M_J$ of cold molecular gas, and the gas to dust ratio is no more than ~ 2 in the outer disk (assuming $[CO]/[H_2]$ abundance of 1×10^{-4} and a depletion factor of 1000).
- The disk characteristics of HD 100453A do not fit the classical definition of a protoplanetary disk, a transitional disk, or a debris disk. The characteristics may define a new class of objects that link gas-rich protoplanetary disks and gas-poor debris disks. These objects maintain a high level of NIR and FIR excess, but have no detectable cold, warm, or hot molecular gas.
- It is possible that the disk of HD 100453 is in the debris disk phase, and that the relatively small amount of dust that is intercepting a significant portion of the star's luminosity is from mostly second-generation dust that is being created and dispersed from the midplane by collisions of massive bodies within the disk.

High resolution, high contrast optical observations with an occulting disk $\leq 0''.3$ in radius are needed to image the disk in scattered light. Additional epochs of proper motion data are required to determine the orbital dynamics of the B companion and to confirm that star C is a background star.

3. CONCLUSIONS

Meeus et al. (2001) classified 14 Herbig Ae stars into two groups and suggested that sources evolve from Group I to Group II based on three characteristics of the SED (see § 1.4). The characteristics are (1) a blackbody component, or lack thereof, in the mid-IR, (2) the ratio of total IR excess luminosity to the luminosity of the central star, and (3) the slope of the SED at submillimeter wavelengths. **The goal of this thesis is to test the hypothesis that Meeus Group I sources evolve to Meeus group II sources.**

3.1 Results of the Thesis Statement Test

To test the hypothesis, we need age estimates for the stars in Meeus Groups I and II. Four of the eight Meeus Group I sources and two of the six Meeus group II sources do not have age estimates in the Meeus et al. (2001) paper. From the results of this thesis, Grady et al. (2007), van Boekel et al. (2005), and Carmona et al. (2007, 2008), all of the Meeus Group I and II objects now have age estimates. These new age estimates are combined with updated age estimates from the literature for other Group I and II sources and are summarized in Table 3.1.

Accretion rates from Garcia Lopez et al. (2006), based on the luminosity of the Br γ emission line, are also included in Table 3.1. In § 2.3.4.2, we infer that the Br γ emission line has a substantial stellar activity component for HD 100453, causing the corresponding Garcia Lopez et al. (2006) accretion rate to be too high. To keep the systematic error introduced by activity consistent across all sources, we use the Br γ based

accretion rate for HD 100453 in the table, instead of the more stringent upper limit determined in the work.

The mean ages of the Group I and Group II sources are 6.7 Myr and 5.2 Myr, respectively (Table 3.1), suggesting that Group II disks evolve to Group I disks, opposite of the Meeus et al. (2001) prediction. However, the difference in mean age between the groups is not statistically significant ($<1\sigma$), and the range of values is consistent between the two groups. **From a stellar age perspective, it is clear that the Meeus Group I sources do not, in general, evolve to Meeus Group II sources.**

Meeus et al. (2001) suggest that if this result is determined, it could be explained if the timescales over which stars and disks evolve are not strongly coupled for the sample of 14 Herbig stars. As discussed in § 1.3, accretion is expected to slow as a disk evolves. The mean accretion rates for the Group I and Group II sources are $3\times 10^{-8} M_{\odot} \text{ yr}^{-1}$ and $6\times 10^{-8} M_{\odot} \text{ yr}^{-1}$ (Table 3.1), suggesting that Group II disks evolve to Group I disks, opposite of the Meeus et al. (2001) prediction. However, the difference in mean accretion rate is not statistically significant ($<1\sigma$), and the range of values is consistent between the two groups. **From an accretion rate perspective, it is clear that the Meeus Group I disks do not, in general, evolve to Meeus Group II disks.**

Figure 3.1 shows accretion rate plotted as a function of stellar age for the sources in Meeus et al. (2001). A strong correlation can be seen between increasing age and decreasing accretion rate. For the Meeus sources, apparently the star, disk, and accretion rate evolve together.

We conclude that the hypothesis suggesting Meeus Group I sources evolve to Meeus Group II sources does not hold. However, this result should be confirmed with a larger sample.

Table 3.1

Summary of Meeus Group I and II age estimates

Meeus Group	Source	Sp. Type	L_{IR}/L_*	\log Accr. Rate ^a (M_{\odot}/yr)	Age (Myr)	Age Reference
I	AB Aur	A0Ve	0.48	-6.85	2	van den Ancker et al. (1999)
I	HD 100546	B9Ve	0.51	-	~10	van den Ancker et al. (1999)
I	HD 142527	F7IIIe	1.06	-7.16	2	Fukagawa et al. (2006)
I	HD 179218	B9e	0.62	-6.59	1.2	van Boekel et al. (2005)
I	HD 100453	A9Ve	0.54	-8.04	14	(this work)
I	HD 135344	F4Ve	0.44	-8.27	8	van Boekel et al. (2005)
I	HD 139614	A7Ve	0.39	-7.99	~10	van Boekel et al. (2005)
I	HD 169142	A5Ve	0.10	-7.40	6	Grady et al. (2007)
Group I Mean Values			0.52	-7.47	6.7	
II	HD 104237	A4Ve	0.13	-7.45	2	van Boekel et al. (2005)
II	HD 142666	A8Ve	0.28	-8.00	6	Carmona et al. (2008)
II	HD 144432	A9Ve	0.26	-7.07	8	Carmona et al. (2007)
II	HD 150193	A1Ve	0.15	-7.29	10	Carmona et al. (2007)
II	HD 163296	A3Ve	0.16	-7.12	5	van Boekel et al. (2005)
II	51 Oph	A0Ve	0.02	-6.27	0.3	van den Ancker et al. (1999)
Group II Mean Values			0.17	-7.20	5.2	

^aaccretion rates based on luminosity of Bry emission line (Garcia Lopez et al. 2006)

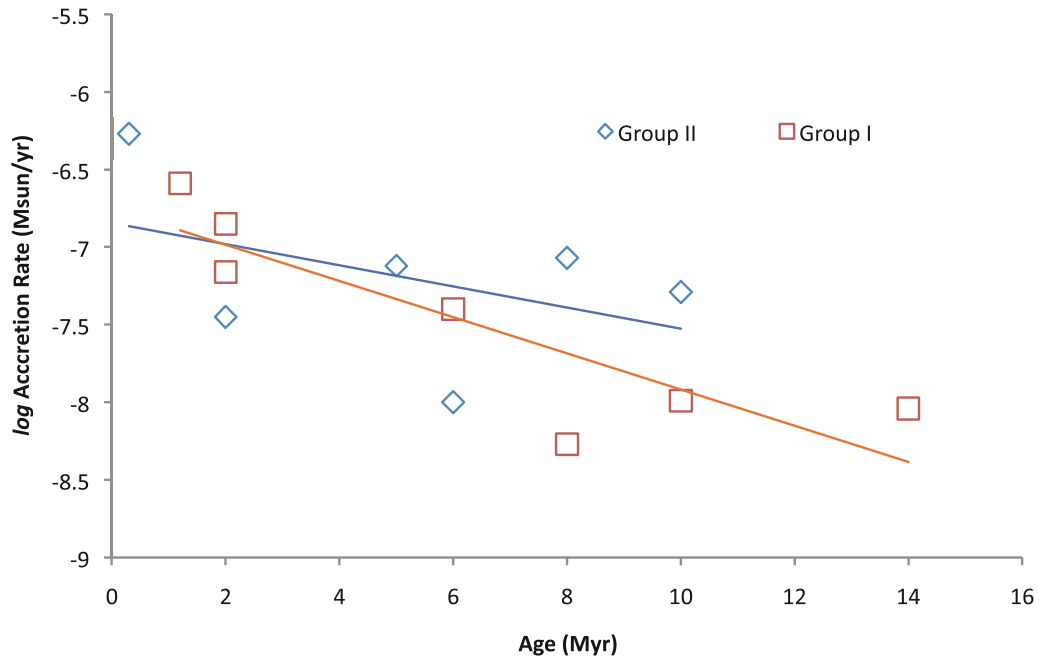


Figure 3.1. Age vs. *log* accretion rate for the Group I and Group II sources .

Meeus Group I sources are plotted as orange squares, and Meeus Group II sources are plotted as blue diamonds (data from Table 3.1). The solid lines show the best linear fit to the data. It is clear that accretion rate decreases as a star ages. The typical error in age is about $\pm 30\%$.

3.2 Possible Physical Explanations

The failure of the Meeus et al. (2001) hypothesis to hold can be explained by physical and dynamical properties of the disk environment. Meeus et al. (2001) assign sources to the two groups based on three characteristics of the SED.

The first characteristic of a Group I source is the existence of a blackbody component in the mid-IR of the SED. Meeus et al. (2001) explained this by assuming a mostly optically thin inner disk, which allows the star to illuminate the outer disk surface, causing it to flare and produce the blackbody component. The mid-IR blackbody

component can also be the result of a more evolved disk with a cavity between an inner and outer disk structure. An example is the Meeus Group I source HD 100546. Bouwman et al. (2003) model its SED and study its spectral features and find that a cavity has likely developed within the disk (Figure 3.2). The presence of this cavity has been confirmed by mid-IR interferometric measurements (Liu et al. 2003) and Hubble Space Telescope STIS observations (Grady et al. 2005). The inner rims of the inner disk and outer disk are directly illuminated by the star causing a near-IR and mid-IR blackbody component in its SED, respectively (see Figure 1.7b). A collisional cascade induced by a possible giant planet in the cavity is producing dust grains and throwing them up and out of the disk midplane. The small grains are blown away by radiation pressure and rain down on the surface of the outer disk.

The second characteristic of a Group I source is a high level of NIR and FIR excess. A star's total IR excess is expected to decrease as grains grow, since small dust grains radiate more efficiently than larger grains. However, we see in the HD 100546 example that emission from small grains may increase as a disk evolves and collisional episodes occur. As a PMS star evolves, its total IR excess will likely fluctuate significantly due to periods of high and low collisional activity.

The third characteristic of the SED considered by Meeus et al. (2001) is the sub-mm slope. When comparing grains from similar regions of a disk, larger grains radiate at longer wavelengths than smaller grains. Therefore, large grains tend to create shallower slopes in the sub-mm than small grains. However, we have seen that small grains likely exist in evolved disks that are experiencing high levels of collisions.

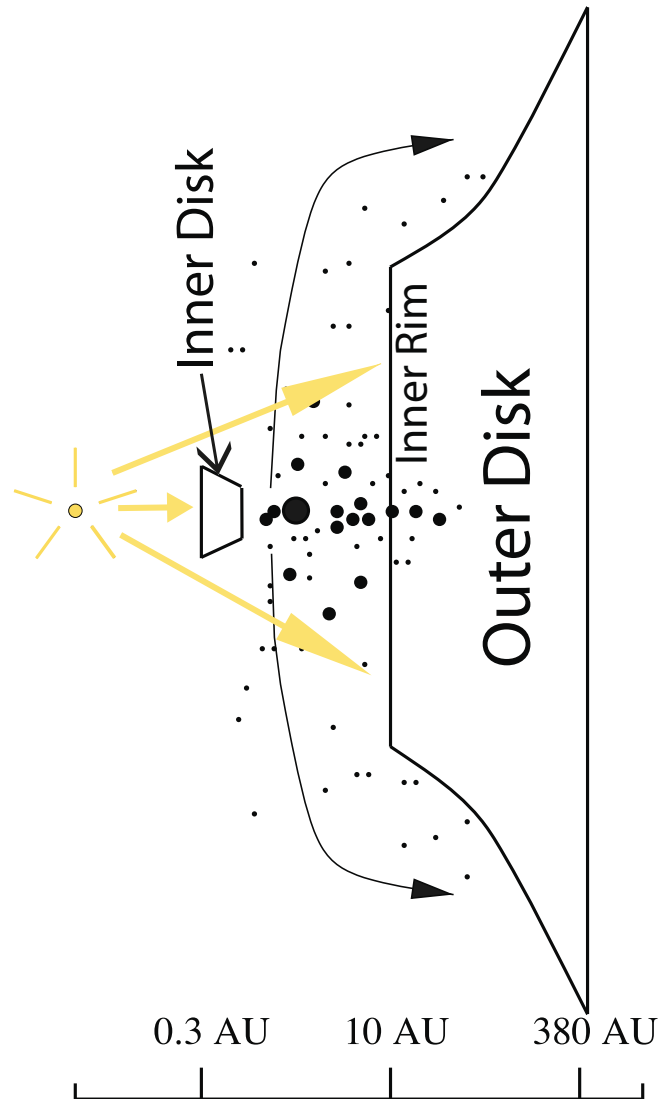


Figure 3.2. Schematic representation of the HD 100546 system.

A giant planet has formed a gap in the flaring disk at ~ 10 AU. The inner rim of the outer disk is directly illuminated by the star causing a large mid-IR blackbody component in the SED (see Figure 1.7b). A collisional cascade induced by the giant planet is producing dust grains and throwing them up and out of the disk midplane. The small grains are blown away by radiation pressure and rain down on the surface of the outer disk (after Bouwman et al. 2003)

It is clear that SED shape, total IR excess, and sub-mm slope are not indicators of a unique phase in the evolution of a circumstellar disk. In particular, an SED exhibiting a blackbody component in the mid-IR, a high level of total IR excess, and a steep sub-mm slope can represent both a protoplanetary flared disk with an optically thin inner disk, and a more evolved disk which has a cavity between the inner and outer disk and which is experiencing collisions of massive bodies that create small dust grains. **It appears that the Meeus groups may be more representative of differences in disk structure rather than differences in disk evolution.** Figure 3.3 shows the SED continua of HD 100546, HD 100453A, and HD 169142. All three of these Meeus Group I sources show a strong mid-IR blackbody component in the SED and are relatively old Herbig Ae/Be stars. Modeling of the SED of HD 169142 (Grady et al. 2007) suggests that a gap exists within the disk and that the mid-IR blackbody component of the SED is caused by a flaring outer disk having an inner radius of ~ 44 AU. The minimal NIR excess of this source suggests that the inner disk is geometrically thin rather than vertically extended.

The SED of HD 100453A is similar to HD 100546 in both the NIR and MIR, however the NIR blackbody component of HD 100453A is stronger. This suggests that the outer edge of the inner disk may extend farther out than the outer edge of the inner disk of HD 100546, and/or its inner disk is more vertically extended than the inner disk of HD 100546. The dust-rich, gas-poor nature of HD 100453A, at an age of 14 ± 4 Myr, is consistent with the current observational investigations of our solar system and theoretical studies that indicate that gas-giant planets form in less than ~ 10 Myr and Earth-like terrestrial planets in less than ~ 30 Myr (Zuckerman & Song 2004). The age range of HD 100453A overlaps these important epochs of planet formation and the

system should be considered for future studies to determine if planets have formed, or are in the process of forming, around this older Herbig Ae star.

3.3 Future Directions

To lift the degeneracies in disk structure allowed by knowledge of SED shape, total IR excess, and sub-mm slope, one needs high contrast, high spatial resolution imaging and high spatial resolution interferometry. These capabilities are available from instrumentation today and are being enhanced by a new generation of ground-based and space-based observatories and instruments.

3.3.1 NICMOS on HST

The Near-Infrared Camera and Multi-Object Spectrometer (NICMOS) instrument aboard HST has been operating since 1997 in the wavelength range 0.8 – 2.5 μm . Among many other capabilities, it provides an imaging mode with a pixel scale of $0''.075 \text{ pixel}^{-1}$ and a coronagraphic mirror hole of radius 0.3 arcsec (Barker et al. 2007). With a combination of the coronagraphic mode and psf-subtraction techniques, contrast ratios of about 1×10^6 can be achieved at an angular distance of about 1 arcsec from the central star. Figure 3.4d demonstrates the coronagraphic capabilities available from NICMOS. Disk structure is clearly resolved. Because of this capability, a proposal has been submitted (March 2008) for NICMOS observations of several T Tauri and Herbig Ae/Be stars, including HD 100453. If this proposal is accepted, it is likely that disk structure will be resolved for the first time around many of the targets.

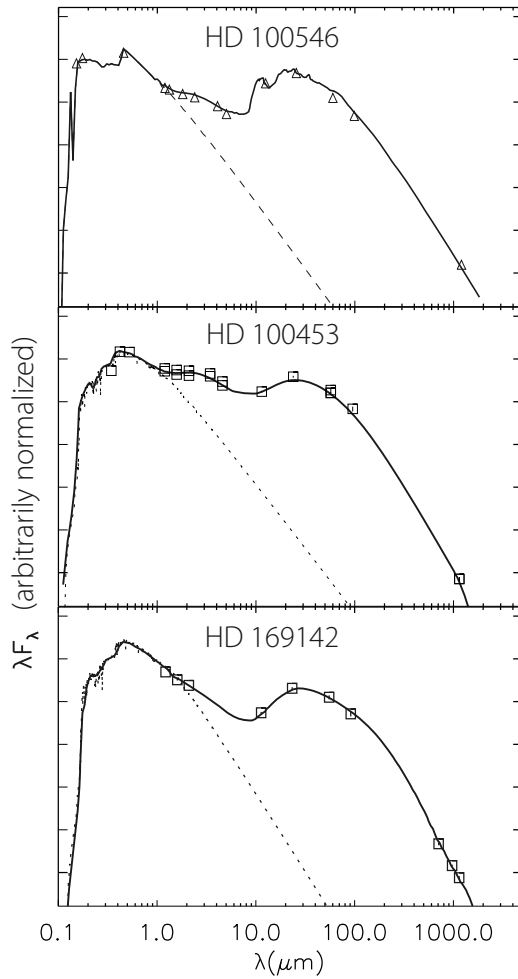


Figure 3.3. SEDs of HD 100546, HD 100453, and HD 169142.

The solid lines show the SED continuum fit to the photometric data indicated by the circles and squares. The stellar contribution is indicated by the Kurucz (1991) models shown as dashed lines. The strong mid-IR blackbody component common to all three SEDs is likely caused by a gap in each of the disk structures (see text). The NIR component of HD 100564 (top panel) and HD 100453 (middle panel) is strong and is likely the result of vertical extension in the inner disk structure (see text). The NIR excess of HD 169142 (bottom panel) is weak and suggests a geometrically thin inner disk (top panel – after Bouwman et al. 2003; middle panel – after figure from M. Sitko, private communication; bottom panel – after Grady et al. 2007).

HST: HD 141569

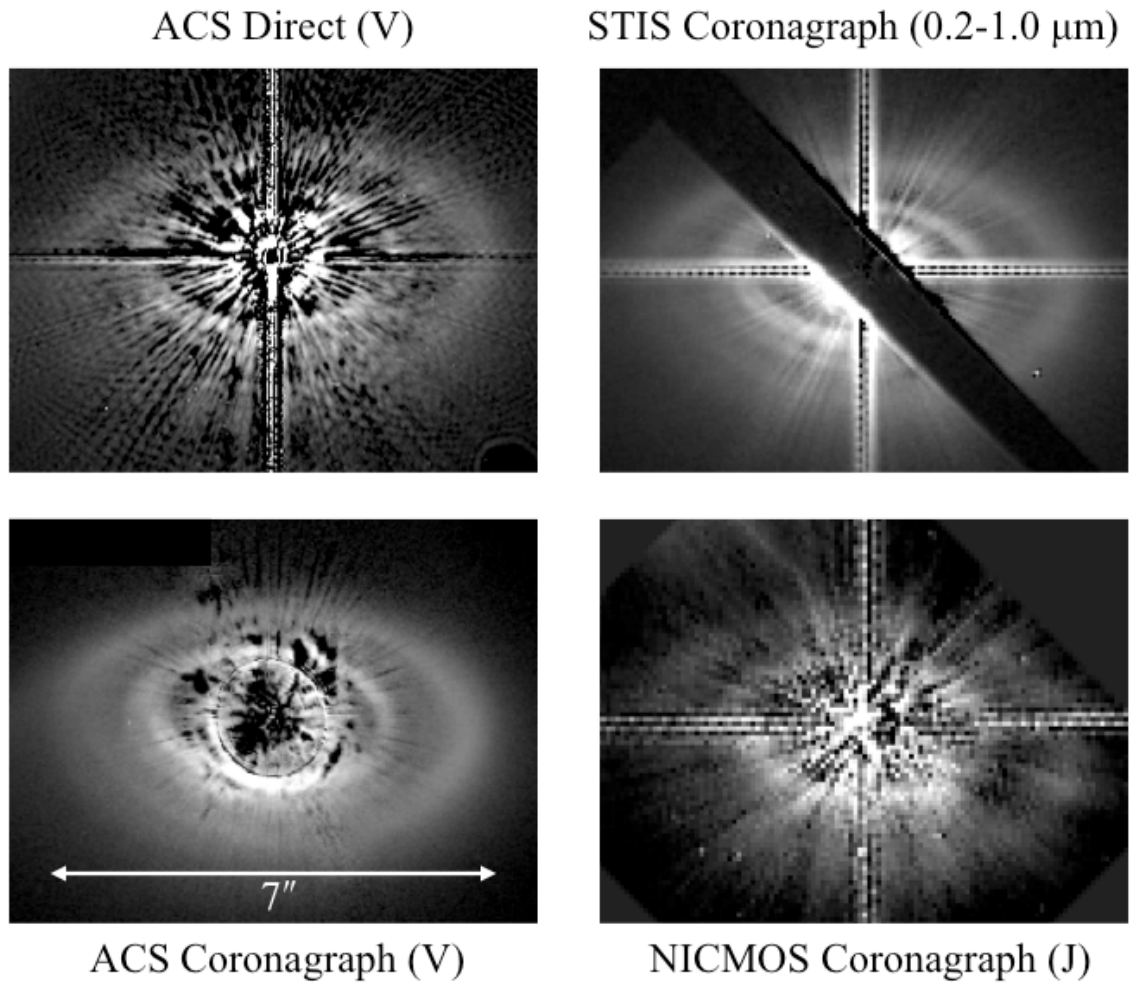


Figure 3.4. HST coronagraphic capabilities of ACS, STIS, and NICMOS.

Images of HD 141569 from three HST instruments with high contrast, high resolution coronagraphic capability (from Krist 2004). Structure in the disk is clearly resolved.

- (a) An ACS psf-subtracted direct image of HD 141569 in V-band.
- (b) A STIS psf-subtracted coronagraphic image of HD 141569 at 0.2 – 1.0 μm .
- (c) An ACS psf-subtracted coronagraphic image of HD 141569 in V-band.
- (d) A NICMOS psf-subtracted coronagraphic image of HD 141569 in J-band.

3.3.2 ACS and STIS on HST

The most important near-term space instrumentation advance is the Hubble Space Telescope servicing mission 4 (SM4), which is scheduled for August 2008. Recall that the coronagraphic imagery in this work was obtained by the HST ACS HRC camera. However, since June 2006, the HRC camera has been out of service due to a power supply failure. SM4 will repair ACS and restore its high contrast, high spatial resolution imaging capability that is key to resolving disk structure around young stars (Figure 3.4a,c). It provides circular coronagraphic spots of radius $0''.9$ and $1''.8$, a pixel scale of $0''.025 \text{ pixel}^{-1}$, and with psf-subtraction can obtain a contrast ratio of 1×10^6 at an angular separation of $1''$ from the central star (Gonzaga et al. 2006).

The Space Telescope Imaging Spectrograph (STIS) is an HST instrument that failed in 2004. SM4 will also restore STIS to operational status. Although STIS is primarily a spectrograph, it also provides a coronagraphic imaging mode with a pixel scale of $0''.05 \text{ pixel}^{-1}$ (Figure 3.4b). Its occulters are crossed wedges ranging in width from $0.5 - 2.8 \text{ arcsec}$ (Kim Quijano et al. 2007). This occulter design is optimal for imaging disk structure around stars with close binaries.

The restoration of the high contrast, high spatial resolution, coronagraphic imaging capability of ACS and STIS will provide obvious opportunities to resolve disk structure around young stars.

3.3.3 Millimeter/Submillimeter Interferometry

Millimeter and submillimeter interferometers are offering exciting new capabilities to image disk structure at very high spatial resolutions. Because the interferometers operate in the sub-mm/mm wavelength range, they detect radiation from

cold material ($\sim 20 - 100$ K). Although much of the dust and gas in a circumstellar disk is cold and radiates significantly in the sub-mm/mm, stars have negligible emission at these wavelengths, and therefore coronagraphs are not required.

One such observatory in operation today is the Combined Array for Research in Millimeter-wave Astronomy (CARMA), which is located in eastern California. CARMA provides resolutions down to $0''.1$ at a wavelength of 1.3 mm. Another operating observatory is the Sub-Millimeter Array (SMA), which is an 8-element radio interferometer located atop Mauna Kea in Hawaii that operates at wavelengths from $330 \mu\text{m}$ to 1.6 mm and provides a spatial resolution of $0''.15$ at $435 \mu\text{m}$. Observations from these instruments provide data related to disk structure, gas mass, and dust mass.

3.3.4 Mid-IR Imaging and Spectroscopy

When heated by direct radiation from the central star, small warm dust grains emit thermal radiation in the mid-IR. Observations of this radiation allow one to trace the existence of small grains in a disk and to develop evolutionary constraints on grain growth in disks. Mid-IR atmospheric windows occur in the range of $10 \mu\text{m}$ and $20 \mu\text{m}$, allowing ground based observations at these wavelengths. Two classes of small grains found in circumstellar disks are polycyclic aromatic hydrocarbons (PAHs) and amorphous silicates, and both radiate in the $10 \mu\text{m}$ window at various wavelengths. If we can spatially resolve the emission, we can also extract disk structure information from the data. It is also important to point out that star-to-disk contrast ratios are significantly lower in the mid-IR than in the optical.

One of the best instruments to observe in the mid-IR is Canaricam on the 10.4 m Gran Telescopio Canarias located in the Canary Islands (Northern Hemisphere).

Canaricam²² offers both imaging and spectroscopic modes. Imaging mode has a pixel scale of $0''.08 \text{ pixel}^{-1}$ and a field of view of $19'' \times 26''$. It also offers a $0''.83$ radius coronagraph which can improve contrast by a factor of 10 at $1''$ from the central star. Spectroscopic mode offers a $19''$ long-slit that can be used to spatially resolve line features. Canaricam observations of a target could provide both disk structure and grain size information.

3.3.5 NICI on Gemini South

The Near-IR Coronagraphic Imager²³ (NICI) is a ground-based instrument and is currently being tested on the Gemini South 8.1 meter telescope (appropriately located for observations of HD 100453), and it is expected to be available as a general user instrument in 2009. NICI should provide the capability to image larger planets in the cavities of circumstellar disks at angular separations from the star of greater than ~ 1 arcsec. NICI uses an onboard adaptive optics system with an 85 element deformable mirror for sharpening the image, and a set of coronagraphic masks of radius 0.22, 0.32, 0.46, 0.65, and 0.90 arcsec to reduce light contamination from the central star. NICI has two imaging channels to simultaneously image the same field of view in two filters. The detectors have a field of view of $18''.4 \times 18''.4$, a pixel scale of $0''.018 \text{ pixel}^{-1}$, and a wavelength coverage of $0.9 - 5.5 \mu\text{m}$. NICI's baseline performance estimate assumes a contrast ratio of 15 magnitudes at 1.5 arcsec radius from the star (Figure 3.5), using differential imaging with 1% methane filters at $1.6 \mu\text{m}$ and traditional hard-edged pupil and focal plane masks.

²² <http://www.gtc.iac.es/en/pages/instrumentation.php>

²³ <http://www.gemini.edu/sciops/instruments/nici/>

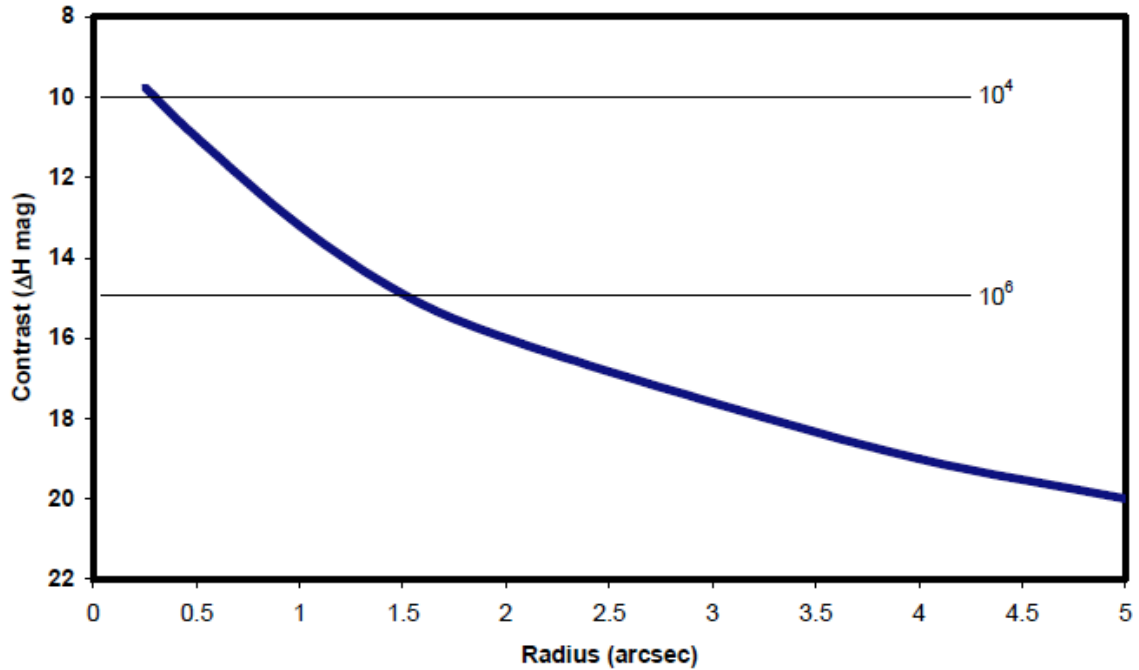


Figure 3.5. NICI estimated contrast ratio in H-band.

The blue curve indicates the expected contrast ratio that can be obtained as a function of angular distance from the central star (natural V-band seeing of ~ 0.5 arcsec, 3 hour exposure, 5σ significance). At 1.5 arcsec, a contrast ratio of 15 magnitudes (1×10^6) is expected. The horizontal black lines mark contrast ratios of 10^4 and 10^6 (from “*NICI RFP for Planet Finding Campaign*” issued 9/15/2005).

3.3.6 Atacama Large Millimeter Array (ALMA)

Perhaps one of the most powerful instruments on the horizon for circumstellar disk observations is ALMA. Operating in the millimeter/submillimeter wavelength range (0.3 – 9.6 mm), ALMA will provide the capability to image cold dust and gas at very high angular resolution. It will be composed of up to sixty-four 12-meter antennas, and will be located in the Chilean Andes at an altitude of 5000 meters. Construction is scheduled for completion in 2012. ALMA will provide the ability to image stellar

environments at spatial resolutions down to 0.01 arcsec (~ 1 AU resolution for HD 100453A). Because the central star is not bright at millimeter wavelengths, contrast issues are not a problem. With ALMA's high resolution imaging capability, one will be able to more accurately determine the size and mass of cold dust disks, the distribution and mass of cold gas, the inclination of the system, and resolve any cavities in the disk. Figure 3.6 illustrates a simulation of ALMA observations in the sub-mm. The inner disk, disk cavity, planet, and outer disk are clearly resolved.

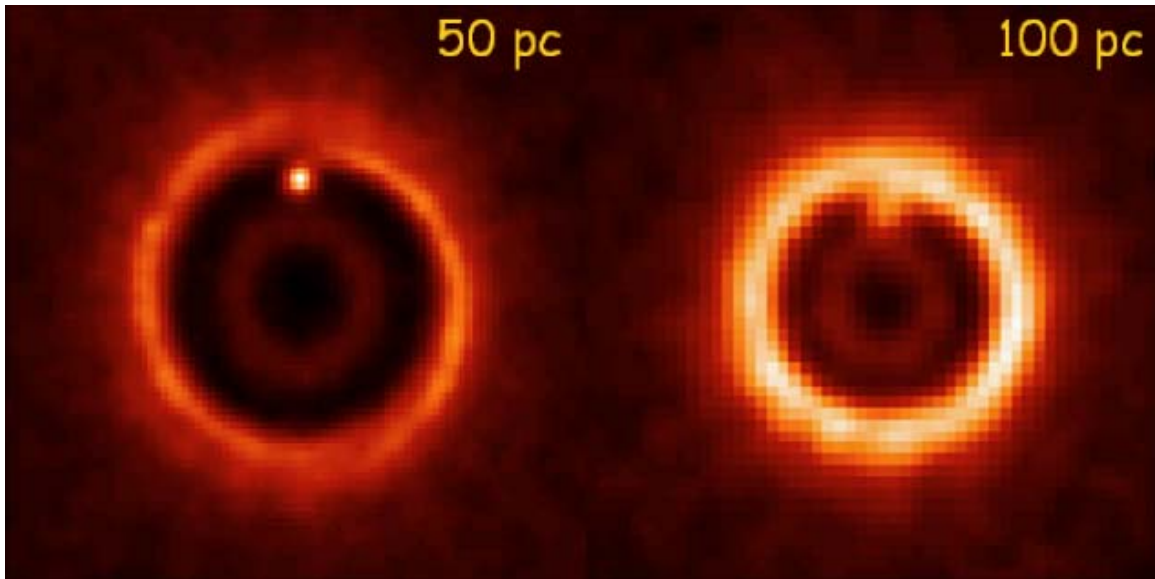


Figure 3.6. A simulation of ALMA observations at 950 GHz (310 μm).

A simulation of ALMA observations at 310 μm of a disk shows an embedded protoplanet of 1 Jupiter Mass around a 0.5 Solar Mass star (orbital radius: 5AU). The assumed distance is 50 pc or 100 pc as labeled. The disk mass is set to $M_{\text{disk}} = 1 \times 10^{-2} M_{\odot}$. Only structures above the 2σ level are shown (Wolf & D'Angelo 2005).

3.3.7 Space-based Missions

Several space-based observatories are in various stages of development or planning. One of these longer-term missions is the James Webb Space Telescope²⁴ (JWST), which is scheduled for launch in 2013. It is optimized for observations in the IR, and the primary camera, NIRSpec, operates in the range of 0.6 – 5 μm , with its incoming light split by a dichroic at $\sim 2.35 \mu\text{m}$. The short wavelength channel has a pixel scale of $0''.0317 \text{ pixel}^{-1}$, and the long wavelength channel has a pixel scale of $0''.0648 \text{ pixel}^{-1}$.

The Space Interferometry Mission²⁵ (SIM) is currently an unfunded NASA mission that will launch no earlier than 2015. The spacecraft would have the capability to measure the angular position of an object in space (astrometry) with a precision of $\sim 1 \times 10^{-6}$ arcsec. The main goal of SIM is to find planets orbiting stars by astrometric wobble: tiny changes in the position of a star that are created by an orbiting planet. SIM would also precisely determine the distance to stars in the Milky Way, which would help to place more stringent limits on the ages, masses, and luminosities of the young stars we are studying.

Two other missions under discussion are Terrestrial Planet Finder - Coronagraph²⁶ (TPF-C) and New Worlds Observer (NWO) (Arenberg & Cash 2005). Both seek to provide small inner working angles of $\sim 0''.05$ and a contrast ratio of at least 1×10^{10} , which is the minimum requirement to image a terrestrial mass planet around a nearby solar mass star, in the optical. NWO proposes a separate spacecraft from the

²⁴ <http://www.stsci.edu/jwst/>

²⁵ http://planetquest.jpl.nasa.gov/SIM/sim_index.cfm

²⁶ http://planetquest.jpl.nasa.gov/TPF-C/tpf-C_index.cfm

telescope spacecraft which acts as a detached occulter and flies at a distance of about 50,000 km from the telescope. TPF-C attempts to achieve the goal within a single spacecraft by utilizing a coronagraph, adaptive optics, a series of images taken at different spacecraft roll angles, and sophisticated image processing.

Although it is not possible to predict which, if any, of these proposed missions will be funded to completion, instrumentation available today has the capabilities and can be utilized to help us understand circumstellar disk evolution and the origins of our own solar system. We are living in a very exciting epoch of astrophysical discoveries that are redefining our understanding of the origins and fate of the universe, the Milky Way galaxy, the solar system, the planet Earth, and the life existing around us.

REFERENCES

- Acke, B., & Waelkens, C. 2004, *A&A*, 427, 1009
- Acke, B., van den Ancker, M. E., & Dullemond, C. P. 2005, *A&A*, 436, 209
- Alcala, J. M., et al. 1993, *A&A*, 272, 225
- Alexander, R. D., Clarke, C. J., Pringle, J. E. 2006, *MNRAS*, 369, 229
- Andrews, S. M., & Williams, J. P. 2005, *ApJ*, 631, 1134
- Arenberg, J. & Cash, W. 2005, IUE Symposium, “*New Worlds Observer: A novel Planet Finding Mission*”
- Artymowicz, P., & Lubow, S. H. 1994, *ApJ*, 421, 651
- Baraffe, I., Charbrier, G., Allard, F., & Hauschildt, P. H. 1998, *A&A*, 337, 403.
- Barker, E., Dahlen, T., et al. 2007, “NICMOS Instrument Handbook”, Version 10.0, (Baltimore: STScI)
- Bastian, U., et al. 1983, *A&A*, 126, 438
- Beckwith, S. V. W., Sargent, A. I., Chini, R. S., & Guesten, R. 1990, *AJ*, 99, 924
- Bessell, M. S., & Brett, J. M. 1988, *PASP*, 100, 1134
- Bohlin, R., Hartig, G., Meurer, G. 1999, Flats: SBC Data From Thermal Vacuum Testing, ISR ACS 99-02
- Bohlin, R. C. 2007, Instrument Science Report ACS 2007-06; Baltimore:STScI
- Bonnet, H. et al. 2004, *The ESO Messenger* 117, 17
- Bouwman, J., de Koter, A., Dominik, C., & Waters, L. B. F. M. 2003, *A&A*, 401, 577
- Brittain, S. D. 2004, Ph.D. Thesis
- Brittain, S. D., Rettig, T. W., Simon, T., Kulesa, C., DiSanti, M. A., & Dello Russo, N. 2003, *ApJ*, 588, 535

- Brittain, S. D., Simon, T., Najita, J. R., & Rettig, T. W. 2007, *ApJ*, 659, 685
- Calvet, N., Muzerolle, J., Briceno, C., Hernandez, J., Hartmann, L., Saucedo, J. L., & Gordon, K.D. 2004, *AJ* 128, 1294.
- Carmona, A., van den Ancker, M. E., & Henning, T. 2007, *A&A*, 464, 687
- Carmona, A., et al. 2008, *A&A*, 477, 839
- Chen, X. P., Henning, T., van Boekel, R., & Grady, C. A. 2006, *A&A*, 445, 331
- Chiang E. I., & Goldreich P. 1997, *ApJ*, 490, 368
- Clampin, M. et al. 2003, *AJ*, 126, 385
- Clarke, C. J., Gendrin, A., Sotomayor, M. 2001, *MNRAS*, 328, 485
- Collins, K. A. et al. 2007, Instrument Science Report (ACS 07-05; Baltimore:STScI)
- Coulson, I. M., Walther, D. M., & Dent, W. R. F. 1998, *MNRAS*, 296, 934
- Cox, Arthur N. et al. 2001, *Allen's Astrophysical Quantities* (4th ed, 2nd printing; NY, Springer)
- Cox, C. 2004, SBC Dark and Cumulative Images, ISR ACS 2004-014
- Cutri, R. M., et al. 2003, 2Mass All-Sky Point Sources Catalog,
<http://irsa.ipac.caltech.edu/applications/Gator/>
- D'Alessio, P., Merín, B., Calvet, N., Hartmann, L., & Montesinos, B. 2005, *Rev. Mex. AA*, 41, 61
- Dent, W. R. F., et al. 2000, *Imaging at Radio through Submillimeter Wavelengths*, ASP Conference Series, Vol 217, p. 33
- Dent, W. R. F., Greaves, J. S., & Coulson, I. M. 2005, *MNRAS*, 359, 663
- Devine, D., Grady, C. A., Kimble, R. A., Woodgate, B., Bruhweiler, F. C., Boggess, A., Linsky, J. L., & Clampin, M. 2000, *ApJ* 542, L115
- Disanti, M. A., Mumma, M. J., Dello Russo, N., & Magee-Sauer, K. 2001, *Icarus*, 153, 361
- Dominik, C., Dullemond, C. P., Waters, L. B. F. M., & Walch, S. 2003, *A&A*, 398, 607
- Dullemond, C. P., Hollenbach, D., Kamp, I., & D'Alessio, P. 2006, *Protostars and Planets V*, Reipurth, B., Jewitt, D., & Keil K. Eds., University of Arizona Press, Tucson

- Eisenhauer, F. et al. 2003, SPIE 4841, 1548
- Endres, M., Haddad, N., Hilton, G. M., Grady, C. A., Woodgate, B. E., & Williger, G. M. 2005, BAAS, 37, 1287
- Feigelson, E. D., Gaffney, J. A., Garmire, G., Hillenbrand, L. A., & Townsley, L. 2003, ApJ, 584, 911
- Feigelson, E. D., Lawson, W. A., Stark, M., Townsley, L., & Garmire, G. P. 2006, AJ, 131, 1730
- Finkenzeller, U., & Mundt, R. 1984, A&AS, 55,109
- Fukagawa, M., et al. 2006, ApJ, 636, L153
- Garcia Lopez, R., Natta, A., Testi, L., & Habart, E. 2006, A&A, 459, 837
- Garmire, G. P., Bautz, M. W., Ford, P. G., Nousek, J. A., & Ricker, G. R. Jr. 2003 SPIE 4851, 28
- Gizis, J. E. 2002, ApJ, 575, 484
- Gizis, J. E., Shipman, H. L., & Harvin, J. A. 2005, ApJ, 630, 89
- Goldreich P., & Ward W. R. 1973, ApJ, 183, 1051
- Golimowski, D. A. et al. 2006, AJ, 131, 3109
- Gonzaga, S. et al. 2005, <http://www.stsci.edu/hst/acs/proposing/dither/ACS-SBC-DITHER-BOX.html>
- Gonzaga, S. et al. 2006, ACS Instrument Handbook, V. 6.0, (Baltimore:STScI).
- Grady, C. A., et al. 2004, ApJ, 608, 809
- Grady, C. A., Woodgate, B., Heap, S. R., et al. 2005, ApJ, 620, 470
- Grady, C. A., et al. 2006, AAS, 210.8712
- Grady, C. A., et al. 2007, ApJ, 665, 1391
- Habart, E., Natta, A., & Krügel, E. 2004, A&A, 427, 179
- Habart, E., Natta, A., Testi, L., & Carillet, M. 2006, A&A, 449, 1067
- Habing, H. J. et al. 2001, A&A, 365, 545
- Hamaguchi, K., Yamauchi, S., & Koyama, K. 2005, ApJ, 618, 360

- Hamann, F., & Persson, S. E. 1992, ApJS, 82, 285
- Harper, G. M., Wilkinson, E., Brown, A., Jordan, C., & Linsky, J. L. 2001, ApJ, 551, 486
- Hartmann, L. 2005, in “The Nature and Evolution of Disks Around Hot Stars”, ASP Conf. Ser. 337, (eds. Ignace, R., and Gayley, K. G.), 3.
- Hempel, M., Robrade, J., Ness, J. U., & Schmitt, J. H. M. M. 2005, A&A, 440, 727
- Herbig, G. H. 1960, ApJS, 4, 337
- Hinkle, K. H., et al. 2003, ProcSPIE, 4834, 353
- Hinkle, K. H., Joyce, R. R., Sharp, N., & Valenti, J. A. 2000, ProcSPIE, 4008, 720
- Hinkle, K. H., Cuberly, R. W., Gaughan, N. A., Heynssens, J. B., Joyce, R. R., Ridgway, S. T., Schmitt, P., & Simmons, J. E. 1998, ProcSPIE, 3354, 810
- Houk, N. & Cowley, A. P. 1975, Michigan Catalogue of two-dimensional spectral types for the HD star
- Isella, A. 2006, PhD Thesis, “Interferometric Observations of Pre-main Sequence Disks”
- Johnson, H. L. et al. 1966, CoLPL, 4, 99
- Joy, A. H. 1945, ApJ 102, 168
- Kaufer, A. et al. 1999, The Messenger 95, 8
- Kaufer, A., Stahl, O., Tubbesing, S., Norregaard, P., Avila, G., Francois, P., Pasquini, L., & Pizzella, A. 2000, SPIE, 4008, 459
- Kenyon S. J. & Hartmann L. 1987 ApJ, 323, 714
- Kenyon, S. J. & Hartmann, L. 1995, ApJS, 101, 117
- Kim Quijano, J., et al. 2007, "STIS Instrument Handbook", Version 8.0, (Baltimore: STScI)
- Kouwenhoven, M. B. N., Brown, A. G. A., Zinnecker, H., Kaper, L., & Portegies Zwart, S. F. 2005, A&A, 430, 137
- Krist, J. E. 2004, workshop, “*Hubble Space Telescope Coronagraphs*”
- Krist, J. E. et al. 2005, AJ, 129, 1008
- Laidler et al, 2007, "Synphot Data User's Guide" (Baltimore, STScI)
- Lahuis, F. et al. 2007, ApJ, 665, 492

- Lagrange, A. M. et al. 2003, SPIE, 4841, 860
- Lenzen, R. et al. 1998, SPIE, 3354, 606
- Lenzen, R. et al. 2003, SPIE, 4841,944
- Li, J., Kastner, J. H., Prigozhin, G. Y., & Schulz, N. S. 2003, ApJ, 590, 586
- Li, J., Kastner, J. H., Prigozhin, G. Y., Schulz, N. S., Feigelson, E. D., & Getman, K. V. 2004, ApJ, 610, 1204
- Liu, W. M., Hinz, P. M., Meyer, M. R., et al. 2003, ApJ, 598, L111
- Malfait, K., Bogaert E., & Waelkens, C. 1998, A&A, 331, 211
- Mamajek, Eric E., Meyer, Michael R., & Liebert, James 2002, AJ, 124, 1670
- Manoj, P., Bhatt, H. C., Maheswar, G., & Muneer, S. 2006, ApJ, 653, 657
- Meeus, G., Waters, L. B. F. M., Bouwman, J., van den Ancker, M. E., Waelkens, C., & Malfait, K. 2001, A&A, 365, 476
- Meeus, G., Bouwman, J., Dominik, C., Waters, L. B. F. M., & de Koter, A. 2002, A&A, 392, 1039
- Meeus, G., Bouwman, J., Dominik, C., Waters, L. B. F. M., & de Koter, A. 2003, A&A, 402, 767
- Modigliani, A., Ballester, P., & Peron, M. 2007, VLT-MAN-ESO-19500-3600
- Mohanty, S., Basri, G., & Jayawardhana, R. 2005, AN, 326, 891
- Mutchler M. et al. 2004, Bias and Dark Calibration of ACS Data, ISR ACS 2004-07
- Muzerolle, J., Hartmann, L., & Calvet, N. 1998, ApJ, 492, 743
- Najita, J. R., Strom, S. E., & Muzerolle, J. 2007, MNRAS, 378, 369
- Natta, A. & Whitney, B. A. 2000, A&A, 364, 633
- Pavlovsky, C., et al. 2006a, ACS Data Handbook, Version 5.0, (Baltimore: STScI)
- Pavlovsky, C. et al. 2006b, "ACS Instrument Handbook", Version 7.0, (Baltimore: STScI)
- Persson, S. E., Murphy, D. C., Krzeminski, W., Roth M., and Rieke, M. J. 1998, AJ, 116, 2475
- Phillips, J. P. 1999, A&AS 134, 241

- Roberge, A. et al. 2001, ApJ, 551L, 97
- Rousset, G., et al. 2003, SPIE, 4839, 140
- Rayner et al. in prep
- Perryman, M. A. C. et al. 1997, A&A, 323, L49
- Ryter, C. E. 1996, Ap&SS, 236, 285
- Sasseen, T. P., Hurwitz, M., Dixon, W. V., & Airieau, S. 2002, ApJ, 566, 267
- Scoville, N. Z., Sargent, A. I., Sanders, D. B., Claussen, M. J., Masson, C. R., Lo, K. Y., & Phillips, T. G. 1986, ApJ, 303, 416
- Setiawan, J., Henning, Th., Launhardt, R., Müller, A., Weise, P., & Kürster, M. 2008, Nature, 451, 38
- Shu, F. H., Adams, F. C., & Lizano, S. 1987, ARA&A, 25, 23
- Siess L., Dufour E., Forestini M. 2000, A&A, 358, 593
- Skinner, S. L., Güdel, M., Audard, M., & Smith, K. 2004, ApJ, 614, 221
- Stauffer, J. R. 2004, Debris Disks and the Formation of Planets, 324, 100
- Stecklum, B., Grady, C. A., Bouret, J. C., Endres, M., Meusinger, H., Roberge, A., Sahu, M., Williger, G. M., & Woodgate, B. 2007, A&A (in press).
- Stelzer, B., Micela, G., Flaccomio, E., Neuhäuser, R., & Jayawardhana, R. 2006a, A&A, 448, 293
- Stelzer, B., Micela, G., Hamaguchi, K., & Schmitt, J. H. M. M. 2006b, A&A, 457, 223
- Strom, K. E., Strom, S. E., Edwards, S., Cabrit, S., & Skrutskie, M. F. 1989, AJ, 97, 1451
- Skrutskie, M. F., Dutkevitch, D., Strom, S. E., Edwards, S., Strom, K. M., Shure, M. A., 1990, AJ, 99, 1187
- Swartz, D. A., et al. 2005, ApJ, 628, 811
- Tsuboi, Y., 2003, ApJ, 587, 51
- Tsunemi, H., Mori, K., Miyata, E., Baluta, C., Burrows, D. N., Garmire, G. P., & Chartas, G. 2001, ApJ, 554, 496
- van Boekel, R. et al. 2005, A&A, 437, 189

- van den Ancker, M. E. 1999, PhD Thesis, "Circumstellar Material in Young Stellar Objects"
- Vieira, S. L. A. et al. 2003, *ApJ*, 126, 2971
- Wade, G A., Bagnulo, S., Drouin, D., Landstreet, J. D., & Monin, D. 2007, *MNRAS*, 376, 1145
- Wassell, E. J., Grady, C. A., Woodgate, B., Kimble, R. A., Bruhweiler, F. C. 2006, *ApJ*, 650, 985
- Weidenschilling, S. J. 1997, *Icarus*, 127, 290
- Weinberger, A. J., Rich, R. M., Becklin, E. E., Zuckerman, B., & Matthews, K. 2000, *ApJ*, 544, 937
- Wisniewski, J. P. et al. 2008, *ApJ*, submitted
- Wood, J.A. 1997, *Sky & Telescope* 97, No. 1, 37
- Wolf, S. & D'Angelo, G. 2005, *ApJ*, 619, 114
- Youdin, A. N., & Shu, F. H. 2002, *ApJ*, 580, 494
- Zuckerman, B., & Becklin, E. E. 1993, *ApJ*, 414, 793
- Zuckerman, B. 2001, *ARA&A*, 39, 549
- Zuckerman, B., & Song, I. 2004, *ARA&A*, 42, 685

APPENDIX

A. AN OPTICAL GHOST IN HST/ACS/SBC F122M

A.1 Introduction

HST has been used to find low-mass stellar, sub-stellar, and planetary mass companions to pre-main sequence stars by exploiting its diffraction limited imaging and large dynamic range. We have extended this into the FUV using the Advanced Camera for Surveys (ACS) Solar Blind Channel (SBC). Low-mass companions to Herbig Ae stars are expected to be copious X-ray emitters, and to have strong emission at $H\alpha$ and Lyman α . With its diffraction limited imaging, HST is capable of locating chromospherically-active counterparts to X-ray sources with a factor of 20 improvement in spatial resolution over Chandra, and can detect such sources in close proximity to Herbig Ae stars (Grady et al. 2007). Our criterion is that we should see X-ray, $H\alpha$, and Lyman α emissions for a real object. However, in analyzing our datasets, we have found features in the SBC F122 Lyman α imagery that do not exist in corresponding X-ray imagery or Near IR imagery.

A.2 Observations

A.2.1 Program Star Observations

HD 169142 and HD 100453 were observed with HST and the Advanced Camera for Surveys Solar Blind Channel with the F122M filter (nominal $\lambda_{\text{eff}} = 1210\text{\AA}$, FWHM = 60\AA) on 2006 April 5 and 2006 June 7, respectively, as part of HST-GO-10764 (Grady, PI). The HD 169142 data, with total integration time of 1904 s, were

obtained in 4 segments within a single spacecraft orbit at a spacecraft orientation of 88.6789° (see Table A.1). The HD 100453 data, with total integration time of 2096 s, were also obtained in 4 segments within a single spacecraft orbit at a spacecraft orientation of -82.0755° (see Table A.1). For each segment of both targets, the field was dithered using ACS small-box dither pattern (Gonzaga et al. 2005, with dither offsets of $\approx 0''.15-0''.19$) about the SBC aperture location.

A.2.2 Archival Observations

The known single source white dwarf reference star HS 2027+0651 was observed with HST/ACS/SBC/F122M on 2002 June 9 as part of calibration program 9020 (De Marchi, PI). One exposure of 400 seconds was obtained with a spacecraft orientation of 59.9797° East of North (see Table A.1).

HS 2027+0651 was again observed with HST/ACS/SBC/F122M on 2003 March 19 as part of calibration program 9654 (De Marchi, PI). The data, with a total integration time of 2000 s, were obtained in 5 segments within a single spacecraft orbit at a spacecraft orientation of 96.3855° East of North (see Table A.1). For each segment, the field was dithered using ACS small-box dither pattern (Gonzaga et al. 2005, with dither offsets of $\approx 0''.15-0''.19$) about the SBC aperture location.

A.3 Data Reduction

The data were processed using the default ACS pipeline software (NOAO-IRAF FITS Image Kernel July 2003) including geometric distortion correction and the use of the multi-drizzle algorithm to produce a stacked (except for the 2002 June 9 HS 2027+0651 single exposure observation), geometric distortion corrected image

(Pavlovsky et al. 2006b). In the final, geometrically corrected imagery, the scale is $0''.025 \text{ pixel}^{-1}$.

A.3.1 Known ACS/SBC Anomalies

Each of the above referenced datasets readily demonstrates two known SBC MAMA detector anomalies (Bohlin et al. 1999; Cox 2004; Mutchler et al. 2004). In each image, a set of warm pixels is seen near physical location $x = 80, y = 341$. Also, a known bad MAMA detector anode can be detected starting at $x = 0, y = 718$ and progressing slightly upward (due to the geometric correction) and to the right across the detector frame. Both sets of coordinates are relative to the geometric distortion corrected, multi-drizzle imagery.

Table A.1

Summary of Ghost Observations (HST/ACS/SBC F122M)

Target	Program ID	Observation ID	Exposure Date	Exposure Start Time	Exposure Duration (sec)	Spacecraft Orientation (E of N)
HS 2027+0651	9020	j8c102wnq_drz.fits	6/9/02	08:27	400	59.9797°
HS 2027+0651	9654	j8jq01ryq_drz.fits	3/19/03	14:15	400	96.3855°
	9654	j8jq01rzq_drz.fits	3/19/03	14:23	400	96.3855°
	9654	j8jq01s0q_drz.fits	3/19/03	14:30	400	96.3855°
	9654	j8jq01s1q_drz.fits	3/19/03	14:37	400	96.3855°
	9654	j8jq01s2q_drz.fits	3/19/03	14:45	400	96.3855°
HD 169142	10764	j9jd02010_drz.fits	4/5/06	09:14	476	88.6789°
	10764	j9jd02020_drz.fits	4/5/06	09:26	476	88.6789°
	10764	j9jd02030_drz.fits	4/5/06	09:37	476	88.6789°
	10764	j9jd02040_drz.fits	4/5/06	09:49	476	88.6789°
HD 100453	10764	j9jd01010_drz.fits	6/7/06	21:12	524	-82.0755°
	10764	j9jd01020_drz.fits	6/7/06	21:36	524	-82.0755°
	10764	j9jd01030_drz.fits	6/7/06	21:49	524	-82.0755°
	10764	j9jd01040_drz.fits	6/7/06	22:02	524	-82.0755°

A.4 Analysis

A.4.1 Identification of an Optical Ghost

As expected, all of the imagery is sparse in the field around the target, especially compared to NIR imagery (Grady et al. 2007). In the ACS HD 169142 imagery, we recover the companions of HD 169142 seen in NICMOS coronagraphic imagery (Grady et al. 2007). In addition, we have a surplus source that has no counterpart in Apache Point 3.5 meter/Goddard Fabry-Perot Interferometer H α imagery, NICMOS F110W coronagraphic imagery, or Chandra ACIS-S X-ray imagery (Grady et al. 2007).

Next we examine the ACS HD 100453 imagery and also find a surplus source at the exact same offset and position angle (PA) as found with the HD 169142 imagery. The surplus source in the ACS HD 100453 imagery has no counterpart in VLT NACO imagery (Chen et al. 2006), ACS HRC F606W coronagraphic imagery (this work), or Chandra ACIS-S X-ray imagery (this work). We now have two images of unrelated parts of the sky with a surplus source at the exact same PA and offset from the target, and we have imagery at other wavelengths in other instruments that do not exhibit the surplus source. This suggests a possible optical artifact associated with the ACS SBC instrument.

Finally, we test the hypothesis through the use of the ACS SBC F122M white dwarf (HS 2027+0651) calibration archival data listed in Table A.1. The data are taken at two different epochs and are at two different spacecraft orientations. The surplus source is again detected and exists at the same PA and offset from the primary target in both sets of imagery and in the HD 169142 and HD 100453 imagery. We now have the exact same target at two different spacecraft roll angles with the surplus source maintaining the same PA and offset from the primary target relative to the detector frame.

A.4.2 Characterization of the Ghost

With the surplus source being detected at the same PA and offset from the primary target in three unrelated parts of the sky, four different epochs, four different spacecraft orientations, and not seen at other wavelengths in other instruments, we conclude that the surplus source is not fixed on the sky or the detector frame and is therefore indeed an optical artifact.

In all of the datasets listed in Table A.1, the optical ghost appears at 19 degrees to the left of the positive y-axis in the geometrically corrected detector frame image (see Figure A.1). The edge of the ghost nearest the primary target is located from 3".93 to 4".36 from the peak of the primary target and its outer edge is located from 4".43 to 4".52 from the peak of the primary target. The SBC pixel scale is 0".025 pixel⁻¹ in the geometrically corrected drizzle datasets. The outer edge variations are only 20% of the inner edge variations and are all within the margin of error in determining the peak of the primary and the edge of the surplus source. The primary target to surplus source encircled energy ratio ranges from 169:1 to 94:1, with a mean value of 122:1 corresponding to an optical ghost containing 0.82% of the primary target energy (see Table A.2).

A.5 Discussion

The SBC MAMA detector is a STIS flight spare and STIS has a ghost that is visible in deep, far UV observations (Grady et al. 2004). However the SBC optical path design is somewhat different than the STIS optical path and as it turns out, the source of the SBC ghost is different than for STIS. Investigations into the SBC design (G. Hartig, private communication) suggest that the ghost is consistent with a reflection between the back and front sides of the F122M filter. The ACS SBC design counters the lateral color

induced by use of the STIS spare MAMA detector (window at ~24 deg angle of incidence) by tilting the filters in the opposite direction by a similar amount. The observed ghosts are in the direction expected from the filter back to front reflection mechanism, and their displacement from the star image is reasonable for the geometry (filter thickness ~3.6 mm). Furthermore, the variation in the distance to the nearest edge and the elongation of the ghost is consistent with the variation in refractive index of the filter substrate over its passband.

Optical ghosts are seen in other SBC filters as well. For further information go to http://www.stsci.edu/hst/acs/performance/anomalies/acs_sbc_opticalghosts.html at the STScI website.

Table A.2

Summary of Optical Ghost Results

Target	Dataset	Primary to Ghost Encircled Energy Ratio	Ghost Angular Position (left of +y-axis)	Ghost Distance From Peak of Primary Target		Ghost Radial Extent
				Near Edge	Far Edge	
HS2027+0651	j8c102wnq_drz.fits	115:1	19°	4.05"	4.48"	0.43"
HS2027+0651	j8jq01ryq_drz.fits	110:1	19°	3.93"	4.43"	0.50"
	j8jq01rzq_drz.fits					
	j8jq01s0q_drz.fits					
	j8jq01s1q_drz.fits					
HD169142	j8jq01s2q_drz.fits	94:1	19°	4.25"	4.51"	0.26"
	j9jd02010_drz.fits					
	j9jd02020_drz.fits					
	j9jd02030_drz.fits					
HD100453	j9jd02040_drz.fits	169:1	19°	4.36"	4.52"	0.16"
	j9jd01010_drz.fits					
	j9jd01020_drz.fits					
	j9jd01030_drz.fits					
Mean Value		122:1	19°	4.15"	4.49"	0.34"

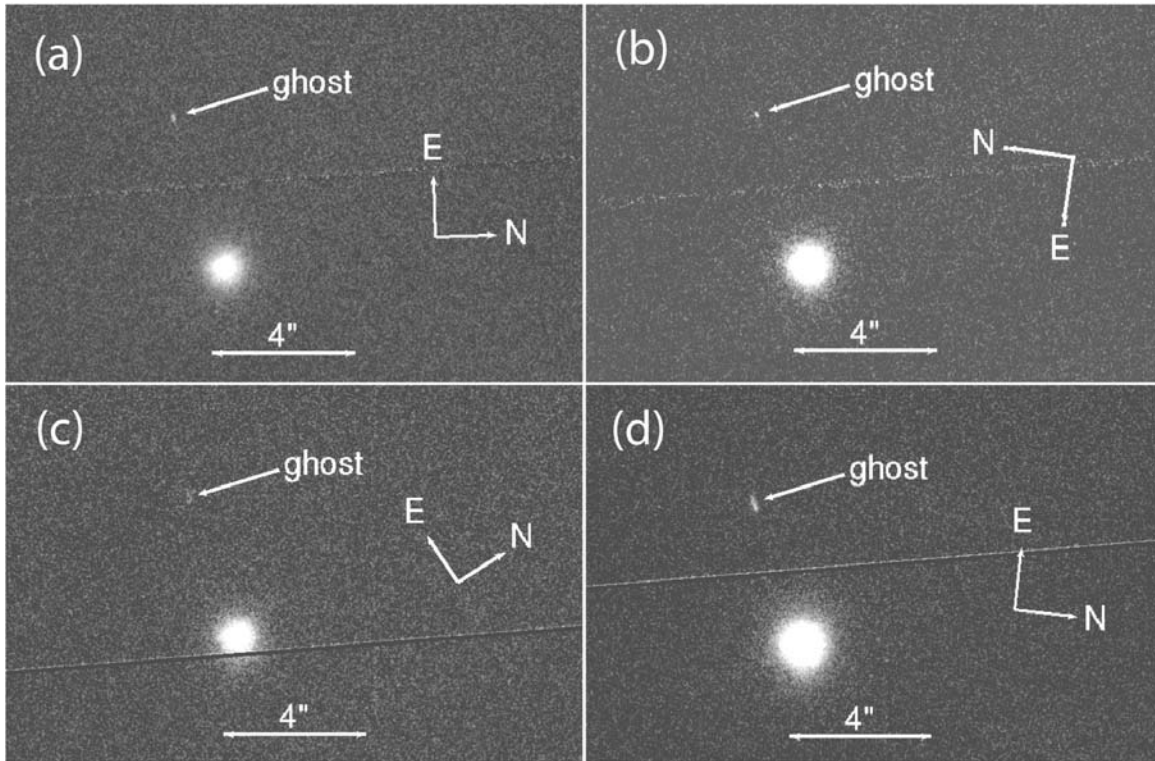


Figure A.1. Optical ghost imagery.

(a) HD 169142 – Four 476 second stacked exposures taken 2006 April 5.

(b) HD 100453 – Four 524-second stacked exposure taken 2006 June 7.

(c) HS 2027+0651 – Single 400-second exposure taken 2002 June 9.

(d) HS 2027+0651 – Five 400-second stacked exposures taken 2003 March 19.

GLOSSARY OF ACRONYMS

2MASS - Two Micron All-Sky Survey

ACIS-S - AXAF CCD Imaging Spectrometer - Spectroscopy

ACS - Advanced Camera for Surveys

A/O - Adaptive Optics

AU - Astronomical Unit

BPMG - Beta Pictoris Moving Group

CCD - Charge-Coupled Device

CIAO - Chandra Interactive Analysis of Observations

CXO - Chandra X-ray Observatory

ESA - European Space Agency

ESO - European Southern Observatory

ETC - Exposure Time Calculator

EW - Equivalent Width

FEROS - Fiber-fed Extended Range Optical Spectrograph

FIR - Far InfraRed

FITS - Flexible Image Transport System

FOV - Field Of View

FUSE - Far Ultraviolet Spectroscopic Explorer

FUV - Far UltraViolet

FWHM - Full Width Half Maximum

GFP - Goddard Fabry-Perot

GO - Guest Observer

GSFC - Goddard Space Flight Center

HARP - Heterodyne Array Receiver Program

HD - Henry Draper star catalogue

HH - Herbig-Haro

HIP - HIPparcos

H-R - Hertzsprung-Russell

HRC - High Resolution Channel

HST - Hubble Space Telescope

IR - Infrared

IRAS - Infrared Astronomical Satellite

IRAF - Image Reduction and Analysis Facility

IRS - Infrared Spectrograph

IRTF - InfraRed Telescope Facility

ISM - InterStellar Medium

ISO - Infrared Space Observatory

IUE - International Ultraviolet Explorer

JCMT - James Clerk Maxwell Telescope

K - Kelvin

keV - kiloelectronVolt

KSGC - Kentucky Space Grant Consortium

LCCA - Lower Centaurus Crux Association

MIR - Mid-InfraRed

M_{\odot} - Solar Mass

MAMA - MultiAnode Microchannel Array

M_J - Jupiter Mass

Myr - Million year(s)

NACO - Short for NAOS Conica

NAOS - Nasmyth Adaptive Optics System

NASA - National Aeronautics and Space Administration

NICMOS - Near Infrared Camera and Multi-Object Spectrometer

NOAO - National Optical Astronomy Observatory

NSF - National Science Foundation

NIR - Near-InfraRed

PA - Position Angle

PAH - Polycyclic Aromatic Hydrocarbons

pc - parsec

PI - Primary Investigator

PM - Proper Motion

psf - point spread function

PMS - Pre-Main Sequence

RASS - ROSAT All-Sky Survey

ROSAT - RÖntgen SATellite

SAO - Smithsonian Astrophysical Observatory

SBC - Solar Blind Channel

SED - Spectral Energy Distribution

SER - Sub-pixel Event Repositioning

SINFONI - Spectrograph for INtegral Field Observations in the Near Infrared

SNR - Signal-to-Noise Ratio

STIS - Space Telescope Imaging Spectrograph

STScI - Space Telescope Science Institute

SYNPHOT - SYNthetic PHOTometry software

SWS - Short Wavelength Spectrometer

UV - Ultraviolet

VLT - Very Large Telescope

ZAMS - Zero Age Main Sequence

CURRICULUM VITAE

NAME: Karen Alicia Collins

ADDRESS: Department of Physics and Astronomy
102 Natural Science Building
University of Louisville
Louisville, KY 40292

DOB: May 22, 1962

EDUCATION: B.S. Electrical Engineering
Georgia Institute of Technology
1980 – 1984

M.S. Electrical Engineering
Georgia Institute of Technology
1989 – 1990

M.S. Physics & Astronomy
University of Louisville
2005 – 2008

PROFESSIONAL SOCIETIES: American Astronomical Society
Society of Physics Students
2006 – 2008

AWARDS: The Manual Schwartz Award for Outstanding
Performance in Physics
2008